THÈSE

En vue de l'obtention du

DOCTORAT DE L'UNIVERSITÉ DE TOULOUSE

Délivré par :
Institut National Polytechnique de Toulouse (INP Toulouse)

Discipline ou spécialité :

Microonde, ElectroMagnétisme et Optoélectronique

Présentée et soutenue par :
Joseph EL ASSAD

le : mercredi 22 octobre 2008

Titre :

Analysis of Self-Mixing Moderate and Strong Feedback Regimes for Mechatronics Applications

---

Ecole doctorale :
Génie Electrique, Electronique et Télécommunications (GEET)

Unité de recherche :
LOSE

Directeur(s) de Thèse :

Thierry Bosch

Rapporteurs :

Prof. Franco Docchio
Prof. Olivier Parriaux

Membre(s) du jury :
Prof. Jean-José Ortheu
PhD. Marie-Anne De Smet
Associated Prof. Subhas Chandra Mukhopadhyay
Prof. Guy Plantier
Prof. Franco Docchio
Prof. Olivier Parriaux

Table of Contents

General Introduction

Laser interferometry is a well-established technique, widely used in the industrial and laboratory environments to measure displacement, velocity (of both solid targets and fluids), vibration and distance.

The usual techniques rely on an external interferometer, i.e. an optical transducer made up of lenses, prisms and mirrors, which is read-out using laser light or white light. This is the case for the well-known Michelson and Mach-Zehnder interferometers.

Optical feedback interferometry, also called self-mixing effect, is similar to conventional two beam interferometry but without all of the auxiliary bulk. A small fraction of the laser beam backscattered from diffusely-reflecting surfaces re-enters the laser active cavity and affects its spectral properties. This back-reflected light is then "self-mixed" with the standing wave in the active optical cavity. Intensity modulation has been explained in terms of interference between this standing wave and the laser beam coupled back into the cavity [1]. This generates, in particular, a variation of the laser optical power, called self-mixing interference, which can be monitored for sensing achievement [2].

History of the self-mixing effect goes back to 1960 when the laser was invented. It was noticed that external feedback into the laser cavity induces intensity modulation in the output of a gas laser [3]. A few years later, the first laser Doppler velocimeter, in which the laser cavity was used as an optical mixer was presented [4]. It was also noticed that, similarly to traditional interferometry, the fringe shift caused by an external reflector corresponds to the optical displacement of $\lambda_0/2$, where λ_0 is the operating wavelength of the laser.

Self-mixing interferometry has been exploited by many laboratories in order to develop different measurement applications for velocimetry [5], displacement, distance and vibration measurements [6]-[7]-[8], ranging [9] and 3D-imaging [10].

Recently, the self-mixing technique has also been introduced to everyday practical applications. It is reported to have been used in optical touch sensitive interfaces [11], where two self-mixing interferometers measure the movement of

the fingertip. The movement of the finger is used to control the optical scroll device.

Self mixing effect was studied in all type of lasers. However, most of these recent applications are based on a semiconductor laser as a source. For example, recent studies are founded on collecting the self-mixing signal by monitoring the change of the voltage across the diode itself and this in setups using especially VCSEL. This will help simplifying even more the experimental setup of such a type of sensors [12].

This is representative of the present state-of-the-art even if researches still use other sources like gas [13] or solid state lasers [14].

Another type of light sources where the self-mixing effect was studied is the low-coherence light sources like super luminescent diodes (SLD) [15]. Self-mixing effect in these sources has been demonstrated in applications of low coherent interferometry such in medical applications [15] or even in applications of tomography [16].

In this study, the Chapter I will introduce the physical principle of the self-mixing effect in a semiconductor laser and then will present a brief state of the art of some of the applications of this type of sensors.

Chapter II will focus then on studying the self-mixing signals in the moderate feedback regime introducing the phenomenon of loss of peaks and its outcome on some of the displacement measurement methods.

Chapter III will treat the strong feedback regime showing the feasibility of a relative displacement sensor in this regime and characterizing this sensor in terms of precision, linearity and harmonic distortion.

Finally, Chapter IV consists of an opening on the different applications of the sensor developed earlier in chapter III such as modal analysis. It was used to study a thin clamped plate and to detect impacts in carbon fiber beams.

Chapter I. Physical Principle and Applications of the Self-Mixing Effect

I.1. Introduction:

Semiconductor lasers or laser diodes are the most commonly used lasers. They are small, normally pumped directly with an injection current and hence, they are very convenient for low cost applications such as CD/DVD players, laser printers or laser pointers. This type of lasers is also the light source of most of the optical telecommunication systems which was the essential application behind the development of the semiconductor lasers. Laser diodes are still finding new application fields ranging from medical imaging to environmental sensing.

Since the beginning of use of lasers in telecommunications and in CD/DVD players, engineers encountered a problem caused by the backscattered light being reinjected in the laser cavity and changing its power and wavelength of emission. This was evoked early after the discovery of semiconductor lasers in the late sixties and early seventies [3]-[4], and notably in order to minimize the feedback in optical fiber communications [2]. The solution found was the use of optical isolators in order to eliminate this undesirable effect, but this increased the price and complexity of the complete system.

However, this effect induced a sensibility in the emission power and frequency to the laser to target distance variations, which holds a very high importance for sensing applications.

In the following chapter, the physical principle of self-mixing will be studied in the first part, exploiting how the optical feedback affects the emission properties of a laser diode and defining the basic relationships ruling its behavior. In the second part of the chapter, some of the applications covering different fields of use of the self-mixing effect will be studied.

Part A. Theoretical Study of the Self-mixing Effect

I.2. Physical Principle of Self-Mixing:

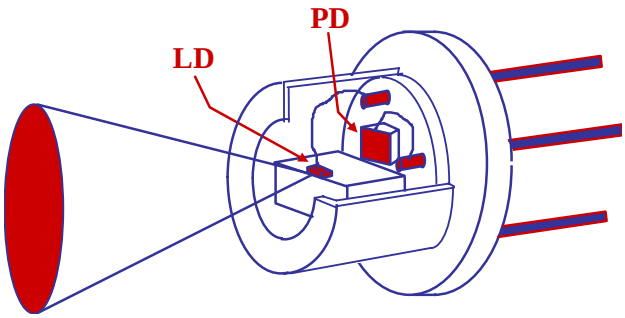

Figure I.1. Example of a commercial Package of laser diodes.

Many commercialized laser packages contain a monitor photodiode mounted behind the laser diode (Figure I.1). This photodiode is usually used in order to compensate for the drifts of the threshold current, caused by variations of the temperature of the junction that may affect the emission power.

Due to back-emission of laser diodes, this same photodiode can also be used in order to monitor the variations of the emitted power when subject to optical feedback such as in all self-mixing sensors.

In order to understand the physical principle of self-mixing, one should begin by examining the behavior of a laser in the case of free running emission and then study the effects of feedback on the different laser parameters.

I.2.1. Case of Free Running Emission:

The cavity of a free running laser diode can be modeled by a Fabry-Perot cavity of a length l delimited by two interfaces I_1 and I_2 (Figure I.2).

In this figure l is the length of the active cavity of the laser, I_1 and I_2 are the rear and front facets of the cavity respectively.

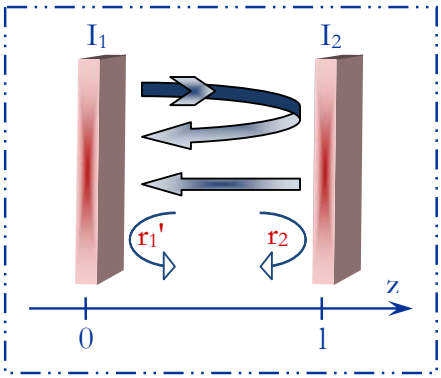

Figure I.2. Schematic arrangement for a free running state laser diode.

The amplitude of the reflection coefficients of the electrical field are r'_1 on the I_1 interface and r_2 on the I_2 interface. The optical power propagating from I_1 to I_2, $P_{1\to2}$, can be expressed as in the following equation [2]:

$$P_{1\to2}(z) = P_{1\to2}(0)\exp\left(gz - \alpha_p z\right) \tag{1.1}$$

Where g is the gain of the active medium, α_p the loss coefficient mainly caused by the absorption of the free carriers and z is the propagation direction between I_1 and I_2.

Natural emission of a diode is a spontaneous emission and in order to have laser emission, two conditions have to be fulfilled. The first one concerns the gain of the active cavity, linked to the number of the free carriers in the active zone in the case of population inversion. The other condition concerns the phase from which will be determined the emission frequency of the laser.

These conditions can be deduced from the expressions of the electrical fields. The electrical field propagating from $z=0$ to $z=l$ can be approximated by $P_{1\to2}(z) \approx \sqrt{\left|E_{1\to2}(z)\right|}$ and then can be written as follows:

$$E_{1\to2}(z) = E_{1\to2}(0)\exp\left(-j\rho z - \frac{1}{2}\gamma_a z\right) \tag{1.2}$$

With ϱ is the wave vector and γ_a the coefficient of absorption in the active medium:

$$\rho = \frac{2\pi\mu_{e0}\nu_0}{c} \tag{1.3}$$

$$\gamma_a = -g + \alpha_p \tag{1.4}$$

Where μ_{e0} represents the effective refraction coefficient of the phase of the active medium, ν_0 being the emission frequency of the laser diode and c the light's celerity.

After traveling through the active medium, the electrical field will be reflected on the I_2 interface and then its expression can be written as follows:

$$E_{2\to1}(z) = E_{2\to1}(l)\exp\left(-j\rho(l-z)+\frac{1}{2}(g-\alpha_p)(l-z)\right) \tag{1.5}$$

$E_{1\to2}(0)$ and $E_{1\to2}(l)$ are related by the equations expressed in (1.6) introducing the reflection coefficients:

$$\begin{aligned} E_{1\to2}(z=0) &= r'_1 E_{2\to1}(z=0) \quad \text{on the } I_1 \text{ interface.} \\ E_{2\to1}(z=l) &= r_2 E_{1\to2}(z=l) \quad \text{on the } I_2 \text{ interface.} \end{aligned} \tag{1.6}$$

The above equations expressing the electrical field leads to the emission condition (1.7) of a laser diode without optical feedback [17]:

$$r'_1 r_2 \exp\left(-j\frac{4\pi\mu_{e0}\nu_0}{c}l+(g_{th0}-\alpha_p)l\right)=1 \tag{1.7}$$

The resolution of the condition presented in equation (1.7) in terms of phase and module leads to the determination of both key parameters of the laser g_{th0} and ν_0.

g_{th0} being the threshold gain without any feedback i.e. the minimum gain needed for laser emission:

$$g_{th0} = \alpha_p - \frac{1}{l}\ln(r'_1 r_2) \tag{1.8}$$

The second parameter obtained from the resolution of the emission condition is the emission frequencies, ν_0, given by the following equation:

$$\nu_0 = q\frac{c}{2l\mu_{e0}} \tag{1.9}$$

Where q is an integer, and thereby, for each value of q corresponds an emission frequency and hence a longitudinal emission mode.

I.2.2. Case of Laser Diode Submitted to Optical Feedback:

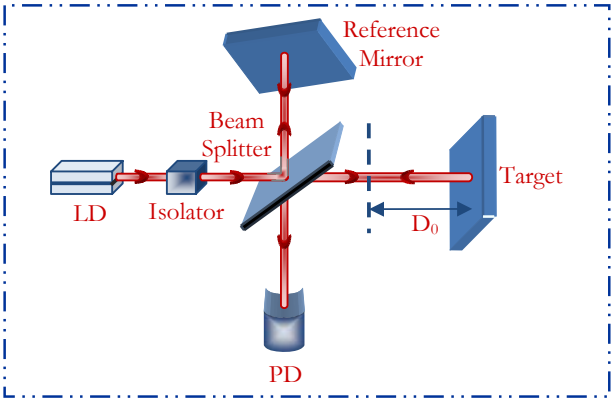

Figure I.3. Setup for a Michelson interferometer.

In presence of a target in the direction of emission, light will be diffused and a part of this diffused light will be coupled back into the laser cavity changing thereby its emission characteristics. The self-mixing setup may be compared to a classic Michelson interferometer as represented respectively in Figure I.3 and in Figure I.4.

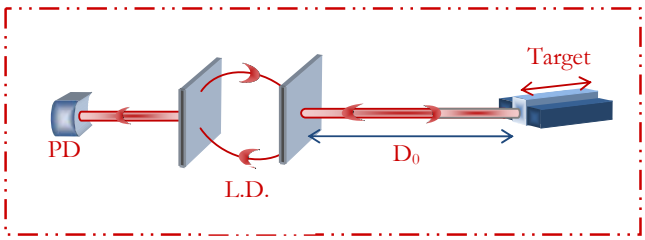

Figure I.4. Setup for a Self-Mixing interferometer.

From these two previous figures it can be seen that a similitude exist between these two setups but the self-mixing setup is a lot simpler where all the expensive optical components (mirrors, isolators and beam splitters) are not needed. The system is auto aligned as both the laser diode (LD) and the photodiode (PD) are included in one package.

I.2.2.a. Theory of The Equivalent Cavities:

In order to explain the self-mixing effect, the theory of equivalent cavities must be introduced. The space between the front facet of the laser and the target can be considered as an external cavity coupled to the internal active cavity inside the laser diode as shown in Figure I.5.

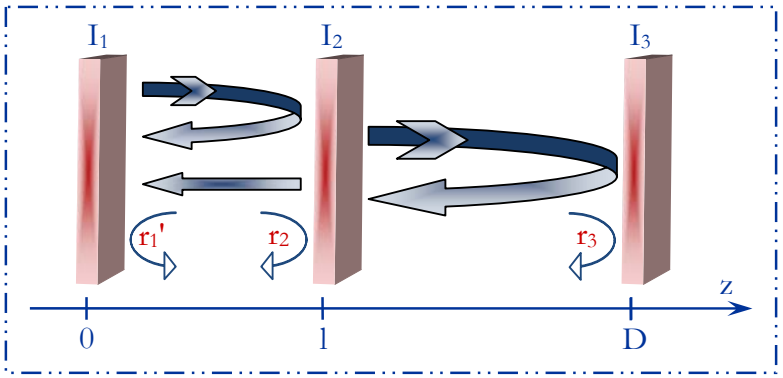

Figure I.5. Internal and external cavities.

In fact, both the active Fabry-Perot cavity and the external cavity can be replaced by an equivalent cavity (Figure I.6) of width l_{eq} and with a complex equivalent amplitude reflectivity index r_{eq} given later on by equation (1.12) [17].

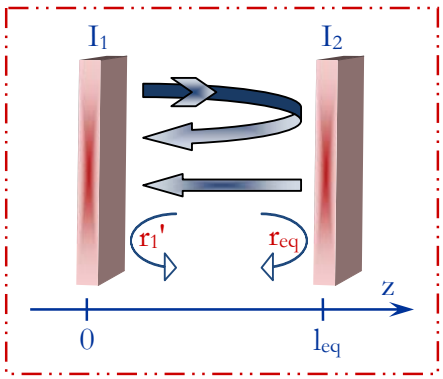

Figure I.6. Equivalent cavity.

By neglecting the multiple reflections within the external feedback for a weak to moderate feedback (since the targets reflectivity $r_3 << r_2$) then r_{eq} can be written as the reflected electrical field at the interface I_2, E_r, divided by the incident field E_i. In this case, a plane wave propagating along the z axis is considered and its electrical field $e(t,z)$ is written as follows:

$$e(t,z) = B\exp\left[j\Phi\left(t-\frac{z}{c}\right)\right] \quad with \quad \omega_F\left(t-\frac{z}{c}\right)=\frac{d\left(\Phi\left(t-\frac{z}{c}\right)\right)}{dt} \qquad (1.10)$$

Where B is the amplitude of the wave, Φ, its phase and ω_F the pulsation of the wave in presence of the target.

Let $e_i(t,z)$ be the incident electrical field and $e_r(t,z)$ the one reflected by the target. Now considering that the variation of the target's speed is negligible during the time of flight of the wave ($\tau_D = 2D/c$) the expression of the fields at the

interfaces may be written: E_i the incident field, E_{r1} the one reflected at the I_2 interface and E_{r2} the field reinjected in the laser cavity after being reflected by the target.

$$E_i = e_i(t,0) = B\exp\left(j\int_0^t\left(\omega_F(t,0)dt\right)\right)$$
$$E_{r1} = r_2 E_i \tag{1.11}$$
$$E_{r2} = e_r(t,0) = t_2 r_3 t'_2 B\exp\left(j\left[\begin{array}{l}\int_0^{t-\frac{\tau_D}{2}}\left(\omega_F(t,0)dt\right)+\\ \int_{t-\frac{\tau_D}{2}}^{t-\tau_D}\frac{c-V_F}{c+V_F}\omega_F(t,0)dt\end{array}\right]\right)$$

Where t_2, and t'_2 respectively, is the transition coefficient of the I_2 interface from the laser diode to the outside and respectively from the outside to the laser diode. The first integral term represent the phase difference of the wave due to the laser to target path and the second term the phase difference caused by the opposite path.

Considering normal incidence at the laser surface then $t_2t'_2=1-r_2^2$; and moreover, neglecting the frequency shift due to the Doppler Effect, thereby, the equivalent reflectivity index can be approximated using a limited development as follows:

$$r_{eq}(t) = \frac{E_r}{E_i} = r_2\left[1+\zeta\exp\left(j\left[\int_t^{t-\tau_D}\omega_F(t,0)dt\right]\right)\right] \tag{1.12}$$

Where $\zeta = \left(1-r_2^2\right)r_3/r_2$ is the coupling parameter between the target and the laser cavity.

In this case, the emission condition is unchanged by replacing the parameters without feedback with parameters taking into account the feedback such as r_2 is replaced by r_{eq}.

$$r'_1 r_{eq}\exp\left(-j\frac{4\pi\mu_{eF}\nu_F}{c}l+\left(g_{thF}-\alpha_p\right)l\right)=1 \tag{1.13}$$

g_{thF} being the threshold gain under feedback.

As mentioned earlier the resolution of this condition in terms of phase and amplitude leads respectively to the determination of the permitted emission frequencies and the variations of Output Optical Power (OOP).

I.2.2.b. Threshold Gain and Permitted Emission Frequencies:

Looking back at both equations (1.7) and (1.13) they can be united in one single equation as follows:

$$\left[\left\|\frac{r_{eq}}{r_2}\right\|\exp\left(\left(g_{thF}-g_{th0}\right)l\right)\right]\exp\left(-j\left(\Phi_F-\Phi_0\right)\right)=1$$

$$With\begin{cases}\Phi_F=\dfrac{4\pi\mu_{eF}\nu_F l}{c}+\Phi_{eq}\\ \Phi_0=\dfrac{4\pi\mu_{e0}\nu_0 l}{c}\\ -\Phi_0=-\Phi_F=2q\pi\end{cases}\tag{1.14}$$

The resolution of the modulus part of the equation in (1.14) gives the threshold gain g_{th} of the laser under feedback. On the other hand, the resolution of the phase equation gives the emission frequency under feedback:

$$g_{thF}-g_{th0}=-\frac{\zeta}{l}\cos\left(2\pi\nu_F\tau_D\right)\tag{1.15}$$

$$\Phi_{thF}-\Phi_{th0}=\frac{4\pi l}{c}\left(\mu_{eF}\nu_F-\mu_{e0}\nu_0\right)+\zeta\sin\left(2\pi\nu_F\tau_D\right)\tag{1.16}$$

The phase equation when solved can be rewritten as follows:

$$\Delta\Phi_L=\nu_F-\nu_0+\frac{C}{2\pi\tau_D}\sin\left(2\pi\nu_F\tau_D+\arctan\left(\alpha\right)\right)=0\tag{1.17}$$

In equation (1.17), two new terms were introduced a the linewidth enhancement factor and the coupling coefficient C defined as follows:

$$C=\varepsilon\frac{\tau_D}{\tau_l}\zeta\sqrt{1+\alpha^2}\tag{1.18}$$

Where τ_l is the time of flight of propagation of light inside the active cavity. On the other hand, it can be seen that this equation accounts for effect of the distance through τ_D and for the effect of the light retro-diffused by the target through ζ. ε is a parameter accounting for the fraction of light effectively reinjected in the laser's cavity [18]-[19]. However, this parameter has to take into account the fact that the emitted beam is Gaussian and will be modified by the target before being reinjected in the laser cavity. Thereby the interference will be

between two different intensity spectrums which causes space overlapping. If the alignment was perfect ε should be equal to unity and hence C should be mainly limited by the coherence length of the laser.

Looking back at the equation (1.17), $\Delta\phi_L$ may be simulated (using MATLAB) and plotted as a function of $(\nu_F-\nu_0)$ for different values of C (Figure I.7). The zero crossings of these curves corresponds to solution of the phase equation and thereby possible emission frequencies or modes of the laser.

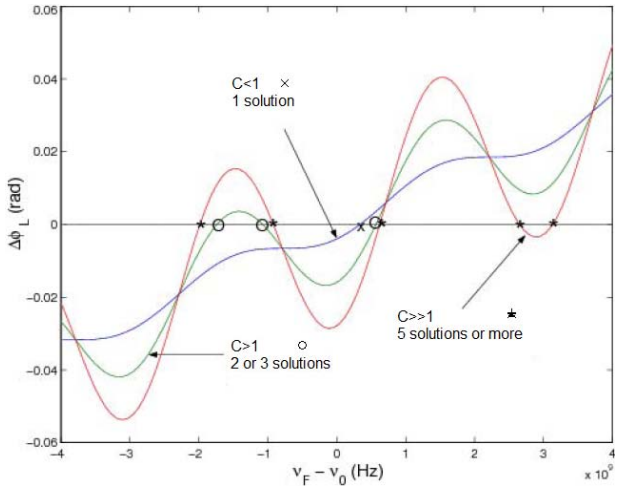

Figure I.7. Solution of the phase equation for different values of C

Depending on the number of solutions, on which C has a major effect, the functioning of the laser can be divided into five regimes as shown in Figure I.8.

In this figure, $\kappa_{ext}=\zeta\varepsilon$ represents the effective optical power reinjected in the laser cavity whereas D_0 is the distance separating the laser diode and the target at $t=0$. Both these two parameters represent the varying parts of C thereby this figure shows indirectly the laser emission modes as a function of C.

Figure I.7 showed that for values of C lower than *1* corresponding to weak levels of feedback only one solution can be found for equation (1.17) meaning that the laser will have one single lasing mode when subject to feedback which maybe encountered in the case of a lot of non-corporative targets.

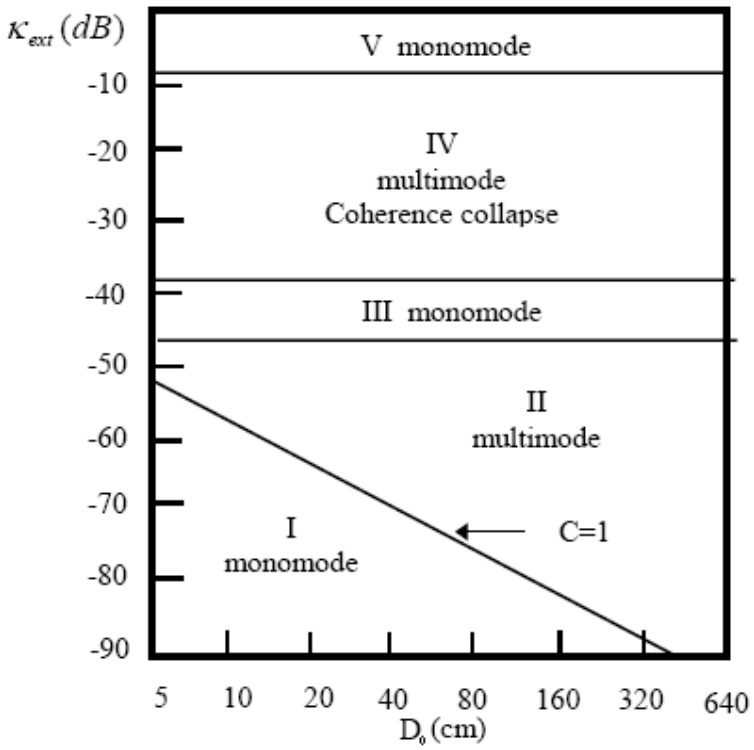

Figure I.8. Different functioning regimes of a laser diode under feedback.

Now, for stronger feedbacks (i.e. $C>1$) the phase equation may have several solutions. In fact, if the case of maximum 3 possible solutions is studied the limit of this regime may be found numerically by solving equation (1.17). *Ca* is the maximum value of *C* corresponding to only three solutions and which can be calculated and found to be $Ca \approx 4.7$ [20]. In this case, the laser was found to stay monomode because, among the three possible modes, only the mode having the narrowest spectral width will be chosen by the laser [21].

For the higher functioning modes III, IV and V, the power reinjected is very important giving them some special characteristics. In fact, in the regime III the laser is perfectly monomode and the spectral width is very narrow. Regime IV, is the coherence collapse regime in which the laser diode loses all its coherence properties (spectral width around the GigaHertz). Finally in regime V, the laser comes back to being monomode with a very high rejection on the lateral modes of the laser cavity. This regime is characterized by a very narrow spectral width and is usually used to obtain stable monomode sources.

I.2.2.c. Optical Output Power of a Laser Diode Submitted to Feedback:

On the other hand, in order to express the optical emitted power, the electron rate equations at stationary operation must be considered for the free running state [22]-[23].

$$\frac{dn_0}{dt} = \frac{1}{e}\frac{dJ}{dx} - v_g N_0 g\left(n_0\right) - \frac{n_0}{\tau_n} \tag{1.19}$$

Where n_0 is the density of electrons in excess, t is the time, e is the elementary charge of an electron, J in the current density, v_g is the group velocity, N_0 is the photon's density and finally τ_n is the average lifetime of electrons.

In the above equation, all carriers are supposed to be injected in the active zone of the laser diode; which can be obtained through a double hetero-junction as shown in Figure I.9.

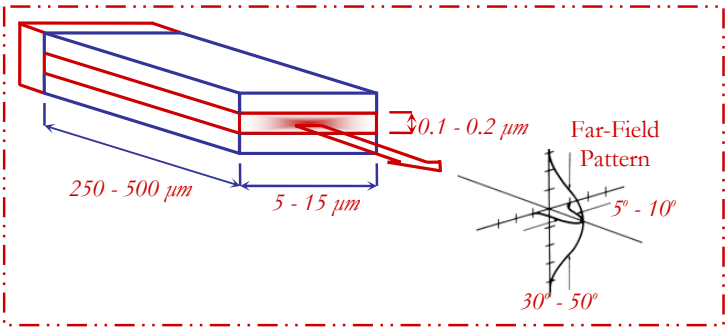

Figure I.9. Structure of a double heterpstructure Fabry Perot laser

Now considering simultaneously the case of a laser diode in its free running state (index 0) and with feedback (index F) it is possible to construct the following equation system (considering in both cases a constant current density J and a linear gain).

$$\begin{cases} \dfrac{J}{ed} = v_g N_0 \dfrac{dg_{lin}}{dx}\left(n_{th0} - n_{nul}\right) + \dfrac{n_{th0}}{\tau_n} \\ \dfrac{J}{ed} = v_g N_F \dfrac{dg_{lin}}{dx}\left(n_{thF} - n_{nul}\right) + \dfrac{n_{thF}}{\tau_n} \end{cases} \tag{1.20}$$

Where d is width of the active zone of the laser diode. n_{nul} is the electrons' density permitting to have a zero gain. The indexes *th* and *lin* correspond respectively to a threshold value and to a linear value (of the gain).

Now, relying on equation (1.20) and considering that $\Delta n = n_{thF} - n_{th0}$ has a small value, it is possible to express the photons' density when the laser is under feedback as a function of their density when the laser is in the free running state.

$$N_F = N_0 \left[1 - \Delta n_{th} \frac{v_g \left(\frac{dg_{lin}}{dn} \right) - \frac{1}{N_0 \tau_n}}{v_g \left(\frac{dg_{lin}}{dn} \right) \left(n_{th0} - n_{nul} \right)} \right] \tag{1.21}$$

Equation (1.15) expressed the gain of the diode in presence of a target as a function of its gain when by itself, thereby it is possible to introduce the phase $2\pi\nu_F\tau_D$ in the expression of the photons' density (1.21) as follows [23]:

$$N_F = N_0 \left[1 + m \cos\left(2\pi\nu_F \tau_D \right) \right] \tag{1.22}$$

Where m is a parameter representing the modulation of the laser.

$$m = \frac{\zeta}{g_{th0} l} \left[1 + \frac{1}{v_g N_0 \tau_n \left(\frac{dg_{lin}}{dn} \right)} \right] \tag{1.23}$$

Finally, considering the proportionality between the photons' density and the emitted optical power, this last can be written as follows [22]-[23]:

$$P_F = P_0 \left(1 + m \cos\left(2\pi\nu_F \tau_D \right) \right) \tag{1.24}$$

Looking back at the expressions of the emission Optical Output Power (OOP) (equation (1.24)) and the frequency under feedback (equation (1.17)), they are both a function of the laser-target distance through τ_D. Hence, both will be modified if this distance changes or if the injection current is modified (through ν_0) or if both of them change. These expressions are then of major importance when studying self-mixing for metrological purposes since they relate the distance to the emitted OOP the one that can be easily monitored through the control photodiode as mentioned earlier.

Part B. Different Applications of the Self-Mixing Effect

I.3. Advantages of Self-Mixing Sensors

As mentioned earlier, the self-mixing (SM) signal was, and still is, considered as a parasite signal in applications like telecommunications and CD/DVD readers. The self-mixing causes the lowering of the efficiency of these systems. However, when exploiting, the expression of the OOP in presence of a target, both the power (1.24) and the frequency (1.17) are modified by variations of the distance separating the laser diode from the target making it very suitable for distance and displacement measurements [2]-[24]-[25].

This last characteristic gave the SM effect a sensing ability which was accentuated by different other advantages such as:

- The simple and compact set-up since the sensor is self-aligned there is no need for any of the expensive external optics used in traditional interferometry (Figure I.4).
- No external photodetector (PD) is required, because the signal is provided by the monitor photodiode contained in the laser diode (LD) package (Figure I.1). Moreover, even this PD was eliminated in some recent SM setups monitoring the variations of the LD voltage directly [12].
- The sensitivity of the scheme is very high, being a sort of coherent detection that easily attains the quantum detection regime (i.e. sub-nm sensitivity in path length is possible) [19].

The first demonstrations of this principle used gas lasers to detect the Doppler shift caused by a moving remote reflector [4]. After that, self-mixing sensors knew the first complete self-mixing interferometer/vibrometer [26] and the use of a laser diode (LD) as a source and a detector at the same time [27]. Remote sensing applications based on the self-mixing effect in low-cost commercial Fabry–Perot (FP) LDs have appeared in the scientific literature first in

1986 [27]-[28], demonstrating the feasibility of velocity, distance and displacement measurements [27]-[28].

I.4. Displacement Measurement

Displacement measurements are achieved in different domains using multiple sensing technologies like resistive, inductive, capacitive, ultrasonic, magnetic and piezoelectric technologies [29]. Due to its simplicity, self-mixing interferometry is being exploited more and more in different sensing domains such as in particular displacement measurement or vibration analysis.

I.4.1. Basic Principle

As mentioned earlier equations (1.17) and (1.24) giving the expressions of the emitted frequency and optical power are important. They both depend on the distance separating the laser from the target and the injection current. In fact, both will stay constant if the LD is driven by a DC injection current and if the laser to target distance is kept constant. However, when a back-reflection is generated by a moving target in the direction of light emission, the optical length of the external cavity is varying and consequently the length of the equivalent cavity is modified too, affecting the spectral properties of the laser.

The Figure I.10 represents saw-tooth like fluctuations of a self-mixing signal (i.e. for a weak feedback $0.1<C<1$) corresponding to a sinusoidal displacement.

The OOP was expressed in (1.24) as an amplitude modulation where the phase is given by $\Phi=2\pi\nu_F\tau_D$. Moreover, similarly to traditional interferometry, the full swing of power matches to a half-wavelength displacement (considered theoretically as corresponding to a phase-shift of 2π).

$$\left|2\pi\nu\Delta\left(\tau_D\right)\right| = 2\pi \Leftrightarrow \left|\Delta D\right| = \lambda/2 \qquad (1.25)$$

A method traditionally used to retrieve the displacement with a basic resolution of $\lambda_0/2$ is the fringe counting method based on considering that the number of saw-tooth like fringes is directly proportional to the displacement. It consisted in counting these power fluctuations and adding them with their proper

sign. For a motion in one direction, if N fluctuations are detected, the corresponding displacement of the target is theoretically given by $D=N.\lambda_0/2$. It will be demonstrated later in this manuscript that this method should be limited to the weak feedback regime.

On the other hand, the asymmetric shape of the saw-tooth like signal was experimentally observed [22]-[29]. It was found that the influence of the variation of the refractive index on the feature of fringe inclination is related by the linewidth enhancement factor α in equation (1.17). It permits to directly recover the target direction of displacement (Figure I.10).

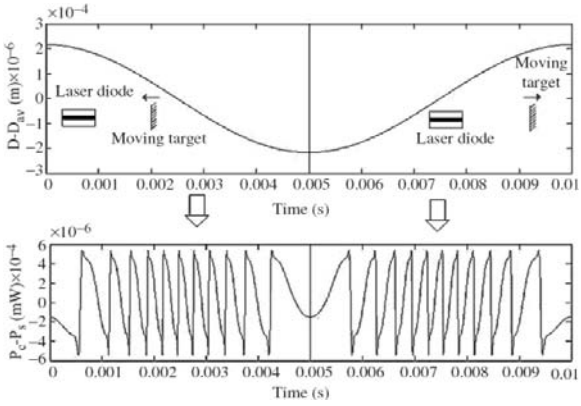

Figure I.10. Saw-tooth like fluctuations for a sinusoidal displacement.

In order to compare, such information can be conventionally achieved with two interferometry channels. In the case of single-channel optical feedback interferometry the only optical component required is a lens used to collimate the laser source in the purpose of focusing the emitted light on the remote target showing the advantage of simplicity of these systems.

Other methods for increasing the resolution of displacement measurement exist such as the phase demodulation [30] that will be exploited in details in chapter II or like the use of extended Kalman filters [31], the use of wavelets transforms or even genetic algorithms [32].

I.4.2. Effect of The Speckle

The speckle effect is an effect encountered when light is reflected by a diffusing surface, where the back-scattered beam shows a characteristic random texture (Figure I.11).

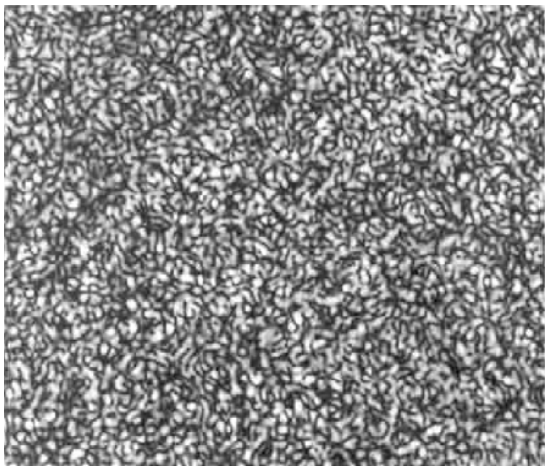

Figure I.11. The randomly spotted texture of the Speckle effect.

This spatial-coherence destruction of the beam is caused by the interaction with the diffuse surface roughness [33]-[34] in two levels. First a specular reflection corresponding to a mirror reflection generating a very directive beam; and the a diffusing or Lambertian diffusion spreading the light uniformly in the space (Figure I.12)

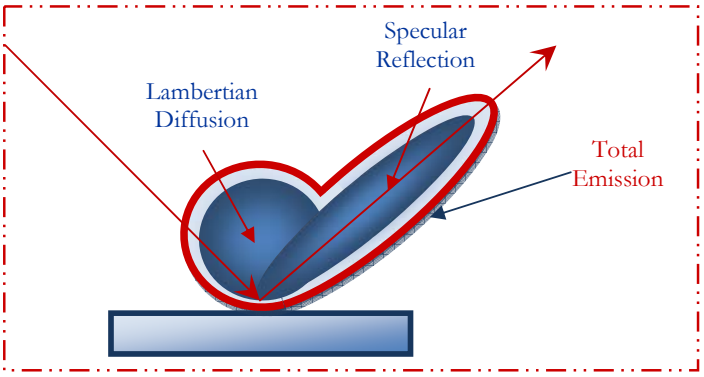

Figure I.12. Emission diagram of a regular surface

When the roughness of the target's surface is comparable to the emission wavelength then there will be a creation of elementary-sources diffusing back the light and interfering with each others causing the randomly spotted texture shown in Figure I.11. Now the fluctuation between constructive and destructive interferences will induce a fading in OOP as shown in Figure I.13. As only incremental measurement is achieved for displacement sensing, data can be lost because of a very poor signal-to-noise ratio, whereas within a speckle grain, the fringe visibility is still adequate to perform a measurement.

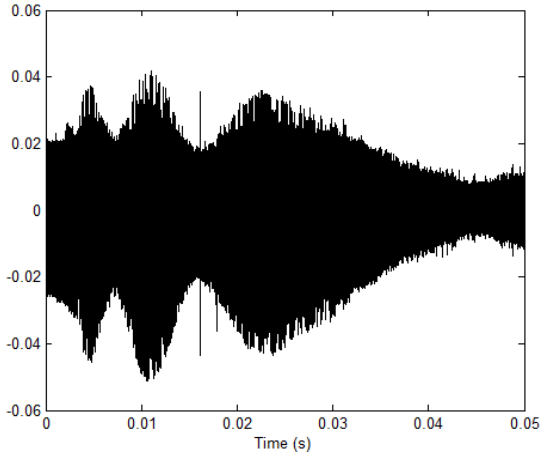

Figure I.13. OOP fading caused by the speckle effect

In order to overcome this limitation caused by the speckle effect, many methods were developed such as bright speckle tracking systems [35].

I.4.3. Increase of Resolution

Different signal processing methods have been proposed to increase the basic resolution beyond half-wavelength. A fast modulation of the optical path difference of a feedback interferometer will modify the round-trip external delay. For example, this can be achieved by using the electro-optical properties of a lithium Niobate crystal acting as a phase modulator [6]. Theoretically, N self-mixing signals can be used and with phases spaced by $2\pi/N$ and sample them properly to reconstruct the displacement with a resolution of $\lambda_0/2N$. Experimentally, a DSP card has been used for simultaneous monitoring in order to achieve a resolution of $\lambda_0/10$ with 5 phase-shifts. This type of sensors has been used as a direct diagnostic tool to characterize fabricated microstructures like MEMS and MOEMs [36]. A silicon vibrating gyroscope has been tested in order to tune the resonance frequency and maximize the quality-factor of the structure [36]. The use of this sensor has then been extended to four-mass gyroscope and microresonators showing how feedback interferometry is suitable for characterizing silicon microstructures [37]. A hybrid opto-mechanical gyroscope has also been developed with a MEMS-like mechanical resonator combined with this sensor for optical readout [38]. A simplified version of this sensor consists in the linearization of the normalized optical power which has been approximated by

an ideal saw-tooth signal [39]. Even if there is no need for preliminary measurements of parameters, this solution is limited to moderate feedback but with a resolution of around $\lambda_0/12$.

I.5. Vibration Measurement

Vibration measurement is essential in many mechanical or mechratonic fields where it can be used to minimize or eliminate the resultant vibration noise. There are also examples where the noise is not the key parameter, but rather a parameter for quality control of the manufactured products. For example, excessive vibration can damage the product, limit processing speeds, or even cause catastrophic machine failure.

The study of self-mixing (SM) principle for the design of sensors in order to measure vibrations is reported since 1996 [40] where the small dimensions and the low-cost of such sensors are among the main practical reasons why researchers have concentrated their attention on this technique.

Self-mixing sensors were privileged in this type of applications because of different facts such as its high sensitivity, large bandwidth and a large dynamic range up to *70 KHz* and *100 dB* [41]. Moreover, it is able to function on different types of surfaces without any optical modulation and permitting equally to measure low frequency vibrations. The sensor developed in [40] permitted to measure vibrations of approximately all types of surfaces with a bandwidth between *0.1 Hz* and *70 KHz* with a maximal peak to peak amplitude of *180 µm*. A special algorithm was developed in order to analyze in real time the self-mixing signal permitting thereby to track the velocity variations of the target.

In 2004, a self-mixing sensor used in piezoelectric transducers characterization [42] permitted to measure the velocity and vibrations of solid targets with results comparable to those obtained by the conventional laser Doppler velocimeter (LDV). The technique used was similar to the one used in LDV where it was able to treat the signals even in presence of speckle with the simplicity of self-mixing sensors.

I.6. Velocity Measurements

Velocity measurement is an essential parameter for safety and profitability of manufactured systems in different areas like aerospace, automotive, metallurgy or paper industry. In fact, there is an increasing need for remote sensing with rough targets in hostile environments or for in-line assembly processes as contact devices can ruin the items being measured.

Non-contact measurements can be performed with ultrasonic or microwaves devices but with poor spatial definition and therefore optoelectronic systems are an alternative solution of great interest. LDV is a very accurate method extensively developed for surface speed measurements but it is expensive because it requires high stability of both optics and mechanics [43]. An emerging method is the Tracking Laser Doppler Velocimetry (TLDV) which optimizes the tracking algorithm strategy compared to the LDV. Feedback interferometry presents the significant advantages of being compatible with a wide range of target characteristics (roughness, color …) still at a very low-cost.

More recent application was the conception of an onboard velocity sensor using the self-mixing effect. Roughness of the target surface, wet target surfaces, non-controlled changes of incident angle, and speed vector vertical components have been considered during this development. A first prototype has been designed with an automotive application so to illustrate its feasibility. This low-cost prototype presents an interesting basic performance. In order to improve the accuracy as well as the robustness of the system, a double-laser diode sensor has then been tested successfully by removing the influence of the pitching and the pumping effects [44].

I.6.1. Physical Principle

The technique of velocity measurement using self-mixing sensors is based on the Doppler-Fizeau effect

$$F_D = \frac{2V_F}{\lambda} \tag{1.26}$$

Where F_D is the Doppler frequency that corresponds to the frequency of the saw-tooth like self-mixing signal and V_F is the velocity of the target. In fact, velocimetry was the first application of the self-mixing effect as the first realizations were accomplished using a gas laser He-Ne [4] and with CO_2 lasers [44]-[45]. However these sources were able to determine the Doppler frequency only in a reduced frequency span.

It was until the mid 80's [46] laser diodes were first used in weak feedback in order to determine the Doppler frequency with a spectrum analyzer or in moderate feedback in order to determine the movement direction through the peak inclination.

Recently VCSELs (Vertical Cavity Surface Emitting Lasers) were used in velocimetry around their bias point [47]. Although their signal to noise ratio (SNR) would have increased in their bistable mode but the signal in this case would lose his sawtooth like shape and will have instead a square shape causing thereby the loss of information about the displacement's direction.

I.6.2. Measurement of Rotation Velocities

The self-mixing sensors may be used also in order to measure velocities of displacements that are not necessary in the propagation direction where in this case the Doppler frequency is given by the following equation:

$$F_D = \frac{2V_F}{\lambda}\cos(\Psi) \tag{1.27}$$

Where in this case, V_F is the module of the velocity vector having ψ as an angle with the propagation direction.

This Doppler frequency can be easily determined by applying a real time Fast Fourier Transform (FFT) to the self-mixing signal. However, this measurement will be strongly affected in the case of rough target's surfaces. A second order auto-regressive algorithm will then be applied to the SM signal in order to ameliorate the system resolution by a factor of 10 [48].

I.6.3. Speckle Velocimetry

Speckle as explained earlier was considered as a parasite effect degrading the efficiency of displacement measurement SM systems.

However it may be used in order to measure the velocity of rough targets with a velocity perpendicular to the direction of the propagation, minimizing thereby the Doppler effect as $\psi=\pi/2$. When the surface will have a translation movement, a part of the beam will be reinjected inside the cavity and the speckle effect will cause a random variation of the OOP. It was shown in [5] that, using two laser sensors, there will be a linear relationship between the autocorrelation of the speckle signal and the velocity of the rough moving surface.

This type of sensors was used in order to determine the surface's roughness and to accomplish then a surface classification using a neural network [5].

I.6.4. Medical Applications

Self-mixing sensors were exploited in different medical fields because of their advantages previously exploited, especially their compact size and their ability to access to far measurement points without contact.

In fact SM sensors were used in different medical fields. First of all the measurement of the velocity of the blood flow inside the arteries was performed. In this case, the laser diode will be pigtailed with an optical fiber that will be inserted inside the blood vessel with a catheter. Thereby, the beam will penetrate inside the blood flow and a part will be diffused by the blood cells with a frequency Doppler shift. The backscattered beam will then be mixed inside the active cavity with the lasing modes at their original frequency giving thus the Doppler velocity of these cells. Such sensor was used in order to measure the blood flow inside the pulmonary artery of a pig [49]. These measurements along with the same blood canal enable the doctors to detect an irregular diminution of a blood vessel permitting them to perceive many deceases. Particular cardiovascular deceases may be detected where since the beginning of the 1960's, different methods were developed in order to measure the red cells velocity. However, their bandwidth, of approximately *3Hz*, did not permit these sensors to

evaluate the blood velocity of animals with a high heart pace. By fixing the fiber optic of a SM sensor at the skin with a precise angle of 30^{o} (i.e.) the blood flow (of a sheep i.e. [50]) can be measured using equation (1.27).

Moreover, a linear equation was found between the autocorrelation of the SM signal disrupted by the speckle and the human blood flow measured at the top of the finger [51]. This was realized using only a laser diode, its control photodiode and a collimating lens without the need of any contact with the skin.

Finally, self-mixing sensors were used in the detection of the muscular vibrations known as mechanomyography or MMG used in sport medicine in order to diagnose the neuromuscular deceases and the ageing of the muscular structure in order to avoid possible injuries [52].

I.7. Absolute Distance Measurements

In this type of sensors, and contrary to all the other types introduced in this manuscript, the injection current is not constant but modulated by a triangular signal. Thereby, in this case, the external cavity length can be constant, however the equivalent Fabry-Perot cavity's length will be modified because of equivalent variations of the active cavity's length caused by the current modulation.

The first sensor of this type was conceived by Berheim and Fritsch in 1986 [53] having a resolution of *15mm* over a distance of *1.5m*. In 1998, the capabilities of the sensor were ameliorated using the Fabry-Perot laser diode LD64110N accomplishing thereby a resolution of *4mm* over a measured distance of *3m* [7].

I.8. Conclusion

The theory of self-mixing was introduced showing its advantages for different sensing applications such as displacement or velocity measurements.

One of the main advantages of this type of sensors is the simplicity of the system which is being simplified more and more by using new light sources. For example, VCSELs present a low threshold current ideal for embedded systems. New self-mixing VCSEL sensors are now being conceived without a photodiode

where the variations of the OOP are monitored by looking directly at the changes of the voltage across the laser diode itself [12].

First commercialized self-mixing sensors are newly launched by Philips through their "Twin-Eye" laser sensor [11] adopted by different computer mice manufacturers such as the new high resolution A4tech gaming mouse or the Logitech V400 mouse [54]. This same sensor would be implemented by Philips also in mobile phones [55], PDAs or laptop computers in order to reduce the size and price occupied by usual inputs such as touch screen, mechanical joysticks or touch pads.

As a conclusion, self-mixing is an emerging technique which is newly commercialized, proving its interest in terms of cost and simplicity for future mass-market applications ranging from medicine to transportation.

Chapter II. Analysis of a Self-Mixing Signal for Displacement Measurements Using a Laser Diode under Moderate Feedback

II.1. Introduction:

In the last two decades, several studies proved that the Laser Diode (LD) Self-Mixing (SM) interferometry is an innovative solution for different applications of vibration, displacement and velocity measurements [2]-[25]-[42]-[56]. The simplicity of SM based sensors makes them very convenient for industrial use due to the ability of their integration into more complicated measurement systems.

These sensors are based on the fact that when a moving target reflects or diffuses the light back, a part of this light is coupled back into the laser cavity, interfering thereby with the lasing beams and thus, inducing pseudo periodic variations of the Optical Output Power (OOP). As in classic interferometry, each peak of these variations corresponds theoretically to a $\lambda_0/2$ of displacement where λ_0 is the emitted wavelength under free running conditions.

Looking back at equation (1.18), it can be seen that depending on the target's surface reflectivity, the distance separating the laser from the moving target and the emission power, different values of the coupling factor are possible.

These variations of the coupling factor will be perceived through their effect on the shape of the variations of the OOP (Figure I.8). These shapes will impose differences in the needed signal processing making thereby the measurement more complex.

In this chapter, we will first remind the principles of the behavioral model and the phase unwrapping method used along this study. Then the effect, of both the linewidth enhancement factor and the coupling coefficient, on the shape of the self-mixing signal is studied along with the variations of C as a function of the

distance separating the laser and the target. Afterwards, the theory of loss of peaks in the moderate feedback regime is introduced and the number of peaks is studied as a function of different key parameters. Finally, the effect of this loss of peaks on both the fringe counting and phase unwrapping techniques is studied.

II.2. Behavioral Model of LD under Feedback

This model, conceived earlier [57], simulates the behavior of a laser diode subject to different feedback levels caused by a target at a certain distance. In fact, this model will give at its output the self-mixing signal from the displacement, the linewidth enhancement factor and the coupling coefficient as inputs. Going back to the basic equations derived in chapter I, the phase equation (2.1) and the variations of the optical output power under feedback (2.2) are rewritten and two new variables, named $x_F(t)$ and $x_0(t)$, could be defined respectively in equations (2.3) and (2.4) [57].

$$\nu_F - \nu_0 + \frac{C}{2\pi\tau_D}\sin\left(2\pi\nu_F\tau_D + \arctan(\alpha)\right) = 0 \tag{2.1}$$

$$P_F = P_0\left(1 + m\cos\left(2\pi\nu_F\tau_D\right)\right) \tag{2.2}$$

$$x_F(t) = 2\pi\frac{D(t)}{\lambda_F(t)/2} = 2\pi\nu_F(t)\tau(t) \tag{2.3}$$

$$x_0(t) = 2\pi\frac{D(t)}{\lambda_0(t)/2} = 2\pi\nu_0(t)\tau(t) \tag{2.4}$$

This will enable us to rewrite equations (2.1) and (2.4), using these variables, respectively as follows:

$$x_0(t) = x_F(t) + C\sin\left[x_F(t) + \arctan(\alpha)\right] \tag{2.5}$$

$$P(t) = P_0\left\{1 + m\cos\left[x_F(t)\right]\right\} \tag{2.6}$$

Now, equation (2.5) could be seen as an injective non linear relation G between $x_F(t)$ and $x_0(t)$ and could be expressed as follows [57]:

$$x_0(t) = G\left[x_F(t); C; \alpha\right] \tag{2.7}$$

However, the model will deduce the OOP variations, using equation (2.6), from the displacement, and hence $x_0(t)$. In fact, $P(t)$ is expressed as a function of

$x_F(t)$ and thereby it is necessary to define a causal relationship between $x_F(t)$ and $x_0(t)$, this is the inverse function $F=G^{-1}$:

$$x_F(t) = G^{-1}\left[x_0(t);C,\alpha\right] = F\left[x_0(t);C,\alpha\right] \tag{2.8}$$

The previous equations derived in this paragraph may seem complicated not showing the transformations of the displacement into OOP variations. Thereby these equations will be described through a bloc diagram exploiting the behavioral model.

First of all, in the case of weak feedback, i.e. $C<1$, the F function has only one solution and the value of the model can be described as follows [57].

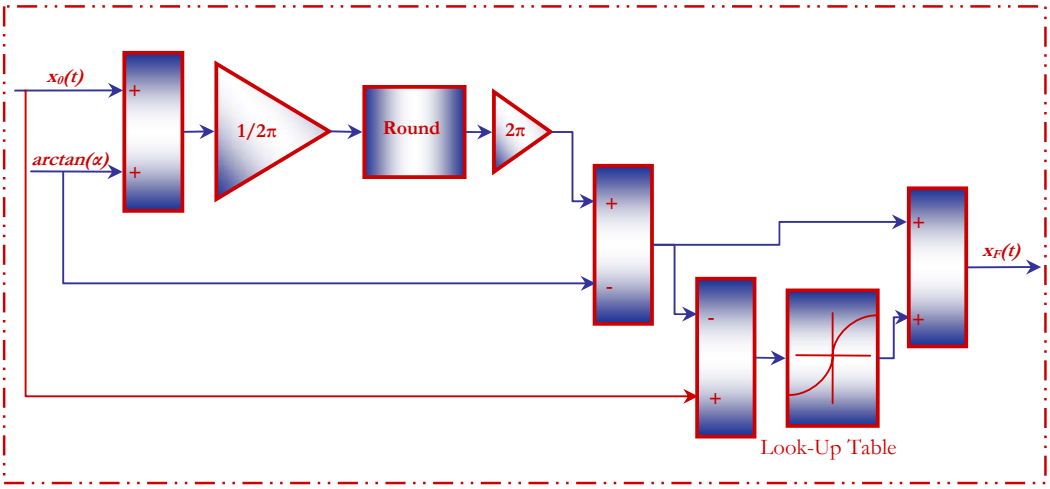

Figure II.1. Bloc diagram of the behavioral model in the case of C<1

In the case of $C<1$, the look up table consists of a simple interpolator since the F function has only one solution in each case. When C increases, i.e. $C>1$, the F function will have more solutions and the value of k will have to be determined through an infinite set of comparators (Figure II.2) in order to be able to deduce $x_F(t)$ and in this case the model can be described throughout the bloc diagram in Figure II.3 [57].

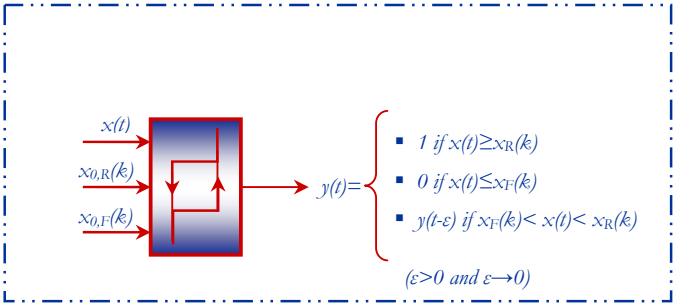

Figure II.2. Comparator used in the bloc diagram of the behavioral model in the case of C<1

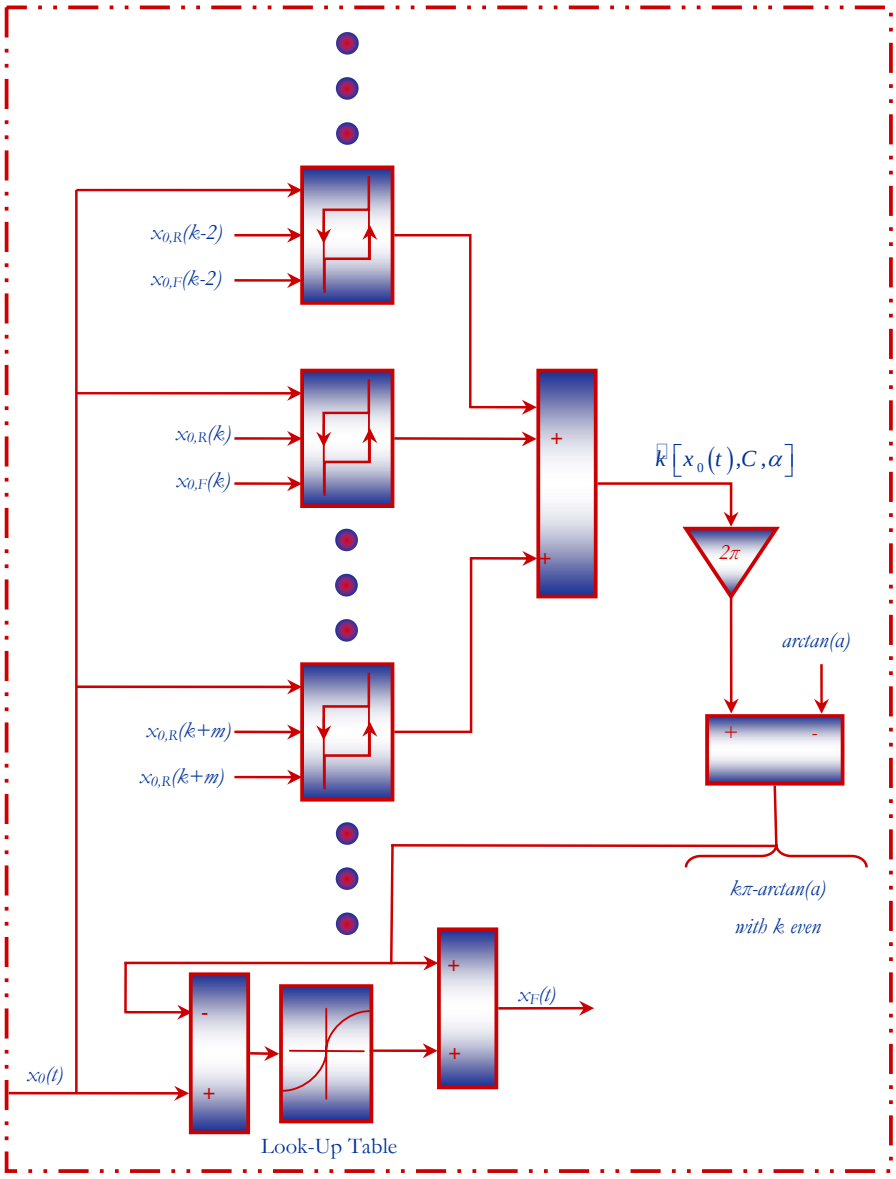

Figure II.3. Bloc diagram of the behavioral model in the case of C>1

After deducing $x_F(t)$ from the bloc diagrams described previously in both cases, the OOP variations can be approximated by applying a cosine function to their outputs.

It can be seen through equation (2.5) that the solution will depend on both factors *a* and *C*. Even thought the linewidth enhancement factor can be directly measured, previous studies showed that, for Fabry-Perot laser diodes, *a* has the only effect of translating the SM signal along the time axis without changing its shape [57]. On the other hand, it is well-known that *C* has a fundamental effect on

the shape of the SM signal. Both these effects will be studied in details farther in this chapter.

II.3. Phase Unwrapping Method

The principle of phase unwrapping method is illustrated in Figure II.4 and can be split up into two principal steps. The first one concerns the rough estimation $\hat{x}_F(t)$ of $x_F(t)$, which is based on remarkable properties of solutions to the non linear phase equation (2.5). Actually it is shown in [17]-[58] that $x_F(t)$ exhibits many discontinuities with phase jumps approximately (for large values for C) equal to 2π. Thereby $\hat{x}_F(t)$ can be retrieved by adding or subtracting 2π to $x_F(t)$, depending on the direction of displacement, every time a discontinuity occurs. After an Automatic Gain Control (AGC) normalizes $P(t)$ making $P(t)/P_0$ ranging over the [-1,1] interval. An arc cosine function is used to get $x_F(t)$ modulo π (Figure II.4). Next the derivative of the $arccos(P(t))$ is thresholded (Figure II.4), and converted to normalized transitions by a transition detector (Figure II.4). Then an integrator adds or subtracts 2π depending on the sign of the discontinuity. This phase correction is an approximation because the actual phase jump depends on C [17]-[58].

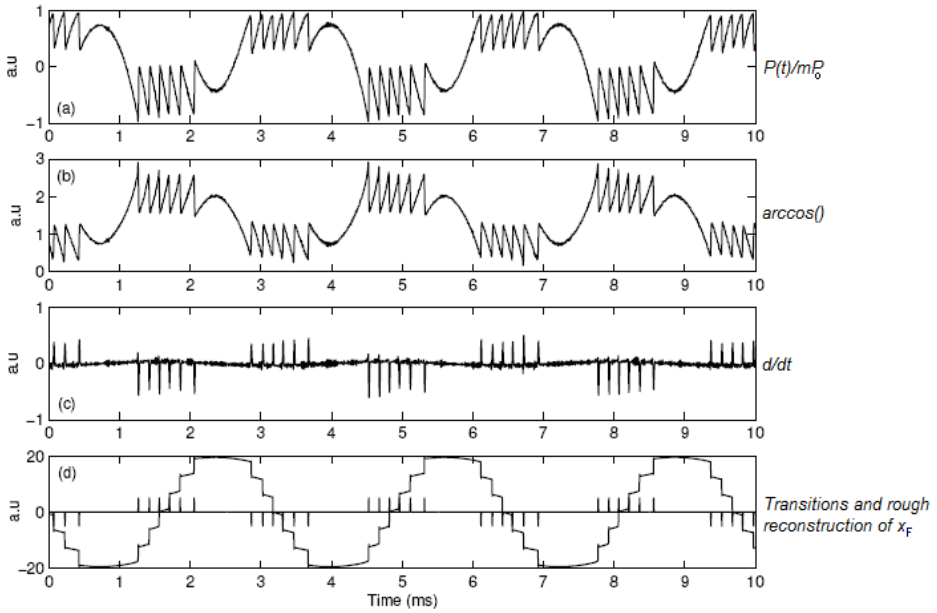

Figure II.4. The first step of the algorithm: (a) Normalized optical output power P(t), (b) arccos(P(t)/mP0), (c)derivative of arccos(P(t)/mP0), (d) Transitions and rough reconstruction of xF (t).

This estimation will be improved by the second step where the signal processing step deals with the joint estimation of *C*, *a* and *D(t)*. The whole procedure is synthesized with the schematic block diagram shown in the following figure.

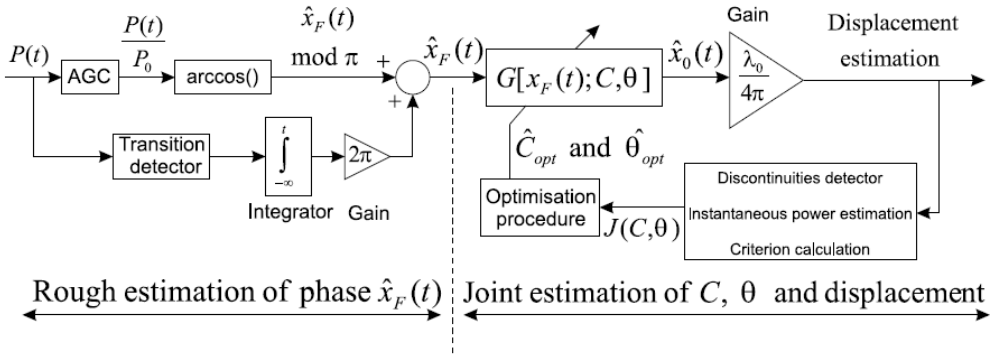

Figure II.5. Complete bloc diagram of the phase unwrapping method.

The algorithm is based on the idea that discontinuities caused by irregular movements of the target are considered far less frequent than discontinuities of *P(t)* and $x_F(t)$ due to the non linear behavior of equations (2.5) and (2.6). This hypothesis is realistic in mechatronics where the target, for example a piezoelectric transducer (PZT), is driven by a sinusoidal signal allowing it to move smoothly.

In this case, equation (2.5) could be then rewritten as follows:

$$x_0(t) = x_F(t) + C\sin\left[x_F(t) + \theta\right] \quad \forall t > 0 \tag{2.9}$$

Where $\theta = x_F(0) + arctan(a)$ is constant. Therefore it is possible to choose an optimal set of parameters $\hat{C}_{opt}$ and $\hat{\theta}_{opt}$ minimizing the discontinuities of the reconstructed phase $\hat{x}_F(t)$ with the Nelder-Mead simplex method, specified by the optimization of the criterion *J(C,θ)* expressed as follows [59]:

$$Arg\min\left(J(C,\theta)\right) = Arg\min\sum_n x_0(n) - x_0(n-1) \tag{2.10}$$

$x_0(n), n \in \mathbb{N}$ being the discrete form of equation (2.5).

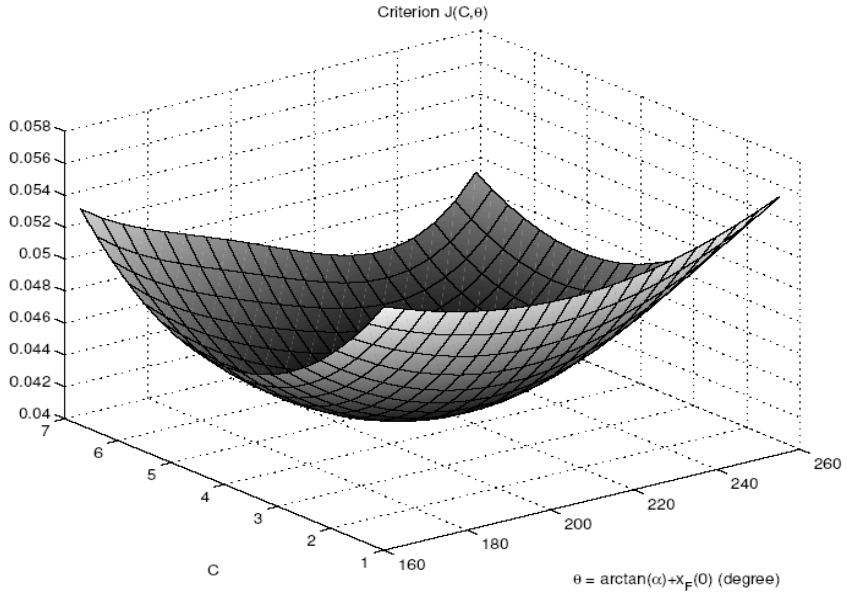

Figure II.6. Criterion J(C,θ) permitting to find the optimal couple ($\hat{C}_{opt}$, $\hat{\theta}_{opt}$)

This criterion depends on the instantaneous power of the reconstructed signal discontinuities. The optimized reconstructed phase $x_0(t)$ is then used to estimate $D(t)$ through equation (2.4).

II.4. Effect of The Linewidth Enhancement Factor

The linewidth enhancement factor effect on the shape of the self-mixing signal is usually considered as a simple transition along the time axis in the case of Fabry-Perot lasers ($4<a<7$) [57].

In fact, Figure II.7 shows simulations of the self-mixing signal, using the model developed in [57], for different values of a of 4 and 7 showing the insensibility of the shape of the self-mixing signal to a in the case of Fabry-Perot lasers, and thereby the signal processing method is not changed by variations of a.

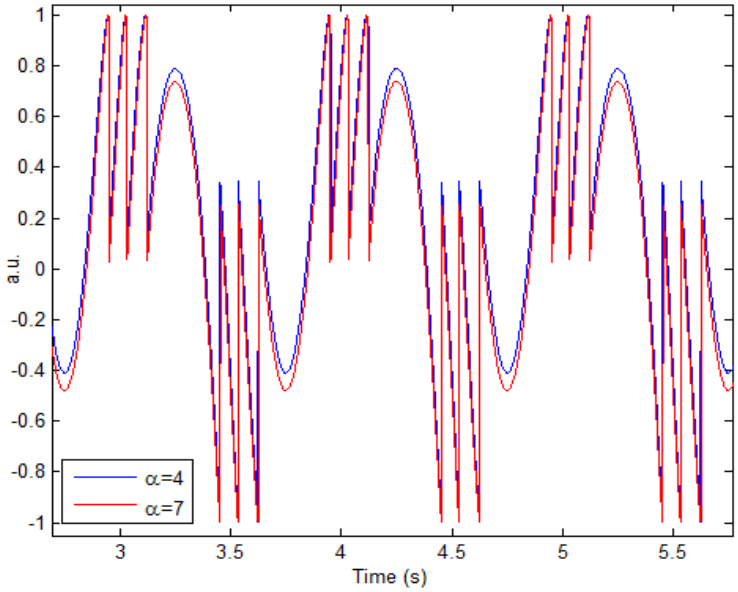

Figure II.7. Self-mixing signal for different values of a=4 (in blue) and 7 (in red)

II.5. Effect of The Coupling Factor C

The previous study of the effect of the linewidth enhancement factor showed that *a* is more of a second order parameter in the case of Fabry-Perot lasers, and thereby in the case of this study where this type of lasers is used. However, the coupling coefficient introduced in equation (2.11) has a major effect, where the number of possible lasing modes, i.e. solutions of equation (2.5), is strongly affected by *C*.

$$C = \varepsilon \frac{\tau_D}{\tau_l} \zeta \sqrt{1+\alpha^2} \qquad (2.11)$$

Therefore, a deeper study of the effect of this coefficient was conducted where the Figure II.8 shows simulations of different self-mixing signals for different values of *C*.

Depending on the number of possible lasing modes, and thereby on the values of *C*, the self-mixing effect has been divided into different regimes of very low feedback (*C=0.1*), low feedback (*C=1*), moderate feedback (*C=7*) and strong feedback (*C=30*). shows the self-mixing signal corresponding to the different values of *C* and the corresponding generating displacement having an amplitude of $8\lambda_0/2$ and a mean value of *1m*.

Figure II.8 shows the strong effect of the coupling coefficient on the shape of the self-mixing signal. For very low feedback the signal peaks (i.e. discontinuities) have a sinusoidal form. If *C* is increased, i.e. into the low feedback regime, the variations of the OOP are continuous and have a sawtoothlike shape. For larger values of *C*, the variations of the OOP begin to present hysteresis, typical symptom of the moderate feedback regime. The more the coupling coefficient increases and the more the hysteresis will be emphasized until arriving to a peak free signal for high values of *C*.

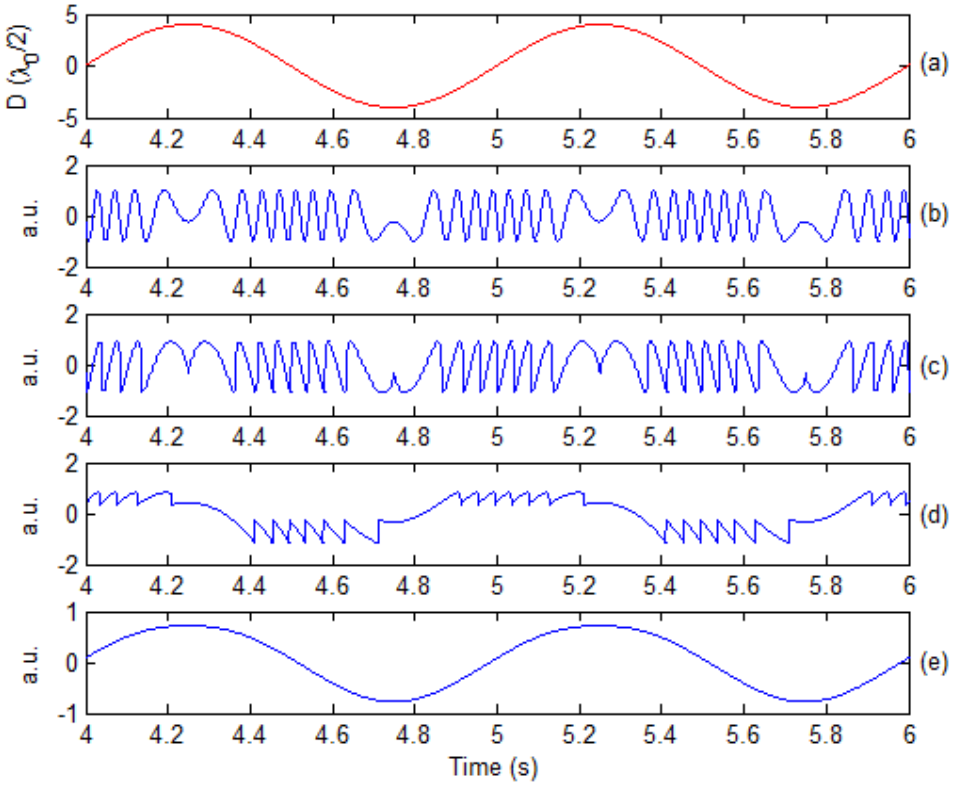

Figure II.8. Simulations of a) the generating displacement having a peek to peek amplitude of 8λ0/2: D(λ0/2) and the self-mixing signal for different values of C b) C=0.1,c) C=1,d) C=7,e) C=30.

The next figure shows a zoom of different parts of the Figure II.8 showing for *C=0.1* the sinusoidal peak, for *C=1* the sawtoothlike peak shown also for *C=3* but this time with hysteresis.

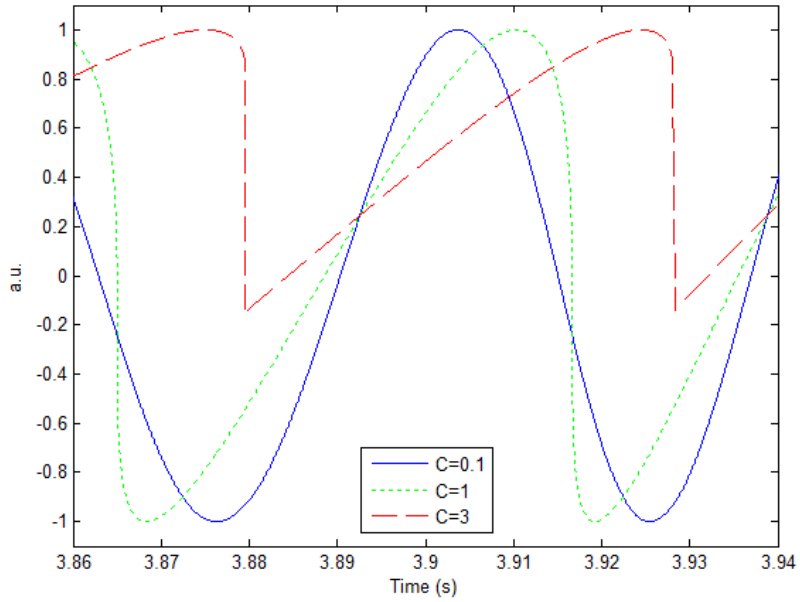

Figure II.9. Effect of C on the shape of the peaks.

All this can be explained by going back to the phase equation (2.5) where for *0.1<C<1* the phase equation has only one solution and the laser emission remains singlemoded and a conventional saw-tooth like signal can be monitored. Now for *1<C<4.6034*, the laser can not be considered theoretically as a singlemode laser anymore because the phase equation can have up to five numerical solutions from which only three can match this relationship and may exist physically [60]. As the system becomes bistable, one of the three solutions is always instable. Though the laser has a propensity to oscillate in the external cavity mode with minimum threshold gain [61], it has been demonstrated that most of the power is in the mode with the narrowest linewidth [62]-[63]-[64]. This is due to a longer duration of oscillation in this mode. Practically, such a property induces that only one among the three possible modes is lasing. Transition from one mode to another occurs as the phase condition is changed because the external round trip delay is slightly modified during the displacement of the target. The frequency separation between upward and downward mode hops depends on *C* [65].

Further increase of the feedback level ($C > 4.6$) corresponds to five potential lasing modes. Even if the criterion of mode hopping is unchanged, the spectral behavior of the laser becomes more complicated because of the increasing number of possible lasing modes.

On the other hand, this hysteresis effect can be explained considering the *F* function defined earlier in the case of moderate feedback where the following figure shows the numerical function and the effective physical behavior of $x_F(t)$ as a function of $x_0(t)$. This late, plotted in bold line, shows the mode hoping of the laser causing the hysteresis effect observed earlier in the self-mixing signal. In fact, when $x_F(t)$ arrives to the value where the derivative of the *F* function is infinite, it changes abruptly. If the temporal variation of $D(t)$ is such as $x_0(t)$ passes from x_{0A} to x_{0D} and back to x_{0A}, then the couple [$x_F(t)$, $x_0(t)$] will follow the trajectory A, B, C, D, E F and back to A. The non linearities of the *F* function will induce a memory effect causing the hysteresis effect [57].

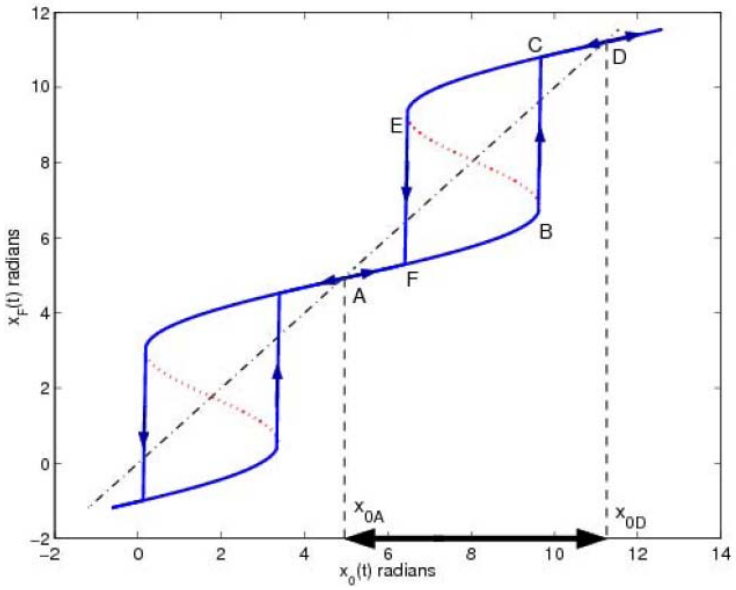

Figure II.10. The F function showing hysteresis (C=3 and a=5): the numerical resolution of equation (2.5) in dotted pink line compared to the physical behavior of the laser diode in blue bold line.

By observing the SM signal depicted in Figure II.8, another characteristic of the moderate feedback signal can be observed. This can be noticed comparing figures a and b with figures c and d where the peaks on the high part of the signal (called "high peaks") has an amplitude less than those on the lower part (called "low peaks"). In fact, Figure II.11 presents the power as a function of the round trip time when the target approaches the laser (a) or moves away from it (b).

The arrows show the physical evolution of the OOP whereas the plain line shows the phase equation presented numerically. It maybe seen that the plain line arrows are smaller than the dotted ones which explains that in a SM signal having

hysteresis, the "high" peaks are smaller than the "low" ones which will be also observed experimentally later in Figure II.17.

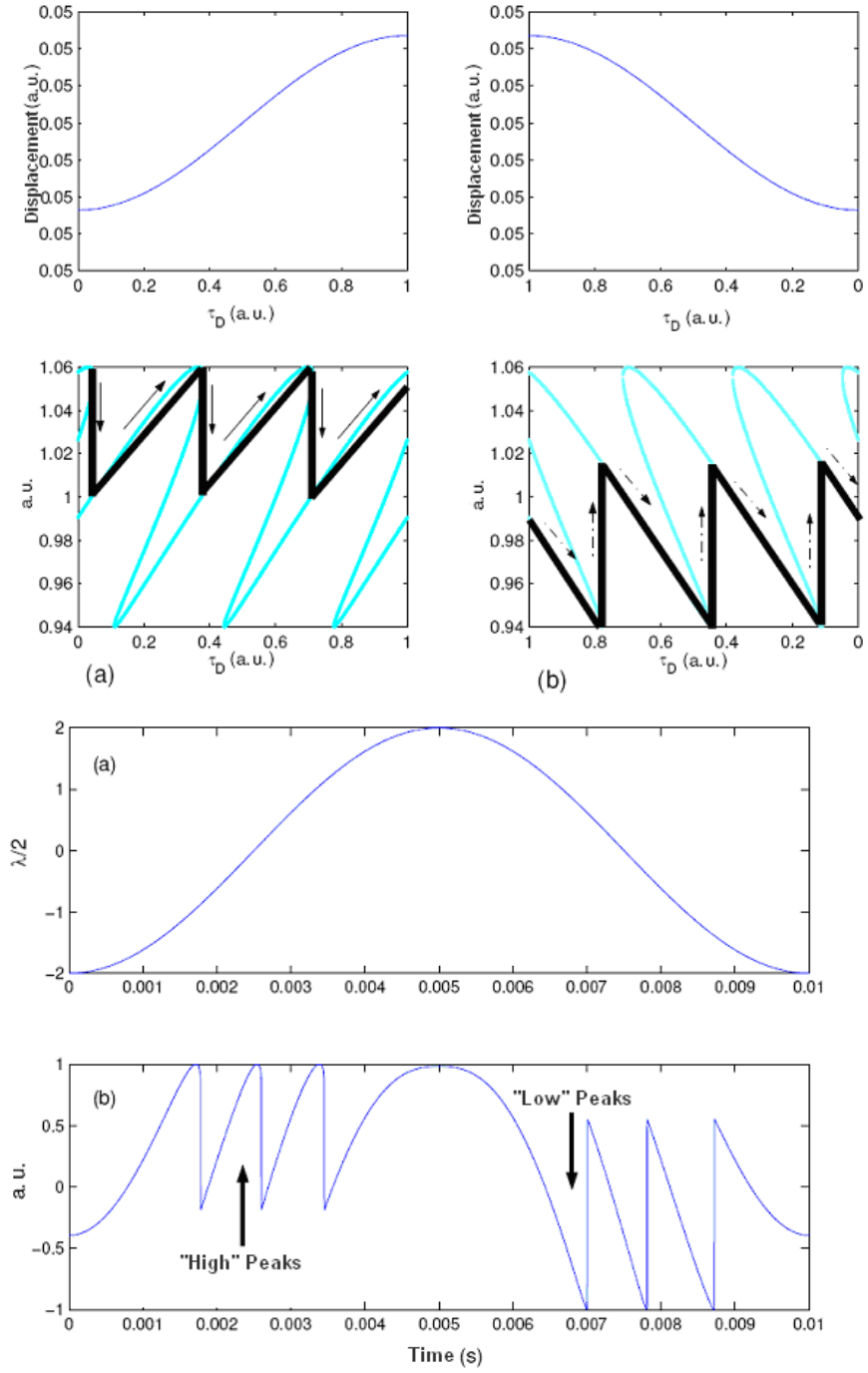

Figure II.11. Plot of OOP as a function of the round trip time in the case of moderate feedback.

II.5.1.a. Variations of The Coupling Coefficient With The Distance:

The coupling coefficient has proven to have a major effect on the self-mixing shape affecting thereby the different signal processing methods to be used in order to accomplish different measurements. Looking at equation (2.11), if everything is perfectly aligned C should be only limited by the coherence length of the laser. This is not the case in reality because different loss parameters will influence (and limit) its variations. Therefore a study of the variations of the coupling coefficient as a function of distance was accomplished through the following experiment.

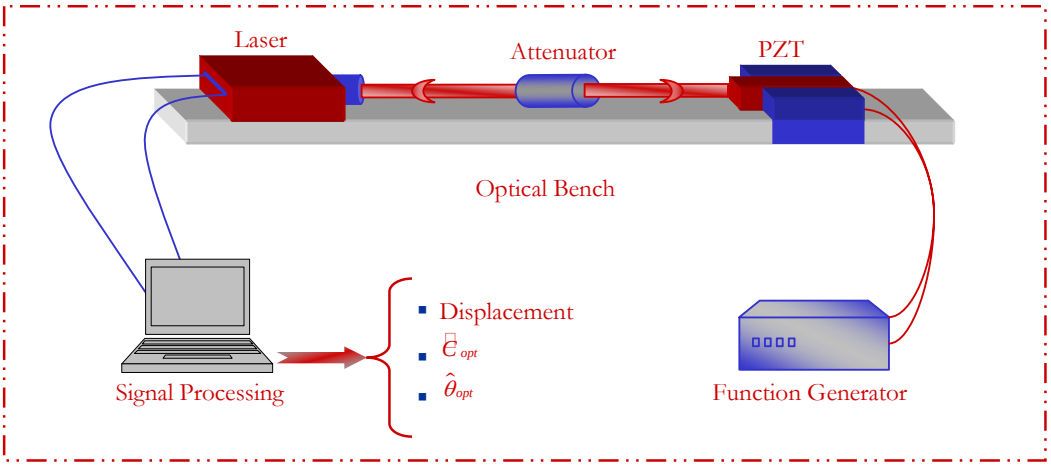

Figure II.12. Experimental setup.

The experimental setup consisted of a LD mounted in front of a vibrating piezoelectric transducer (PZT) that could have been moved farther or closer, changing thereby the distance separating the LD and the PZT. An attenuator was added to the setup in order to keep C in the limitations of the SM behavioral model [57]. In order to eliminate the fading due to the speckle effect [66], an adhesive micro-prism surface was added on the reflecting facet of the target.

The first experiment depicted the variations of the coupling coefficient as a function of distance; the resulting curve is plotted in Figure II.13.

Difficulties were caused by the mechanical alignment inducing the local variation of C on the reflecting surface of the PZT and required thereby to hit the same point of the surface at every data acquisition. This was accomplished by setting a reference point and pointing it each time a measurement was done.

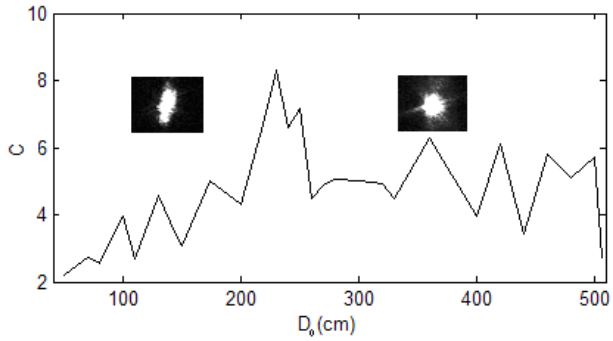

Figure II.13. Variation of C as a function of the distance D0 with corresponding photos of the laser beam.

Figure II.13 shows that first, for short distances (less than 2 meters), *C* tends to increase with distance, which can be seen in equation (2.11) where the gain brought by τ_D (due to the increase of *D*) will be greater than the losses expressed by ε (generally considered as a constant from 0.16 to 0.5 [67]-[68]) and by the attenuation expressed in ζ. This will be sustained until a certain distance where *C* will reach its maximum value (limited in the case of this experiment to a value of *8* because of attenuation). Then the losses will overtake the added gain causing the values of *C* to drop.

Another augmentation in the values of *C*, caused this time by the shape of the collimated laser beam was observed at a distance around *3.5 m*. This may be understood considering the different shapes of the beam spot shown in the photos added to the curve in Figure II.13. In fact, at short distances the spot is ellipsoidal with its major axis directed vertically; it becomes more circular as the distance increases causing thereby more energy to be injected in the laser cavity and inducing a higher coupling coefficient. If the distance *D* is increased more, the spot will lose its circular shape changing back to the elliptical shape with a horizontal major axis this time.

The experiment was repeated several times in different conditions. Figure II.14 shows another repetition for short distances where a smoother beginning of the curve can be noticed. In this curve higher values of *C* were obtained because of the absence of attenuation, the peak value of *C* was, this time, around *140 cm* being caused by the variation of the experimental conditions (i.e. temperature, attenuation, target …).

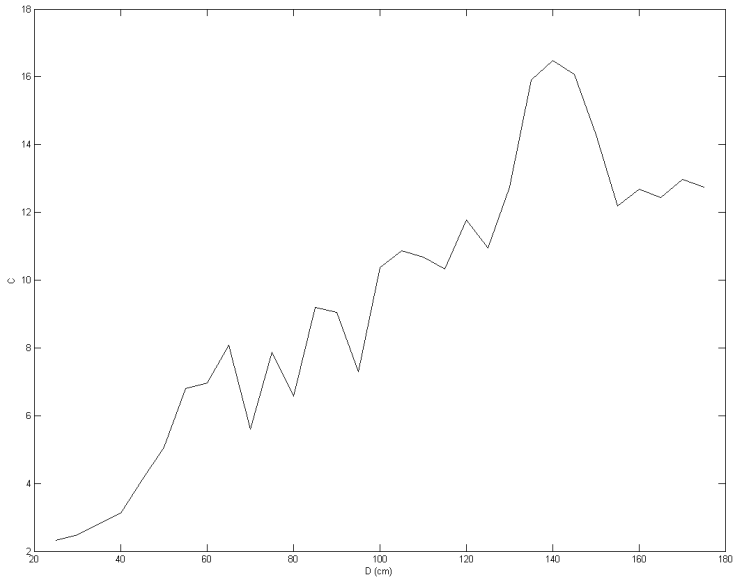

Figure II.14. Measurements of the coupling coefficient for short distances.

As mentioned earlier, if the target is taken farther from the laser, losses become more important and *C* decreases more and more which is also shown in the Figure II.15 representing another experience with different circumstances (room and junction temperature, attenuation and distances).

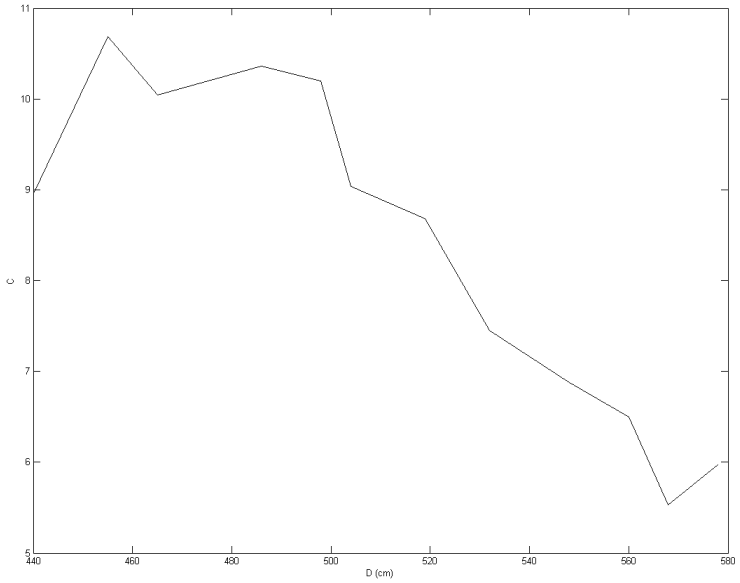

Figure II.15. Measurements of the coupling coefficient for far distances.

Again, the peak value of *C*, caused by the waist of the collimated beam, is observed this time around *4.7* to *5* meters shown clearly in the previous curve.

Looking again at equation (2.11) it can be seen that *C* is also influenced by the surface of the target through different parameters such as ε and ζ. This was shown

through the following experiment where the variations of C for a given constant laser-target distance (D_0=*40 cm*) was measured by translating the laser spot on the surface of an adhesive micro-prisms adhesive paper. The result is depicted in Figure II.16 where variations of C between the values of *1.9* and *5* can be noticed. This will complicate any measurement requiring a constant value of C since it becomes very crucial to hit exactly the same point from the same distance.

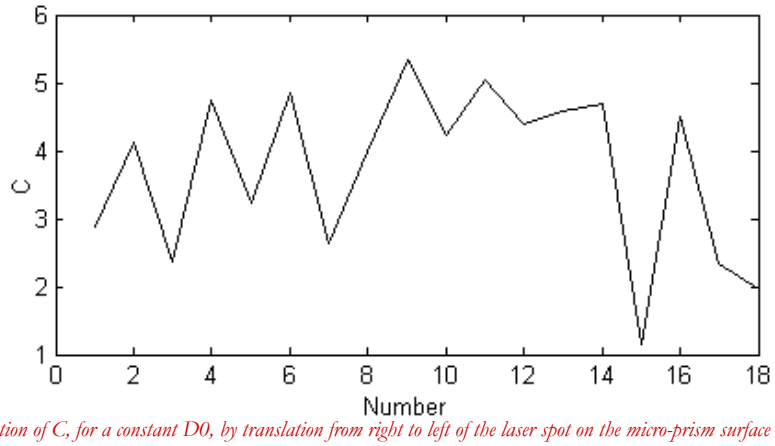

Figure II.16. Variation of C, for a constant D0, by translation from right to left of the laser spot on the micro-prism surface in function with the number acquisitions.

II.6. Study of a Self-Mixing Signal under Moderate Feedback

II.6.1. Observations in The SM Signal under Moderate Feedback:

As mentioned earlier, the different SM signals presented in Figure II.8 correspond to the same displacement and were obtained just by changing the coupling coefficient. However, it can be noticed that the number of peak is not the same for all those signals although the displacement's amplitude was kept constant ($10\lambda_0/2$) (i.e. for C=*0.1* and *1* the number of peaks was *10* whereas for C=*7* it dropped to *9* and for C=*17* to *5*).

This "loss of peaks" was also observed in experimental signals as Figure II.17 shows. Signals in this figure, taken from the previous experiment depicting C as a function of distance, shows a diminution of the number of peaks from *3* peaks at the distance of *50cm* where C=*2.21*, to *2* peaks at the distance of *173 cm* where C=*5* and farther to only one peak at the distance of *230 cm* and a C=*8.32* (same

for the distance of *250 cm* and *C=7.17*). *C* was calculated using the method developed earlier in [30].

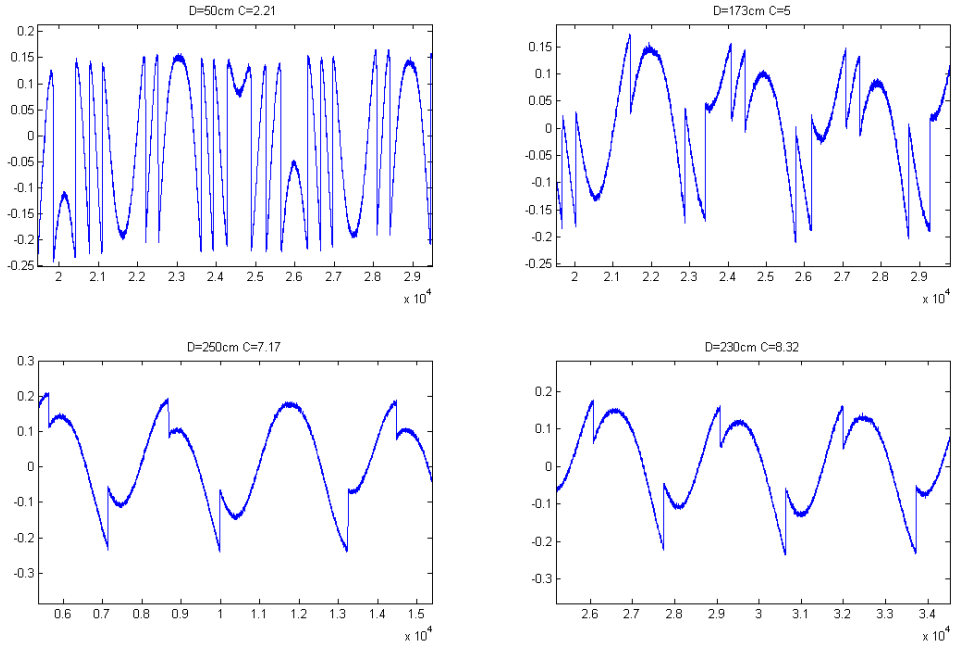

Figure II.17. Experimental Signals Showing Peak Disappearance.

This peak disappearance can be seen even better looking, in Figure II.18, at the simulations of the *F* function for different values of *C* of respectively *2*, *4*, *12* and *16* keeping always the same value of the displacement's amplitude and the same value of the initial laser to target distance.

The following figure is another proof of the loss of peaks where looking at the discontinuities of the *F* function, that corresponds to the peaks of the SM signal, their number diminishes from *6* in the case of *C=2* (corresponding to the $3\lambda_0/2$ displacement), to *5*, *3* and *2* in the case of respectively *C=4*, *12* and *16*.

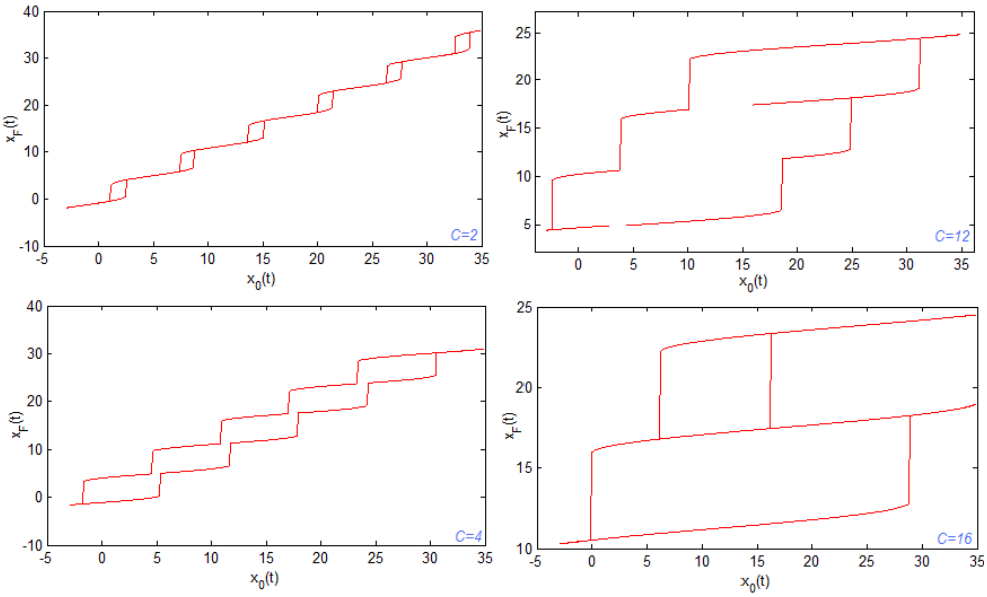

Figure II.18. Simulations of the F function for different values of C respectively of 2, 4, 12 and 16.

Looking even closer at this loss of peaks issue, a displacement with an amplitude of $8\lambda_0/2$ having then *16* peaks in its self-mixing corresponding signal was simulated. The variation of the number of peaks due to different levels of feedback was studied for a continuous variation of *C*. Table II.1 shows the values of *C* corresponding to the disappearance of each pair of peaks respectively (i.e. the Peak Nb. corresponds to the number of the pair of peaks disappearing). Since peaks are disappearing from both the upper and lower parts of the signal, the discussion will be conducted around the loss of pair of peaks and not peaks anymore.

In fact, it was noticed that the peaks disappear each pair after the other, i.e. one peak from the upper part of the signal and the other from its lower part. In fact, Figure II.19 shows the simulation of a self-mixing signal for a $C=1$ generated by a displacement having a peak to peak amplitude of $a=8\lambda_0/2$ and the corresponding self-mixing signal for $C=4$. The first signal exhibits 16 peaks whereas the other signal shows only 14 peaks and that considering a displacement period meaning a peak disappeared from the upper side of the signal (corresponding to the target moving away from the laser) and another peak disappeared from the lower part (corresponding to the movement in the other direction).

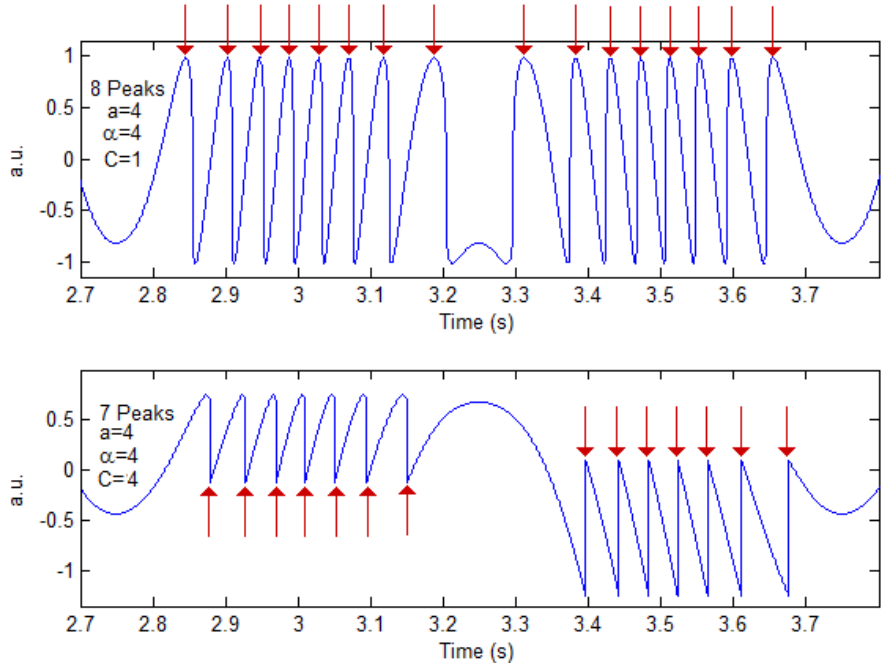

Figure II.19. Pair of peaks disappearance.

Peak Nb.	C	ΔC_1 - $\angle C'_1$	ΔC_2
1	*2.7*	2.7	*6.3*
2	*6.3*	*3.6*	
3	*9.25*	2.254	*6.354*
4	*13.35*	*4.1*	
5	*15.5*	*2.15*	6.35
6	*19.7*	*4.2*	
7	22.3	2.6	6.2
8	*25.9*	*3.6*	
9	28.5	2.6	6.25
10	*32.15*	*3.65*	

Table II.1. Consecutive peak disappearance for continuous variation of C.

The values of *C* corresponding to the disappearance of ten peaks, noted in Table II.1, shows that the first peak disappears for *C=2.7* whereas the second peak disappears for *C=6.3*. Let $\angle C_1$ and $\angle C'_1$ be the needed feedback level to be added in order to make an odd or even numbered pair of peaks disappear respectively and $\angle C_2$ the needed feedback to make two pairs of peaks disappear. Then, it can be noticed that for the disappearance of the odd numbered pair of peaks (pair of peak number *1*, *3*, *5*, …), noted in italic, a feedback increase of $\angle C_1=2.46$ was needed; whereas, for even numbered pair of peaks (in bold) a higher average value was needed ($\angle C'_1=3.83$) giving us therefore an average step of $\angle C_2=6.29$ needed for the disappearance of two pairs of peaks.

Moreover, in the self-mixing signal, a movement of amplitude $n^* \lambda_0/2$ will have 2^*n peaks due to the movement in both directions. So, the disappearance of the last pair of peaks of a displacement (corresponding to the value of C noted Cm) with variable amplitude varying from $\lambda_0/2$ to $20\lambda_0/2$ was studied and the results were depicted in the following table:

Amp. ($\lambda_0/2$)	Cm	Amp. ($\lambda_0/2$)	Cm
1	7	11	70
2	14	12	77
3	20	13	83
4	26	14	89
5	33	15	96
6	39	16	102
7	45	17	108
8	52	18	114
9	58	19	121
10	64	20	127

Table II.2. Disappearance of the last pair of peaks of a displacement with variable amplitude varying from $\lambda_0/2$ to $20\lambda_0/2$

Looking back again at the difference between two consecutive rows it is possible to find again ΔC_2 as this experiment comes back to looking at each of the disappearances of the following pair of peaks of a displacement of $20\lambda_0/2$. This experiment will reveal its importance during the study of strong feedback signals in the next chapter. However, it is interesting to look again at the average value of ΔC_2 being in this case of *6.316*, in the case of Table II.2, showing approximately a quasi-constant value.

Finally, considering the above results the step of disappearance of two pairs of peaks is quasi-constant and has an average value of $\Delta C_2=6.3$ (from both Table II.1 and Table II.2). Despite the difficulty of setting a threshold accurately for peak disappearance leading to a bad resolution, the results in both simulations were similar with a relative error less than *1%*.

II.6.2. Interpretation of The Peak Disappearance:

Looking back at the F function it can be plotted again defining this time φ as the position of $x_0(t=0)$ relatively to the corresponding $k\pi$-θ (Figure II.20), it can be written as follows:

$$\varphi = 2\pi\left\{D\left(t=0\right) - \mathrm{int}\left[D\left(t=0\right)\right]\right\} \tag{2.12}$$

Afterwards, the rising and falling edges of the F function ($x_{0,R}(k)$ and $x_{0,F}(k)$ respectively) can be defined as being the points where its derivative in equal to zero. This leads to the following expressions of $x_{0,R}(k)$ and $x_{0,F}(k)$ respectively [57]:

$$x_{0R}\left(k\right) = k\pi - \theta + \beta + C\sin\left(\beta\right) \tag{2.13}$$

$$x_{0F}\left(k\right) = \left(k+2\right)\pi - \theta - \beta - C\sin\left(\beta\right) \tag{2.14}$$

Where $\beta = \arccos\left(-1/C\right)$.

Finally, $x_0(t=0)$ is the value of x_0 corresponding to the displacement at $t=0$ and a_m is also the corresponding amplitude of $x_0(t)$ caused by the variations of amplitude of $D(t)$ a: $am=a/2\pi$.

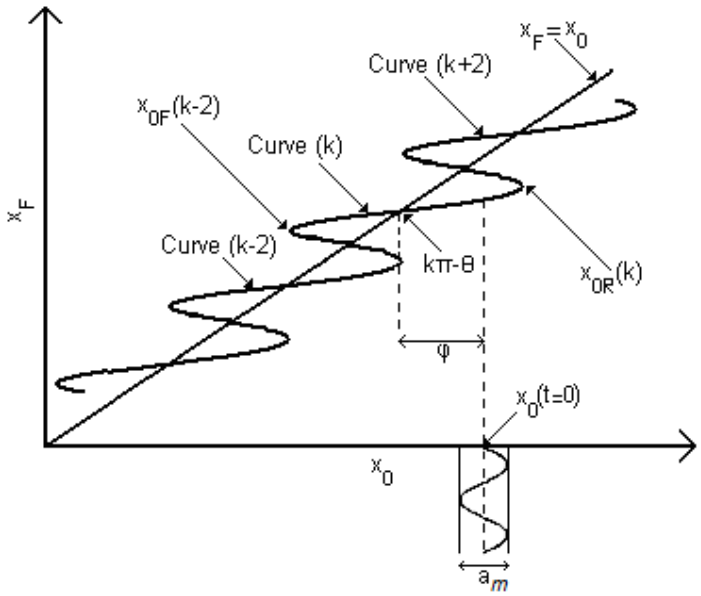

Figure II.20. Plot of function $x_F\left(t\right) = F\left[x_0\left(t\right);C,\alpha\right]$ *moderate or strong feedback*

This figure, shows that, for $C>1$, the F function can be conceived as a juxtaposition of different segments *Curve (k-2)*, *Curve (k)*, *Curve (k+2)*,… with k an even integer [57].

Now, in order to explain the disappearance of peaks; the opposite problem of peak appearance will be considered. In fact, a new pair of peaks appear when the amplitude variation of the phase $x_0(t)$ around φ exceeds $x_{0,F}(k-2)$ or $x_{0,R}(k)$ passing thereby to the next line corresponding to $k-2$ or $k+2$ consecutively causing a

discontinuity in the signal and generating thereby a pair of peak in the self-mixing signal.

These conditions can be written successively as follows:

$$\frac{x_{0F}(k-2)-x_{0R}(k)}{2}-\varphi\le\frac{a_m}{2} \tag{2.15}$$

$$\frac{x_{0F}(k-2)-x_{0R}(k)}{2}+\varphi\le\frac{a_m}{2} \tag{2.16}$$

The equation (2.15) corresponds to variations of x_0 exceeding $x_{0F}(k-2)$; whereas, equation (2.16) corresponds to x_0 exceeding $x_{0R}(k)$.

Then the limit condition for peak appearance can be written as follows:

$$\frac{x_{0F}(k-2)-x_{0R}(k)}{2}\pm\varphi=\frac{a_m}{2} \tag{2.17}$$

Substituting $x_{0R}(k)$ and $x_{0F}(k-2)$ by their expressions defined respectively in (2.13) and (2.14) the limit condition expressed previously in (2.17) could be rewritten as follows:

$$\frac{1}{2}\left|k\pi-\theta-\beta-C\sin(\beta)-k\pi+\theta-\beta-C\sin(\beta)\right|\pm\varphi=\frac{a_m}{2} \tag{2.18}$$

This can be expressed more clearly as follows:

$$2\beta+2C\sin(\beta)\pm2\varphi=a_m \tag{2.19}$$

$$\gamma=\beta+\sin(\beta) \tag{2.20}$$

γ, defined in equation (2.20), is a non linear term that can be approximated using an asymptotic development as shown in the following equation:

$$\begin{aligned}\beta+\sin(\beta)&\approx C+\frac{\pi}{2}+\frac{1}{2C} && \text{Second Order Developpement}\\ &\approx C+\frac{\pi}{2} && \text{First Order Developpement}\end{aligned} \tag{2.21}$$

Considering a first order development equation (2.19) can be approximated as follows:

$$2\left(C+\frac{\pi}{2}\right)\pm2\varphi\approx a_m \tag{2.22}$$

This last equation gives the approximate values of C corresponding to a peak appearance when exceeding $x_{0R}(k)$ (C_1) or $x_{0F}(k-2)$ (C_2).

$$C_1 = \frac{-\pi - 2\varphi + a_m}{2}$$
$$C_2 = \frac{-\pi + 2\varphi + a_m}{2} \quad (2.23)$$

With $0 \le \varphi \le \beta + C\sin(\beta)$. For C_1 to exist a_m must satisfy the following condition $a_m \ge \pi + 2\beta + 2C\sin(\beta)$ where as for C_2 it will be $a_m \ge \pi - 2\beta - 2C\sin(\beta)$.

It is to be noticed that if, $\varphi = 0$ meaning that the variation of $x_0(t)$ is centered at $k\pi - \theta$, both the two pairs of peaks will appear at the same time which is logical considering Figure II.20 because both $x_{0,F}$ and $x_{0,R}$ moves at the same speed.

Next, the condition of appearance of the next pair of peaks will be considered, this will happen for:

$$\frac{x_{0F}(k-4) - x_{0R}(k+2)}{2} \pm \varphi = \frac{a_m}{2} \quad (2.24)$$

Leading to values of C (C'_1 and C'_2) that can be written as follows:

$$C_1^{'} = \frac{-5\pi - 2\varphi + a_m}{2}$$
$$C_2^{'} = \frac{-5\pi + 2\varphi + a_m}{2} \quad (2.25)$$

It is possible now to calculate the equivalent feedback needed for the appearance of a pair of peaks or what was previously called $\angle IC_2$:

$$\Delta C_2 = C_1 - C_1^{'} = C_2 - C_2^{'} = 2\pi \approx 6.28 \quad (2.26)$$

This expression can only confirm the observation of a constant $\angle IC_2$ made earlier and this independently from the different laser parameters like θ or k or even the initial conditions such as φ and the initial value of the coupling coefficient. This means that whatever the amplitude of variation of $x_0(t)$ (thereby displacement), whatever is the initial distance separating the laser diode and the target D_0 (thereby C_0 and φ) adding a feedback equivalent of $\Delta C_2 = 2\pi$ causes an extra pair of peaks to disappear from the SM signal.

All these results were encountered throughout simulations using the model developed in [57] where in both experiments (Table II.1 and Table II.2) the error encountered on the value of $\angle IC_2$ was *0.17%* in the first experiment and *1.1%* in

the second which is acceptable taking into account the difficulty of finding the exact value of C corresponding to the disappearance of peaks in both cases.

Moreover, the first simulation was conducted for a $D(t=0)=20mm$, then the corresponding φ, calculated using equation (2.12), will be $\varphi = 0.707(2\pi)$. As stated before, $\varphi=0$ or $\varphi=2\pi$ corresponds to both pairs of peaks appearing (or disappearing) at the same moment which can be written as $\measuredangle C_1=\measuredangle C'_1$. Now if the relationship between φ on one side and $\measuredangle C_1$ and $\measuredangle C'_1$ on the other side is approximated by a linear relationship then it is possible to express $\measuredangle C_1$ and $\measuredangle C'_1$ as follows:

$$\left.\begin{array}{c} if\ \varphi = 2\pi \\ \Updownarrow \\ \Delta C_1/\Delta C'_1 = 1 \end{array}\right\} \Leftrightarrow \left\{\begin{array}{c} if\ \varphi = 0.707(2\pi) \\ \Updownarrow \\ \Delta C_1/\Delta C'_1 = 0.707 \end{array}\right. \qquad (2.27)$$

On the other hand, through simulations shown in Table II.1 $\measuredangle C_1/\measuredangle C'_1$ had an average value of 0.643 instead of 0.707 leading to a relative error of 9% due to the imprecision of determination of the exact moment of disappearance of a pair of peaks and the approximation of linearizing equation (2.27).

II.6.3. Effect of The Initial Position through φ

The position relative to $k\pi$-θ, φ, was defined in (2.12). Simulations showed that φ has no effect on the value of $\measuredangle C_2$, however, it affects the values of $\measuredangle C_1$ and $\measuredangle C'_1$ this means that it will affect the feedback level at which each of the two pairs of peaks will disappear within the 2π interval.

n	φ=-π/3			φ=π		
	C	ΔC1 / ∠C'1	ΔC2	C	ΔC1 / ∠C'1	ΔC2
1	2.408	2.408		2.71	2.71	
2	6,730	4.322		6.451	3.741	
3	8.845	2.115	6.437	9.125	2.674	6.415
4	13.052	4.207	6.322	12.773	3.648	6.322
5	15.152	2.1	6.307	15.431	2.658	6.306
6	19.348	4.196	6.296	19.069	3.638	6.296
7	21.445	2.097	6.303	21.724	2.655	6.293
8	25.635	4.19	6.287	25.358	3.634	6.289

Table II.3. Simulations of the SM signal for a continuously varying values of C for two different values of D_0 (φ)

In fact, Table II.3 shows the simulation of the disappearance of eight consecutive pairs of peaks for two different values of $\varphi=-\pi/3$ and $\varphi=\pi$. This table permits to show the absence of any effect of φ on the values of $\angle C_2$ and to show however its influence on the values of $\angle C_1$ and $\angle C'_1$.

Investigating more this influence, $\angle C_1$ and $\angle C'_1$ were calculated through simulations with the same amplitude of displacement but with different values of φ as shown in the following table.

φ	ΔC_1	$\angle C'_1$	$\gamma-\varphi$
0	6.3	6.3	6.3287
$\pi/5$	1.32	5.05	5.4878
$\pi/4$	1.61	4.76	4.713
$\pi/3$	2.15	4.228	4.1892
$\pi/2$	3.17	3.23	3.149
$3\pi/5$	4.34	2.1	2.097
$2\pi/3$	4.06	2.4	2.518
π	6.4	6.2	6.295

Table II.4. Different values of $\angle C_1$ and $\angle C'_1$ for different values of φ for a constant amplitude of vibration

Table II.4 showed calculation of $\gamma-\varphi$, where the value of C at which a pair of peaks disappears was considered in order to calculate γ and the mean value was considered. It can be observed through this table that $\angle C'_1 \approx \gamma-\varphi$ and $\angle C_1 \approx 2\pi-\gamma+\varphi$, this observation being made with a relative error of *2.4%*. It is also to note that this effect was symmetric relatively to $\varphi=0$ where considering negative values of φ will give the same values as the ones obtained in Table II.4.

II.6.4. Mechanism of Peak Disappearance

Now that the instance of disappearance in terms of feedback level is calculated, the next step is to look closer at the mechanism of peak disappearance in order to understand more how these peaks are disappearing.

While investigating the mechanism of disappearance, it was observed that in fact there were two different mechanisms one for the odd numbered pair of peaks and the other for the even numbered ones.

In fact, Figure II.21 shows the disappearance of a pair of peaks from a SM signal generated by a $10\lambda_0/2$ displacement. The SM signal corresponding to a

C=2.42 is plotted with a plain line, to *C=2.6* with a dashed line and to *C=3* with a dotted line.

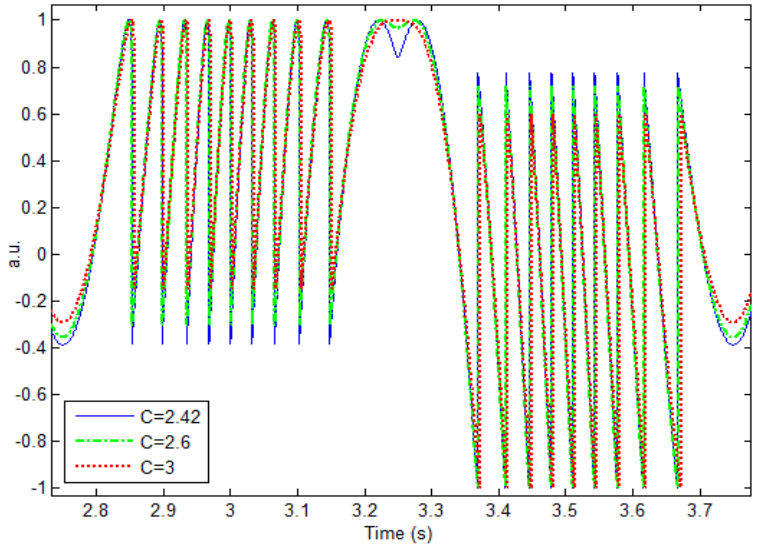

Figure II.21. Odd numbered pair of peaks disappearance

It can be seen that for the odd numbered pair of peaks the disappearance happens in the higher part of the signal where the two small peaks diminishes until disappearing completely as it is shown for the dotted curve.

Whereas the following figure shows the disappearing of even numbered pair of peaks happening at the lower part of the curve.

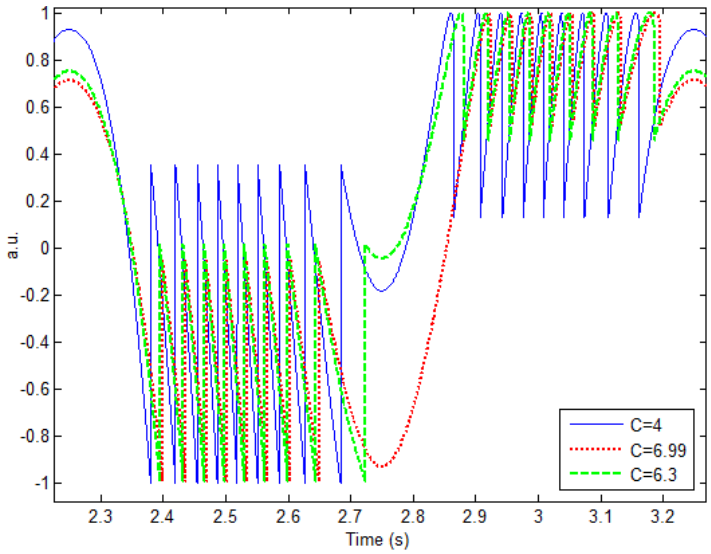

Figure II.22. Loss of an even numbered pair of peaks from the lower part of the signal (C=4 plain line, C=6.99 dotted line and C=6.3 dashed line)

This figure shows how the peak will diminish continually as seen from *C=4* to *C=6.3* until disappearing and passing directly to the next peak as seen for *C=6.99*

leading to the loss of a peak in both the higher and lower parts of the signal and thereby a pair of peaks.

Now looking at the effect of φ on the mechanisms of peak disappearance, the whole interval of variation of φ was considered i.e. between $-\pi$ and π. As stated earlier, simulations shows a symmetry of the effect of φ according to $\varphi=0$. In fact, Figure II.23 shows a comparison between the disappearance of the same pair of peaks in the cases of $\varphi=\pi/2$ and $\varphi=-\pi/2$ for the same value of C where the pair of peaks disappear from the upper part of the signal in the case of $\varphi=\pi/2$ and from the lower part in the case of $\varphi=-\pi/2$, confirming thereby the symmetry according to $\varphi=0$.

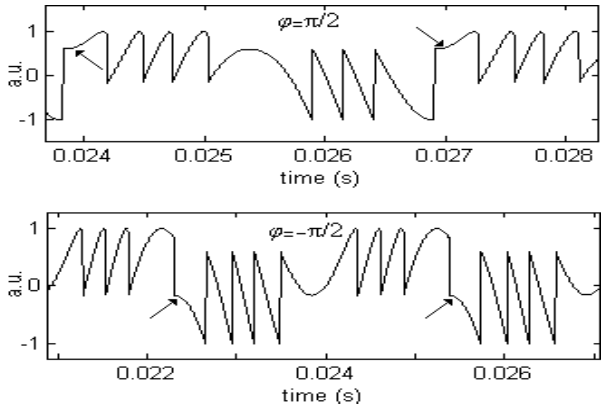

Figure II.23. Comparison between the disappearance of a peak for both $\varphi=\pi/2$ and $\varphi=-\pi/2$ both for C=2.97.

Looking now at where the missing peaks disappear, signals for $\varphi=0$ and for different values of C were simulated and plotted in Figure II.24.

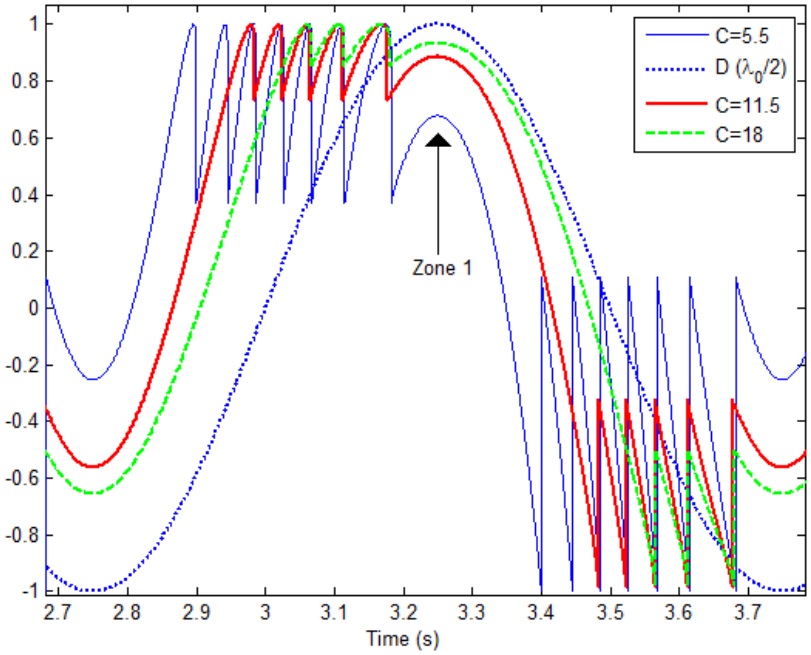

Figure II.24. Simulations showing time differences between consecutives peak disappearances.

This figure shows that for *C=5.5* (OOP having 6 peaks) the time occupied by the "zone 1" indicated in Figure II.24 is $8.4*10^{-4}s$; whereas, for *C=11.5* (having 4 peaks) it is $11*10^{-4}s$ and finally, for *C=18* (having 2 peaks) it is $13.6*10^{-4}s$.

On the other hand, the time occupied by one peak has an average value of approximately $1.32*10^{-4}s$. The difference between two consecutive disappearances (between *C=5.5* and *C=11.5* or between *C=11.5* and *C=18*) is $2.6*10^{-4}s$ corresponds to approximately double the time occupied by one peak. Thereby, it could be concluded that when the two pairs of peaks disappear (simultaneous two pairs since $\varphi=0$) half of them going inside the upper part of the signal corresponding to the change of the displacement's direction (zone 1) and the other half going to the lower part. Thereby, this part of the signal will not represent anymore only the excess fringes but will contain also all the disappeared peaks.

II.6.4.a. Calculation of The number of Peaks in SM Signal:

After establishing conditions of appearance/disappearance of peaks and understanding how these peaks appear or disappear the next step will be to

determine the number of pair of peaks (N) in a certain SM signal knowing the value of the corresponding φ and C.

In fact, each time a discontinuity appears in the SM signal the number of pair of peaks N in increased by *1*. Thereby, this number can be seen as equal to the number of intervals $x_{0,F}(k)$-$x_{0,R}(k)$ (corresponding each to a signal's discontinuities) present in the variation interval of x_0 corresponding to $\overline{x_0} \pm 2a_m\pi$ (Figure II.25).

x_0 can be written as follows:

$$x_0(t) = 2\pi\frac{D(t)}{\lambda_0/2} = k\pi - \theta + 2\pi a_m \sin(2\pi f_M t) + \varphi \tag{2.28}$$

Where f_M is the mechanical vibration frequency whereas, φ can be seen as the mean value of $x_0(t)$ relatively to $k\pi$-θ (Figure II.20) which allows us thereby to calculate its mean value (Figure II.25) as follows:

$$\overline{x_0(t)} = 2\pi\frac{\overline{D(t)}}{\lambda_0/2} = k\pi - \theta + \varphi \tag{2.29}$$

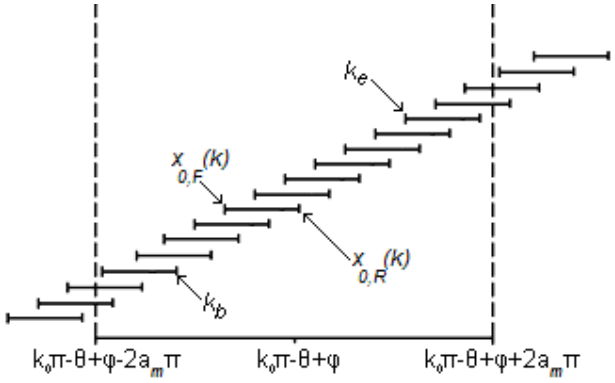

Figure II.25. Calculation of the number of intervals x0,F(k)-x0,R(k) present in the variation interval of x0 corresponding to ±2aπ.

Looking back at the expressions of $x_{0,F}(k)$ and $x_{0,R}(k)$ defined in equations (2.15) and (2.14), then, the expressions of k_b and k_e, numbers of the first and last segments of $x_{0,F}(k)$-$x_{0,R}(k)$ completely included in the variation interval of x_0, can be exploited as follows:

$$k_b = 2 + 2floor\left[\frac{(k-2)\pi + \varphi + \gamma - 2a_m\pi}{2\pi}\right] \tag{2.30}$$

$$k_e = 2floor\left[\frac{k\pi + \varphi - \gamma + 2a_m\pi}{2\pi}\right] \tag{2.31}$$

Where "*floor*" is the function giving the lower integer part of its argument, leading, finally, to the following expression of N:

$$N = \frac{k_e - k_b}{2} + 1 \qquad (2.32)$$

Equation (2.32) allows the calculation the number of pair of peaks and to study how N is influenced by the different parameters such as C, φ and the amplitude of displacement.

First of all, the effect of C will be studied for a fixed amplitude of displacement and a fixed value of φ. As expected, Figure II.26 shows a step function that diminishes by *2* every time C is increased by approximately 2π which confirms the theory developed earlier in equation (2.26).

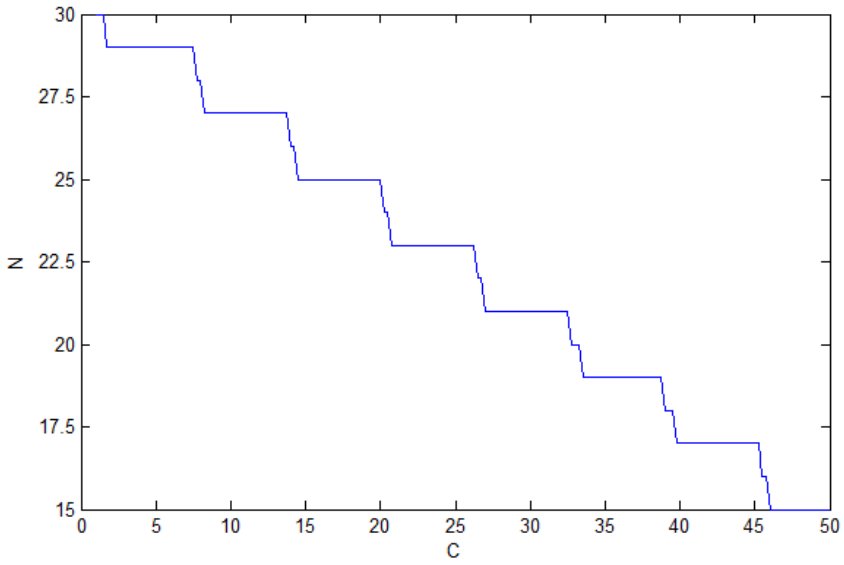

Figure II.26. Number of pairs of peaks N as a function of C for constant amplitude of variation and a constant value of φ.

Furthermore, it was seen before that φ affects only the values of $\measuredangle C_1$ and $\measuredangle C'_1$ and not $\measuredangle C_2$ (Table II.4). This is shown in Figure II.27 where the whole interval of variation of φ was considered between $-\pi$ and π. N was diminished only by one pair of peaks proving also the symmetry to $\varphi=0$.

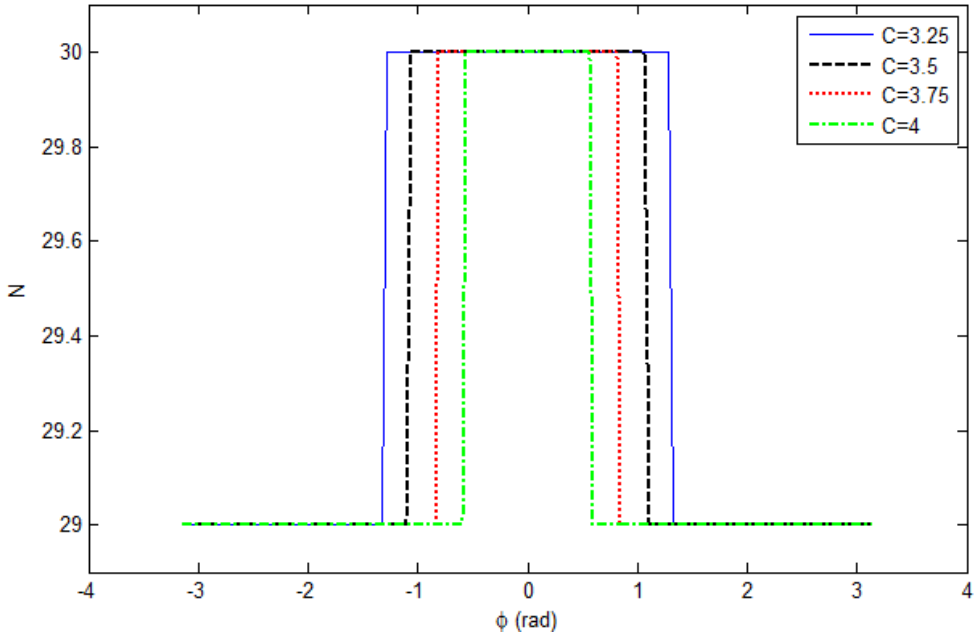

Figure II.27. Effect of φ on the number of peaks.

Another interesting information can be seen in this figure where if *C* increases, the first pair of peaks will disappear for smaller values of *φ*.

Finally the effect of the displacement's amplitude was studied where it revealed to have a linear effect when *C* is constant since adding $\lambda_0/2$ to the amplitude will add a pair of peaks to the SM signal.

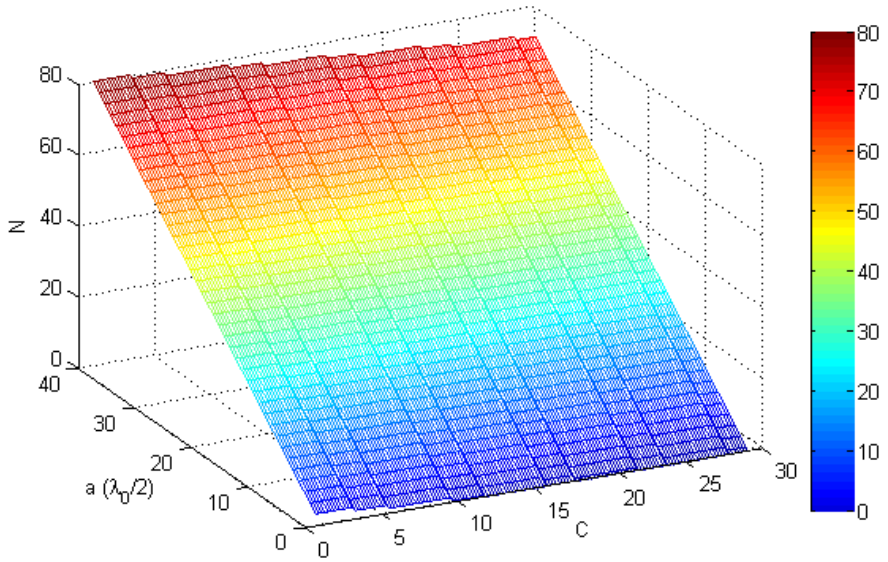

Figure II.28. Variation of N in terms of a and C

It can be clearly seen that as *C* increases the number of peaks diminishes according to a step function whereas as *a* increases the number of peak increases also linearly.

Furthermore, Figure II.29 shows the variation of *N* as a function of both the amplitude of displacement *a* and *φ* for a constant value of *C* (*C=4*). This figure shows once more the symmetry of the variations of *N* in respect to *φ=0* where this figure is a linear repetition of the effect of *φ* for *C* constant presented in Figure II.27, which is very reasonable regarding the purely linear effect of the variations of amplitude.

Finally, an interesting information will be the combined effect, for a constant amplitude of displacement, of both the coupling factor *C* and *φ*. Figure II.30 shows both the effect of *φ* presented in Figure II.27 and the step function representing the effect of *C*.

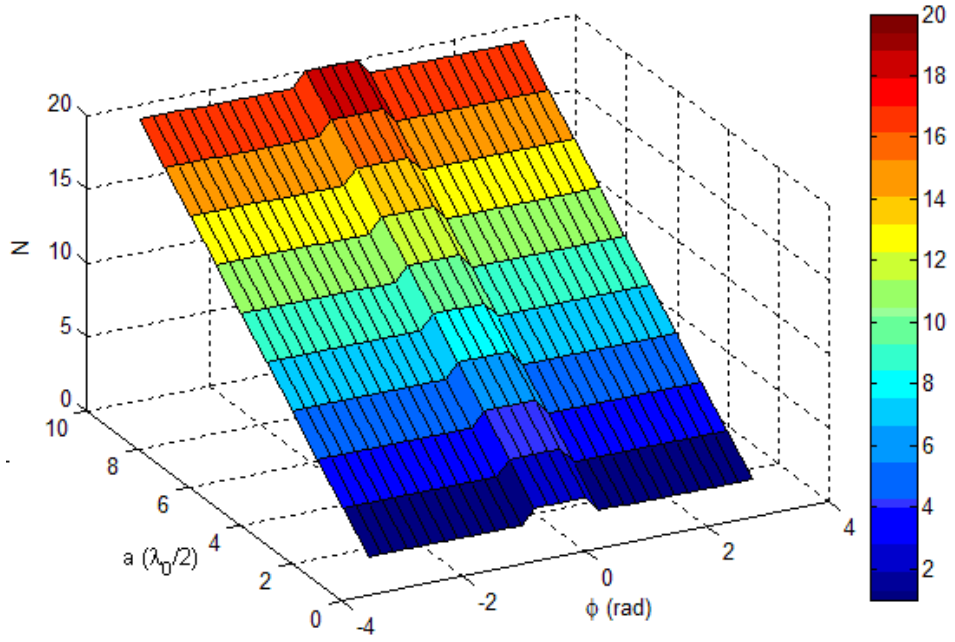

Figure II.29. N as a function of both the amplitude of displacement a and φ for a constant value of C (C=4)

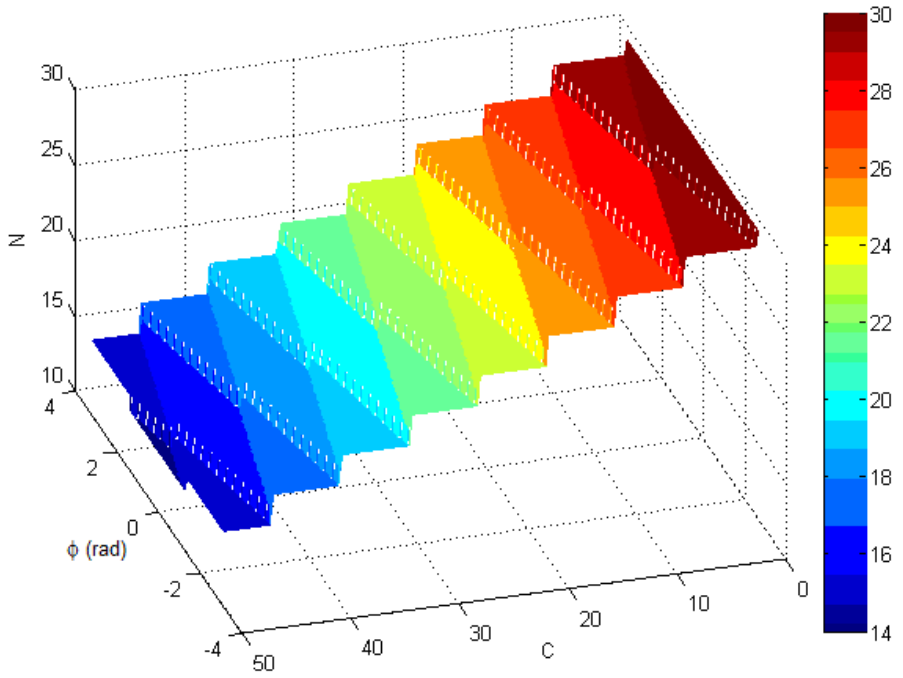

Figure II.30. Combined effect of C and φ on the number of peaks N.

II.7. Application to Displacement Measurements

As mentioned earlier, a variation of C of 2π (2.26) causes two pairs of peaks to disappear (or appear), each of them disappearing (or appearing) for even smaller variations of the coupling coefficient (as low as $C=1.32$ Table II.4). This will reduce seriously the resolution of fringe counting techniques since each peak has to represent a target displacement of $\lambda_0/2$ which is not the case anymore in most cases [69].

In industrial mechatronic applications, such as vibration measurements, keeping D_0 constant or hitting exactly the same point of the sensed surface is not realistic at all. Thereby, since both these conditions affect the coupling coefficient, fringe counting techniques are practically unusable in this type of applications. This means that the measurement error of the previously discussed sensors will be increased by $\lambda_0/2$ each time a pair of peaks disappears.

This section illustrates a method enabling to measure a displacement even when the above-mentioned mechanism of appearance/disappearance occurs, i.e. when the number of peaks of the OOP is no more proportional to the number of half-wavelength displacements.

This method is based on the fact that when peaks disappear the SM signal is following directly the displacement of the target (Figure II.31) and that the disappeared peaks will be present inside the pointed parts of the signal as shown previously in Figure II.24.

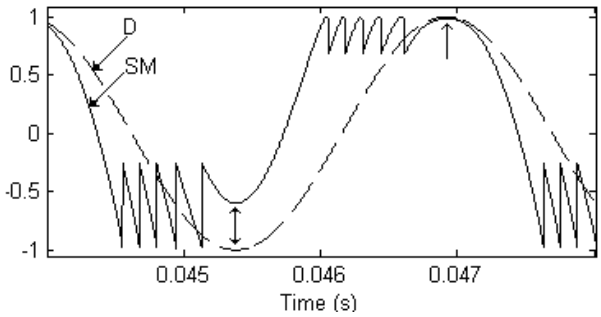

Figure II.31. Simulations showing how SM signal follows the displacement (having an amplitude of 4λ0/2) while losing peaks.

Then, all the remaining peaks will be detected by unwrapping the phase of the signal, i.e. with a threshold detection of the derivative of *arccos(P(t))* [30] or when the signal is noisy, by using a continuous wavelet transform [70]. Each detected peak corresponds to a half-wavelength displacement as in usual fringe counting methods. The difference resigns in adding this integer number of $\lambda_0/2$ displacements to the part of the signal called "zone 1" in Figure II.24 including both the excess fringe (i.e. the fraction of $\lambda_0/2$ as the amplitude of displacement has no reason to be exactly equal to an integer number of $\lambda_0/2$) and the disappeared peaks present in the pointed part of Figure II.31.

Furthermore a detailed study of the theoretically simulated effect of the changes of C on the measurement error of the described method is plotted in Figure II.32

This figure compares this error to the added error in the case of fringe counting techniques clearly showing the large difference between the two compared errors. Considering in example the case of $C=8$ the error encountered in the phase unwrapping method is approximately *92nm* whereas the additional error caused by the peak disappearance is $\lambda_0/2$ for $\varphi=\pi/2$ and λ_0 for $\varphi=0$ in the case of the fringe counting technique.

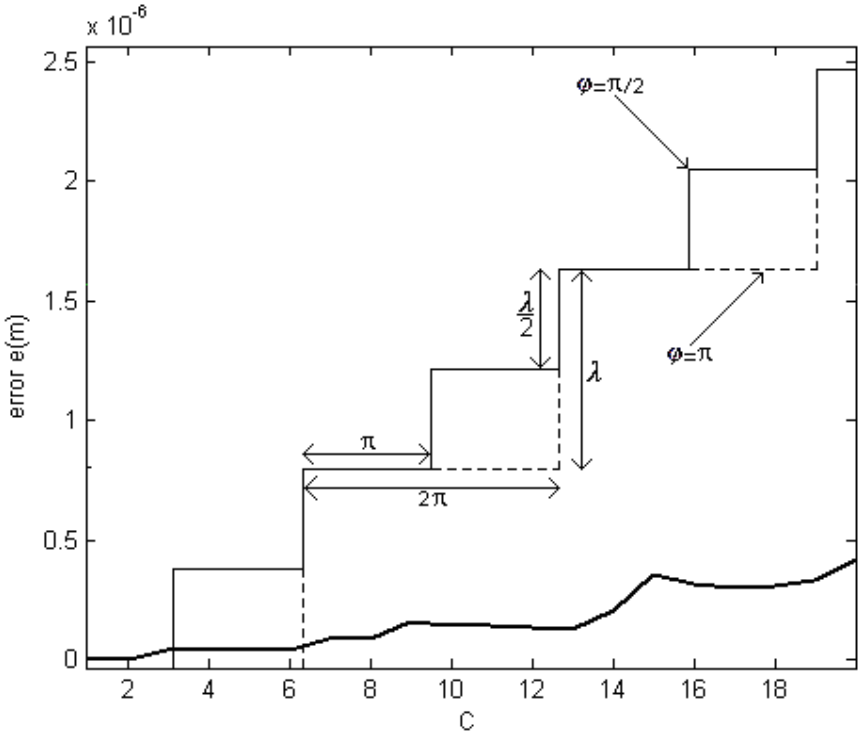

Figure II.32. Comparison between the additional error due to peak disappearance in fringe counting techniques and the simulated theoretical error of the above discussed method.

On the practical side, Figure II.33 shows two of the experimentally acquired samples. These samples correspond to acquisitions having different values of *C* but corresponding to the same displacement amplitude of *9.562 μm* as detected by a capacitive sensor with a resolution less then *2 nm*. These samples show different numbers of peaks corresponding for an increasing *C* where the number diminishes from *25* to *20*.

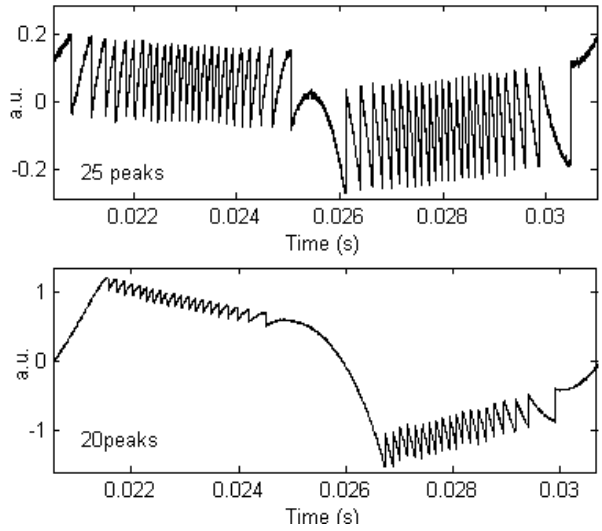

Figure II.33. Experimental samples of acquired OOP signals showing lost of peaks.

Table II.5 shows the different amplitudes as detected by the described method compared with the ones measured by the capacitive sensor for an experiment of *10* acquisitions.

C	*N*	*Amp. SM*	*Amp. Capa*	*SM/ Capa.*	*Error (%)*
28.6	20	23.087	9.557	2.4157	3.9
11.73	23	23.982	9.583	2.5025	4.1
9.82	23	23.981	9.583	2.5024	4.2
4.13	25	24.674	9.557	2.5817	2.7
26.96	20	23.4672	9.557	2.4555	2.3
23.57	20	23.6052	9.557	2.4699	1.7
25.08	21	23.5027	9.583	2.4525	2.4
3.76	24	24.8865	9.557	2.6040	3.6
4.28	24	24.8007	9.557	2.5949	6.3
7.93	24	24.3065	9.531	2.5503	1.5
		24.0292	9.562	2.5129	3.27

Table II.5. Comparison between the amplitude of vibration between the capacitive sensor and the described method

It can be seen in this table, that the average measurement error is approximately *3.27%* corresponding in this case to *0.312 μm*. On the other hand, it can be clearly seen that the number of peaks varies from *25* down to *20* meaning that the resolution in the case of fringe counting techniques would has been degraded in *30%* of the signals corresponding to signals with 24 peaks by $\lambda_0/2$ (i.e. *0.3925 μm*), in *20%* of the signals corresponding to signals with 23 peaks by $2\lambda_0/2$ (i.e. *0.785 μm*), in *10%* of the signals corresponding to signals with 21 peaks by $4\lambda_0/2$ (i.e. *1.57 μm*) and in *30%* corresponding to signals with 20 peaks by $5\lambda_0/2$ (i.e. *3.925 μm*).

Finally only in *10%* of the acquisitions the number of peaks was directly proportional to the displacement showing that the fringe counting technique can be no more used for displacement measurements leading to an average error of approximately *1.61 μm*.

II.8. Conclusion

Many idiosyncrasies in experimental moderate self-mixing signals for displacement measurements were observed, studied and explained in this chapter.

First, the problem of peak disappearance was brought up through experiments, simulations and a complete interpretation as it was shown that an increase of C by 2π would cause two pairs of peaks to disappear, all of this with errors less than *1.5%*. This will have major effect on self-mixing displacement sensors as the fringe counting methods will not be very accurate anymore for moderate or strong feedback regimes.

Then the experimental variation of this coupling factor was depicted showing the influences of the distance to the target, the total external cavity losses and the roughness of the target surface showing that keeping C constant in vibration measurements is not realistic at all.

Afterwards, it was shown that the phase unwrapping method, described above, permits to reduce the displacement measurements errors to *3.27%* approximately when a peak of the optical output power does not correspond anymore to a half-wavelength of displacement.

Moreover, the strong feedback, defined by a complete disappearance of the sawtoothlike variations of the optical output power, was proven to be not only due to the coherence collapse of the laser (i.e. when C is high) but also to depend on the displacement amplitude of the target, and thereby maybe encountered for low values of C in the case of small amplitude displacements (Figure II.30). As a consequence, as it will be shown in the next chapter, a laser under strong feedback (after the complete disappearance of its peaks) would also be able to measure the relative displacement of a target even without the need of any signal processing algorithm if this regime can be maintained long enough [71].

Chapter III. Strong Feedback Regime

III.1. Introduction

In the previous chapter, it was shown that the number of pairs of peaks in a self-mixing signal will diminish by two every time the coupling factor C is increased by 2π. Figure II.8 illustrated this peak disappearance effect and especially the last part of this figure shows a peak free signal following exactly the displacement. This corresponds to a laser in the strong feedback regime where no interferometric discontinuities remain. In this case, the laser accomplishes a sort of an injection detection of the time of flight between the laser and the target.

Generally, sensing applications using the self-mixing effect were developed in the weak [72] and moderate [59] feedback regimes. The strong feedback has also been investigated for angle measurement [73], demonstrating for the first time that a laser can even be used for sensing purposes in this regime reputed for its instability. This regime has the advantage of giving a real time image of the displacement having exactly the same frequency and an amplitude proportional to the one of the displacement itself without the need of any signal processing. Displacement self-mixing sensors operating in this regime are developed for the first time. Thus they revealed to be very attractive for a wide range of applications such as the real time modal analysis or real time relative displacement measurement [71].

The first part of this chapter will present the so called strong feedback regime studying the peak free signals and simplifying the behavioral model in the particular case of this regime in order to demonstrate the statistical aspect of this type of signals analytically and through different simulations and experiments.

The second part, will introduce a conception and characterization of a relative displacement sensor in terms of linearity and total harmonic distortion through different simulations and different experiments.

III.2. The Self-Mixing Signal in The Case of Strong Feedback

III.2.1. Variable Changes and The Rewriting of The Self-Mixing Equations

As stated before, the emission wavelength's fluctuations can be found by solving the phase equation (2.5) [57]-[59]-[74]: this can be rewritten as follows doing a simple change of variables:

$$\begin{aligned} X_0(t) &= x_0(t) + \arctan(\alpha) \\ X_F(t) &= x_F(t) + \arctan(\alpha) \end{aligned} \tag{3.1}$$

$$X_0(t) = X_F(t) + C\sin\left(X_F(t)\right) \quad \forall t > 0 \tag{3.2}$$

$x_F(t)$ and $x_0(t)$ being defined respectively in equations (2.3) and (2.4). C was defined in equation (2.11) showing that the only parameter depending on the target's surface is ζ.

Moreover the variations of the OOP due to the feedback can be now rewritten as follows:

$$P_F(t) = P_0\left(1 + m\cos\left(X_F(t) - \tan^{-1}(\alpha)\right)\right) = P' + \tilde{P}(t) \tag{3.3}$$

Where P' and $\tilde{P}(t)$ represent respectively the constant and time variant parts of the emitted power.

$$\tilde{P}(t) = mP_0\cos\left(X_F(t) - \arctan(\alpha)\right) \tag{3.4}$$

III.2.2. Strong Feedback Signals (Peak Free Signals)

It was shown before, that increasing the feedback level by 2π will make two pairs of peaks disappear (equation (2.26)). It could be imagined then, that at a certain feedback level, sufficiently high, the self-mixing signal will not have any peaks left.

In fact Figure III.1 shows simulations of different SM signals generated by the same displacement ($2\lambda_0/2$) where as expected for $C=1$ the signal has 4 peaks where for $C=7$ it has only 2 peaks and for high values of C (i.e. $C=17$) it has no

peaks left. The laser diode performs then a sort of injection detection process sensitive to the variations of the round trip power attenuation in the external cavity for the strong feedback regime.

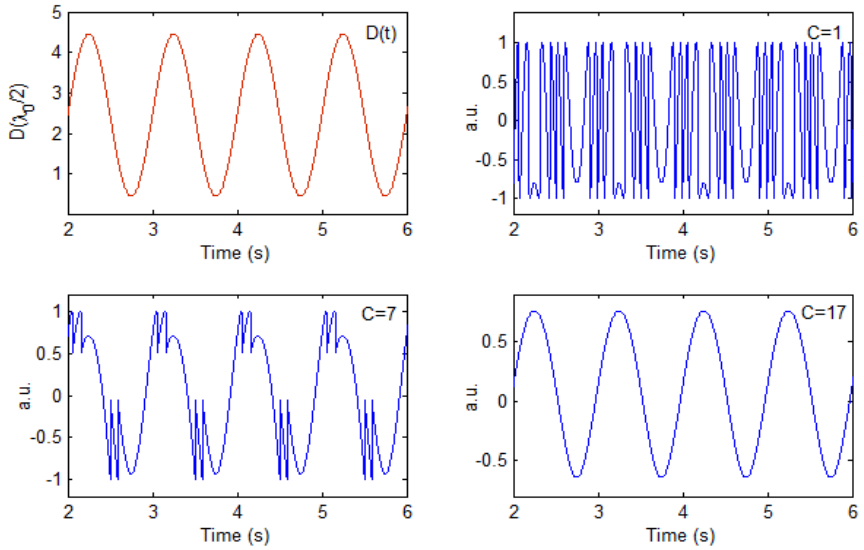

Figure III.1 Simulations of the SM signal generated by D(t) for C=1 (4 peaks), C=7 (2 peaks) and C=17 (0 peaks)

Thereby, the OOP will have the same shape and frequency as the displacement with an amplitude proportional to its amplitude; this is illustrated in Figure III.2 that shows the SM signal following different shapes of the generating signal and Figure III.3 that shows simulations for different amplitudes of displacement proving that the SM signal's amplitude is proportional to the displacement's amplitude.

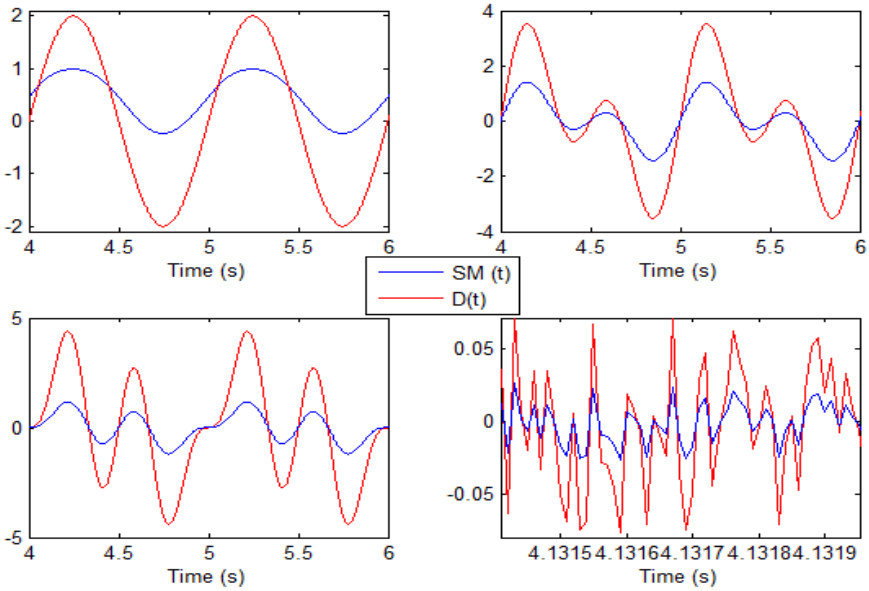

Figure III.2 Simulations of strong feedback SM signal generated by different shapes of displacements.

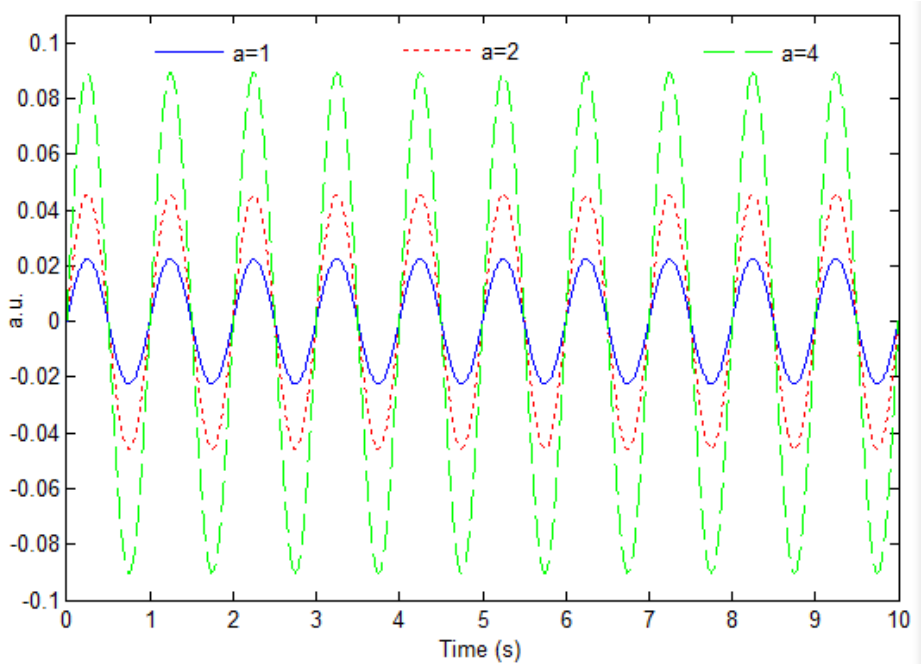

Figure III.3 Simulations of strong feedback SM signal generated by displacements with different amplitudes (a).

Actually, it was shown that this sinusoidal signal proportional to the target displacement can be obtained for low values of *C* if the displacement has a sufficiently small amplitude (*a*). In fact Figure III.4 shows the minimum feedback needed in order to have a peak free OOP corresponding to different amplitudes of variation of *D)t)* [71].

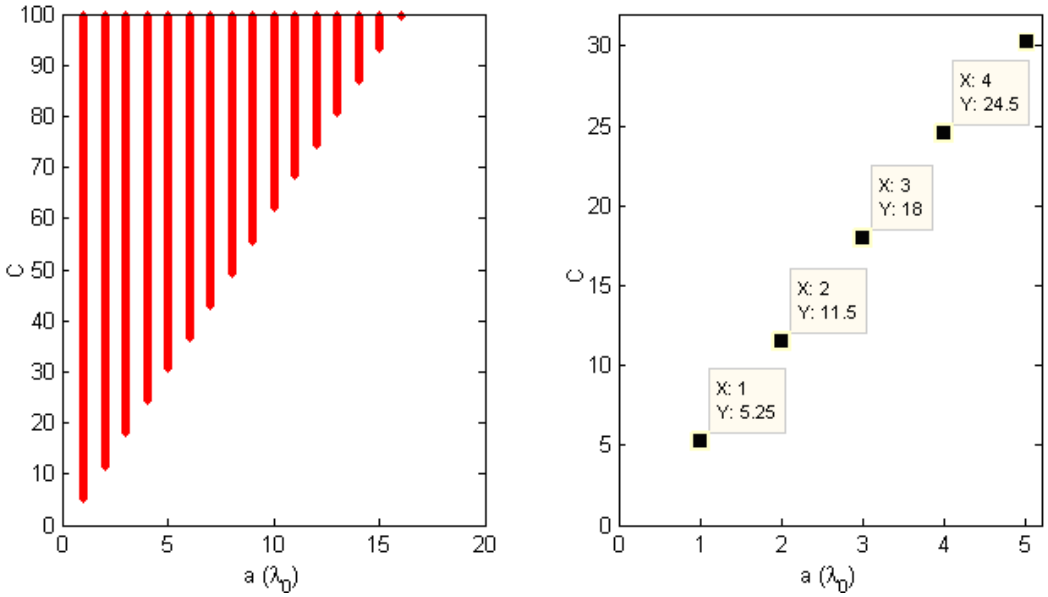

Figure III.4 Feedback corresponding to peak free OOP signal for different amplitudes a.

This figure shows the values of *C* giving a peak free signal for each amplitude of displacement (*a*). As an example for a displacement of amplitude around λ_0 (i.e.

0.785µm in our case) a feedback corresponding to a *C* of *5.25* is enough to have a peak free OOP or even for an amplitude of displacement of $3\lambda_0$ (i.e. *3.55µm* in our case) a feedback corresponding to a *C* of *18* is needed. It is to be noted that these values of *C* are a function of the distance $D(t=0)=D_0$ through φ and may vary according to its changes where Figure III.4 was plotted for $\varphi=\pi/4$.

III.2.3. Theoretical Behavior Model of a Laser under Strong Feedback

Now, considering small fluctuations of $x_F(t)$ around $k\pi$ and high values of *C* corresponding to the strong feedback regime (Figure II.20), the equation (3.2) can be approximated by a first order Taylor development as follows:

$$X_0(t) \approx X_F(t) + C\left(X_F(t) - k\pi\right) \Rightarrow X_F \approx \frac{X_0 + Ck\pi}{1+C} \tag{3.5}$$

Then, substituting X_F by its expression into equation (3.4), $\tilde{P}(t)$ can be expressed as follows:

$$\begin{aligned} \tilde{P}(t) &= -mP_0 \frac{X_0(t)}{1+C} \sin\left(\frac{Ck\pi}{1+C} - \tan^{-1}(\alpha)\right) \\ &\approx mP_0 \frac{X_0(t)}{1+C} \sin\left(\tan^{-1}(\alpha)\right) \end{aligned} \tag{3.6}$$

Substituting now $X_0(t)$ by its expression in equation (3.6), $\tilde{P}(t)$ can be written as follows:

$$\tilde{P}(t) = mP_0 \left[\frac{4\pi \sin\left(\tan^{-1}(\alpha)\right)}{\lambda_0(1+C)} D(t) - \frac{\sin\left(\tan^{-1}(\alpha)\right)}{1+C} \tan^{-1}(\alpha) \right] = \tilde{\tilde{P}}(t) + P'' \tag{3.7}$$

Equation (3.7) points out the linear relationship between the displacement $D(t)$ and the OOP fluctuations $\tilde{\tilde{P}}(t)$ in the case of strong feedback and small amplitude regime. Considering equation (1.23), *m* can be rewritten as follows [51]:

$$m = m_0 \zeta \varepsilon \tag{3.8}$$

Where m_0 is the proportionality coefficient of m to ζ and ε. Then using the expression of C from equation (2.11) it is then possible to write $\tilde{\tilde{P}}(t)$ more explicitly

$$\tilde{\tilde{P}}(t) = \frac{4\pi m P_0 D(t)\sin\left(\tan^{-1}(\alpha)\right)}{C\lambda_0} = \frac{4\pi m_0 P_0 D(t)\sin\left(\tan^{-1}(\alpha)\right)}{\lambda_0 \frac{\tau_D}{\tau_l}\sqrt{1+\alpha^2}} = D(t)/M_2 \tag{3.9}$$

M_2 is the conversion factor permitting the transformation of the OOP variations detected into a displacement of the target when the laser is under strong feedback.

It can be noticed that theoretically this parameter depends on the nature of the laser diode (a, τ_l and m_0) and on the initial conditions (P_0, λ_0, τ_D and $x_F(0)$) but does not depend on the surface reflectivity (x_{ext}) nor the coupling efficiency γ.

A self-mixing signal corresponding to a rather high optical feedback ($C=8$) relatively to the amplitude of vibration ($\lambda_0/2$) is simulated using the behavioral model [57] and equation (3.9) in Figure III.5.

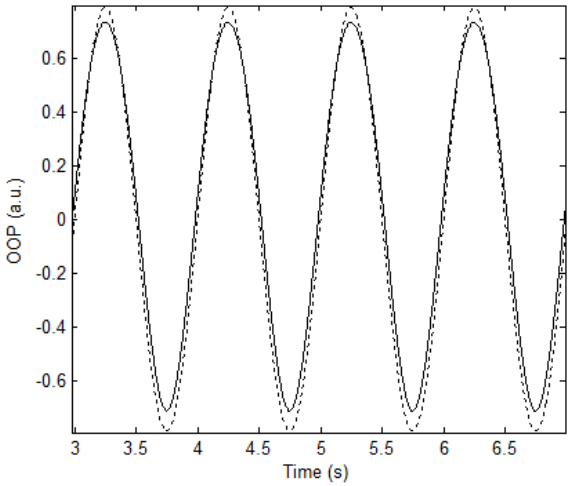

Figure III.5 Simulations of self-mixing signals corresponding to a sinusoidal displacement of an amplitude of $\lambda_0/2$ and a $C=8$ using equation 8 (dotted line) and the behavioral model developed in [57] (plain line).

This figure verifies that the previous approximations made in order to obtain equation (3.9) are applicable for relatively high values of C and small displacement's amplitudes.

Moreover, different simulations of calculations of the conversion factor M_2 by varying the coupling coefficient were accomplished and traced in blue in the following figure. On the other hand, looking back on equation (3.9) it can be seen that it is has hyperbolic variation in respect to C. This equation was reported in the following figure after normalization to mP_0. It can be seen that when C increases the red curve rejoins the blue ones asymptotically. However, it is to be noted that the values of C needed to be sufficiently high ($C=10$) in order to validate the approximations made in equation (3.9) whereas physically lower values of C are sufficient (Figure III.4).

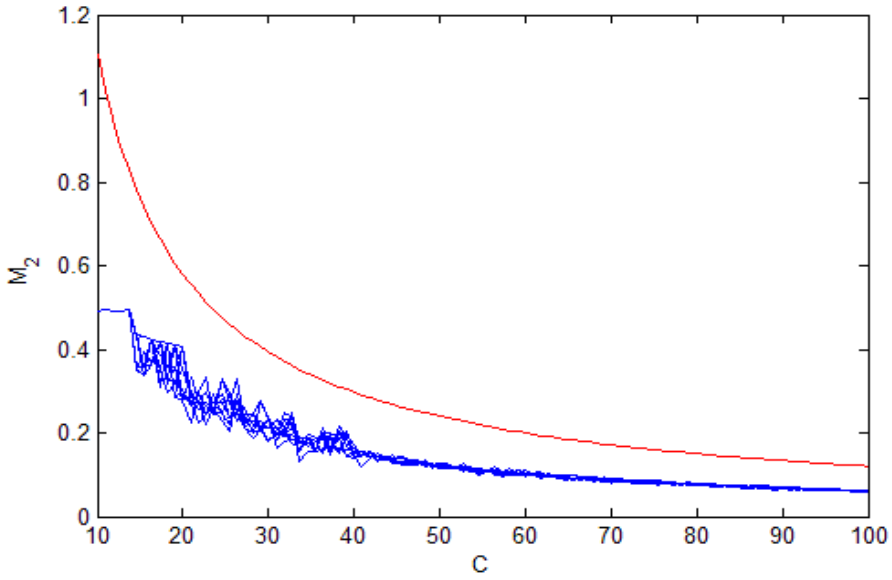

Figure III.6 M_2 as a function of C obtained by the behavioral model in blue and by equation (3.9) in red

III.2.4. Statistical Aspect of The Variations of The OOP

Different simulations using the model developed in [57] showed that the linear relationship between $\tilde{\tilde{P}}(t)$ and $D(t)$ had a statistical aspect when considering the amplitude of the OOP variations for the same amplitude of displacement (Figure III.7). On the other hand, this figure showed that the frequency of the OOP followed exactly the displacement frequency.

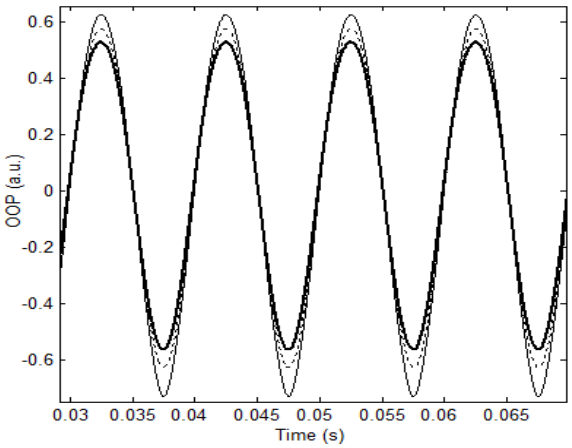

Figure III.7 Repetitions of the simulation of the same sinusoidal displacement showing the statistical aspect of the OOP variations amplitude.

In order to illustrate explicitly this statistical aspect, the equation (3.4) is considered again and the expression of $\tilde{P}(t)$ is rewritten substituting X_F by its expression in equation (3.5).

$$\tilde{P}(t) = mP_0 \cos\left(\frac{X_0(t)+Ck\pi}{1+C} - \tan^{-1}(\alpha)\right) \tag{3.10}$$

This expression can be approximated using a Taylor first order development around $X_0(0)=X_0(t=0)$.

$$\begin{aligned}\tilde{P}(t) &= mP_0\left[\cos\left(\frac{X_0(0)+Ck_0\pi}{1+C} - \tan^{-1}(\alpha)\right) - \frac{(X_0(t)-X_0(0))}{1+C}\sin\left(\frac{X_0(0)+Ck_0\pi}{1+C} - \tan^{-1}(\alpha)\right)\right] \\ &= \tilde{\tilde{P}}'(t) + P'''\end{aligned} \tag{3.11}$$

With k_0 the number of the curve segment of the function $F(t)$ chosen at $t=0$ (Figure III.8).

Considering back now the expression of $\tilde{\tilde{P}}'(t)$, it may be rewritten as a function of the displacement when both $X_0(t)$ ((3.1)) and $x_0(t)$ ((2.4)) are substituted by their expressions:

$$\tilde{\tilde{P}}''(t) = \frac{\tilde{\tilde{P}}'(t)}{mP_0} = \frac{-4\pi\tilde{D}(t)}{\lambda_0(1+C)}\sin\left(\begin{array}{c}\frac{Ck_0\pi}{(1+C)} + \frac{4\pi D_0}{\lambda_0(1+C)} \\ -\frac{(2+C)\tan^{-1}(\alpha)}{(1+C)}\end{array}\right) \tag{3.12}$$

Where $\tilde{D}(t)$ is the instantaneous displacement reported to D_0 i.e. $\tilde{D}(t) = D(t) - D_0$; D_0 being the initial laser to target distance at $t=0$. When considering that the displacements are sinusoidal and that the target is not moving at $t=0$, then D_0 corresponds also to the mean value of distance around which the target is moving.

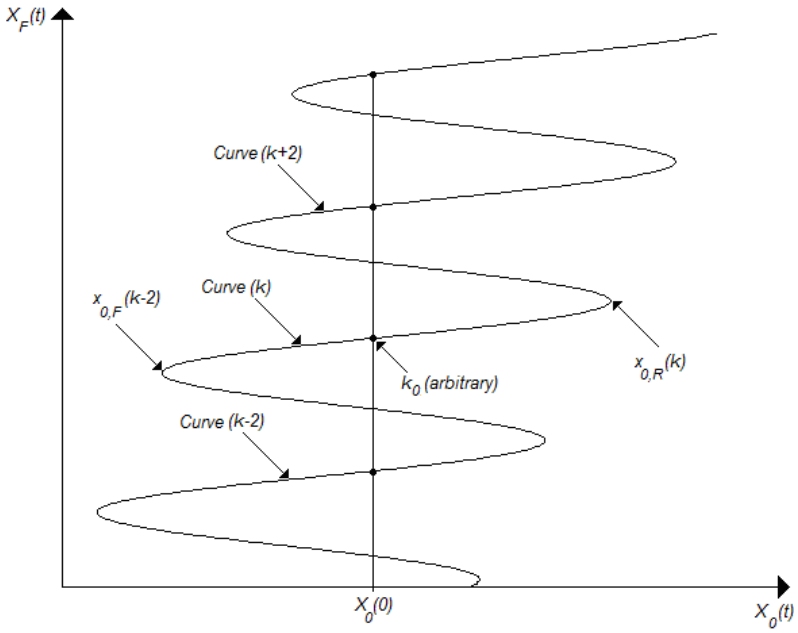

Figure III.8 $X_F(t)$ as a function of $X_0(t)$ (F function).

This expression gives another expression of the conversion factor $M_2 = \tilde{D}(t) / \tilde{\tilde{P}}''(t)$ between the OOP variations and the displacement as follows:

$$M_2 = \frac{\lambda_0(1+C)}{-4\pi \sin\left(\frac{Ck_0\pi}{(1+C)} + \frac{4\pi D(0)}{\lambda_0(1+C)} - \frac{(2+C)\tan^{-1}(\alpha)}{(1+C)}\right)} \qquad (3.13)$$

This factor has a double statistical aspect caused by both D_0 and k_0. In fact, when the laser is turned on the target is at an unknown statistical distance D_0 which sets the first statistical variable. Once D_0 is set (i.e. $X_0(0)$), the laser will lock on one of the different segments fixing thereby statistically k_0 (Figure III.8).

Moreover, in the case of strong feedback with high values of C the traditional shape of the function F is replaced by a group of quasi-parallel quasi-horizontal lines as represented in Figure III.9.

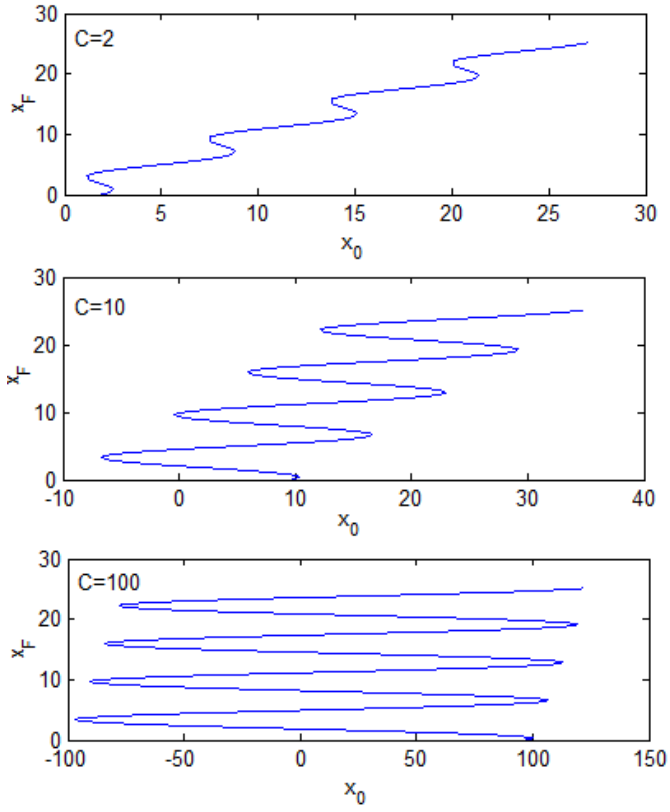

Figure III.9 F function for different values of C

Since the displacement has a small amplitude, it is possible to assume that after triggering on one of the different triggers (i.e. one of the parallel lines) the laser will stay on this trigger as long it is not turned off. In fact, once the laser is powered, $x_0(t=0)$ will be fixed through D_0. Then the laser will fix a triger k_0 (and keep it), and thereby M_2, chosen initially in an arbitrary manner, will be kept after that constant.

III.2.5. Statistical Study of M_2

It was stated before that k_0 is chosen arbitrary when the laser is powered. However, k_0 will be chosen from a finite number of triggers to which $X_0(0)$ belongs (Figure III.8). Calculating the width of a trigger [57], it is given by $x_{0,R}(k)-x_{0,F}(k-2)$ which are defined by equations (2.13) [57]:

$$\begin{aligned} x_{0,R}(k) &= k\pi - \tan^{-1}(\alpha) + \gamma \\ x_{0,F}(k) &= (k+2)\pi - \tan^{-1}(\alpha) - \gamma \end{aligned} \tag{3.14}$$

Where $\gamma = \cos^{-1}(-1/C) + C\sin\left(\cos^{-1}(-1/C)\right)$, leading to a segment width of 2γ.

In order to calculate the number of the possibilities N' that may be chosen by k_0 the following condition must be satisfied:

$$\begin{aligned} & k_1\pi - \tan^{-1}(\alpha) - \gamma \le x_0(0) \le k_2\pi - \tan^{-1}(\alpha) + \gamma \\ & \Rightarrow k_1\pi - \gamma \le X_0(0) \le k_2\pi + \gamma \end{aligned} \tag{3.15}$$

k_1 and k_2 being the first and the last values of k corresponding to peak free signal. γ can be approximated using an asymptotic development to the first order as $\gamma \approx C + \pi/2$. This approximation allows us to deduce both k_1 and k_2 and thereby N' as follows:

$$\begin{aligned} k_1 &= 2floor\left(\frac{X_0(0) - C - \pi/2}{2\pi}\right) + 2 \\ k_2 &= 2floor\left(\frac{X_0(0) + C + \pi/2}{2\pi}\right) \end{aligned} \tag{3.16}$$

$$N' = \frac{k_2 - k_1}{2} \tag{3.17}$$

Where *floor(x)* is a function that gives the lower integer part of a decimal.

Based on this statistical theory and on equation (3.13) a model was conceived in order to calculate the M_2 factor. The statistical variable D_0 was approximated by a Gaussian variable whereas k_0 was approximated by a uniformly distributed variable limited between k_1 and k_2. The validity of this choice will be justified farther in this study.

Figure III.10 shows an histogram obtained by this model for a $C=9$. It shows the combined effect of both Gaussian and uniformly distributed variables where a certain repetition of a Gaussian distribution may be visualized.

The effect of both random variables is more or less accentuated by the values of C. It can be seen that if C has a small value the effect of D_0 is more important where the histogram shown in Figure III.11 simulated for $C=5$ shows a quasi-Gaussian distribution.

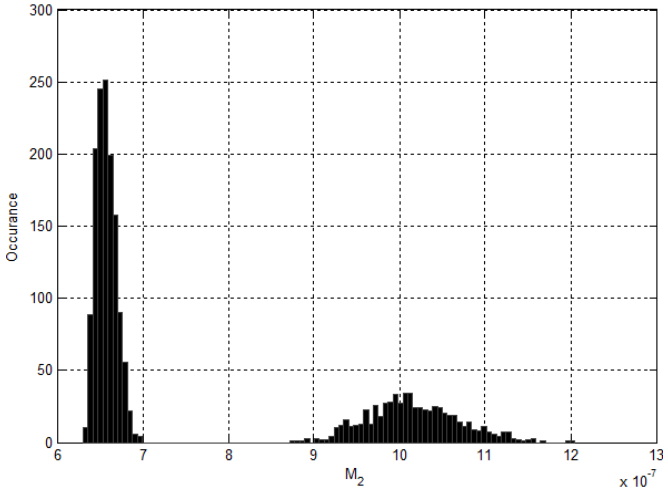

Figure III.10 Histogram obtained by simulation for a C=9 using the previous model.

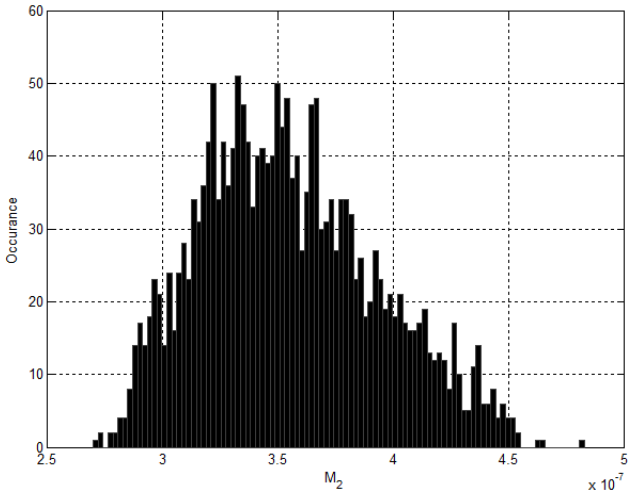

Figure III.11 Histogram obtained for C=5

When the value of C increases, simulation histograms showed a combined effect of both random variables (Figure III.10). If very large values of C are considered the effect of D_0 is attenuated and the effect of k_0 overtakes (3.13) where Figure III.12 shows an histogram simulated for a $C=300$.

Figure III.13 shows a typical histogram for a $1/sin(u)$ random variable where u is a uniform random variable. The resemblance between Figure III.12 and Figure III.13 can be understood looking back at equation (3.13) considered for high values of C.

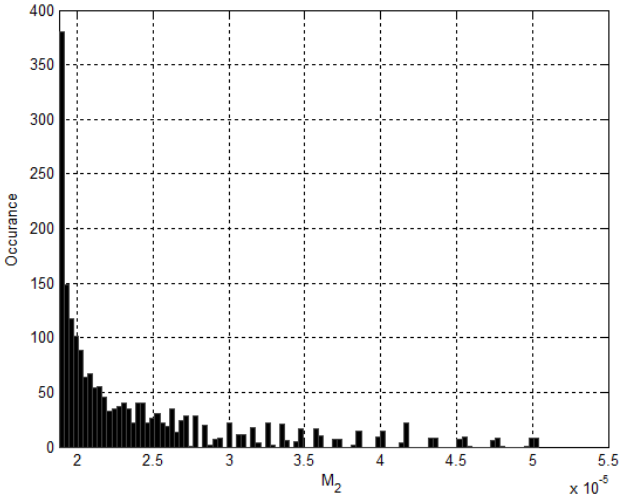

Figure III.12 Histogram obtained by simulation for a C=300 using the previous model.

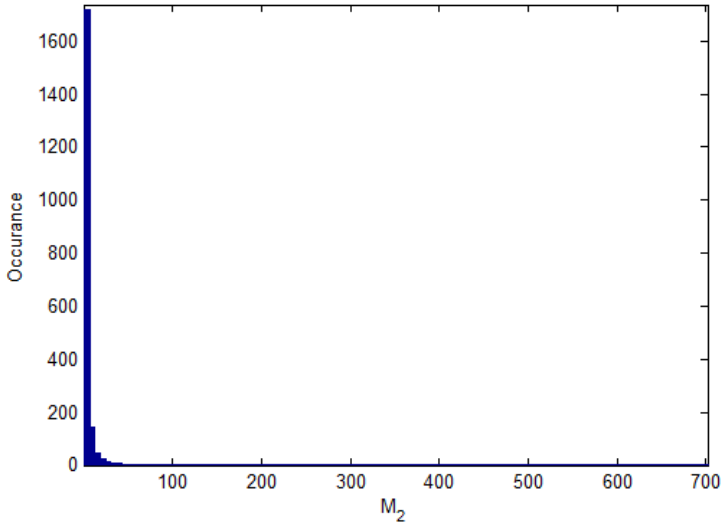

Figure III.13 Histogram of 1/sin(u) where u is a uniform random variable

The effect of the wavelength and the distance on the histograms of M_2 can be obtained through simulations. First, it can be seen, by comparing Figure III.14 and Figure III.15 that the wavelength has no major effect on the shape of the probability distribution nor on the values of M_2 obtained.

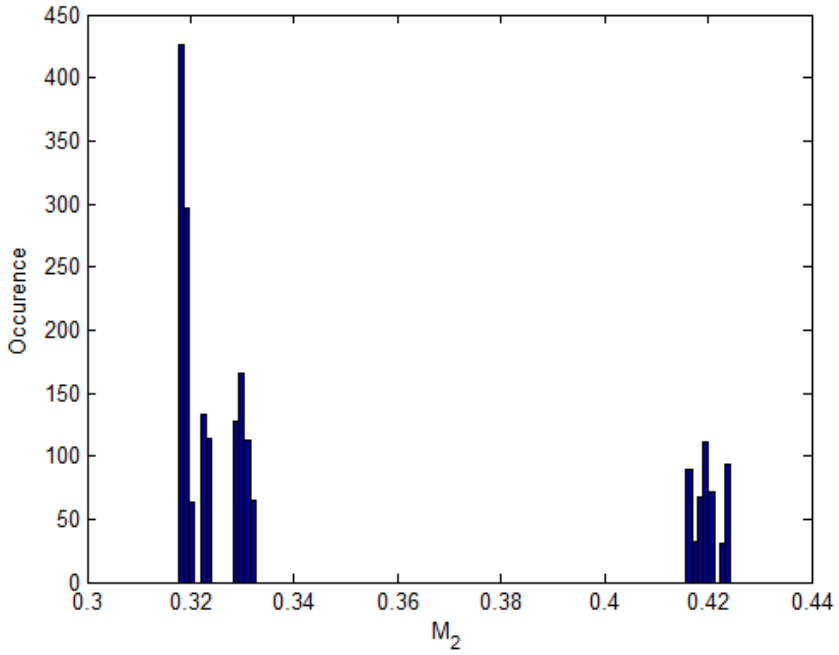

Figure III.14 Histogram for a M_2 with λ_0=785nm and D_0=1m

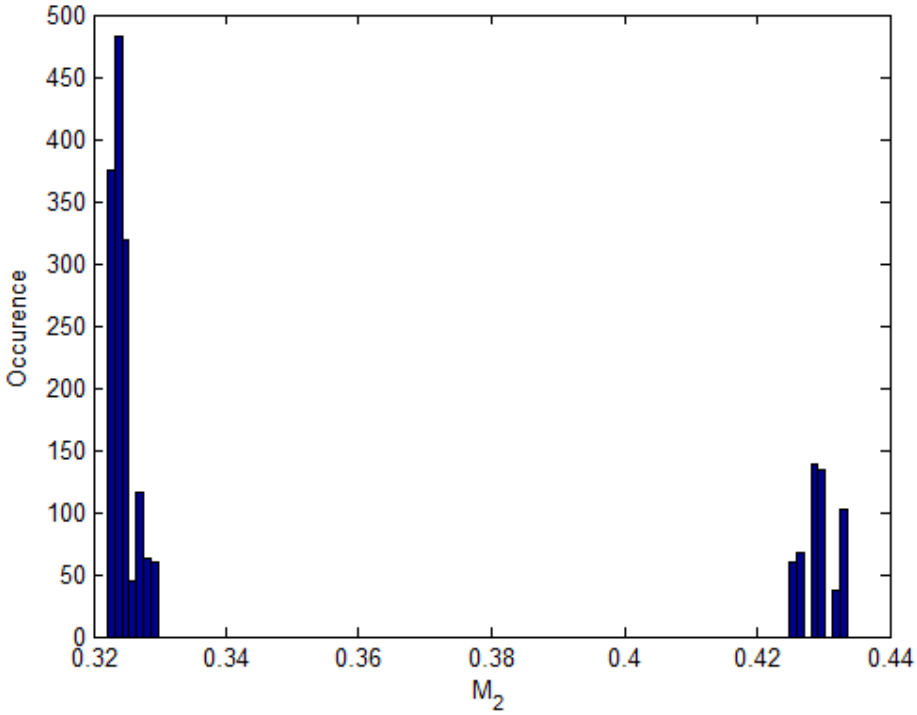

Figure III.15 Histogram for a M_2 with λ_0=1300nm and D_0=1cm

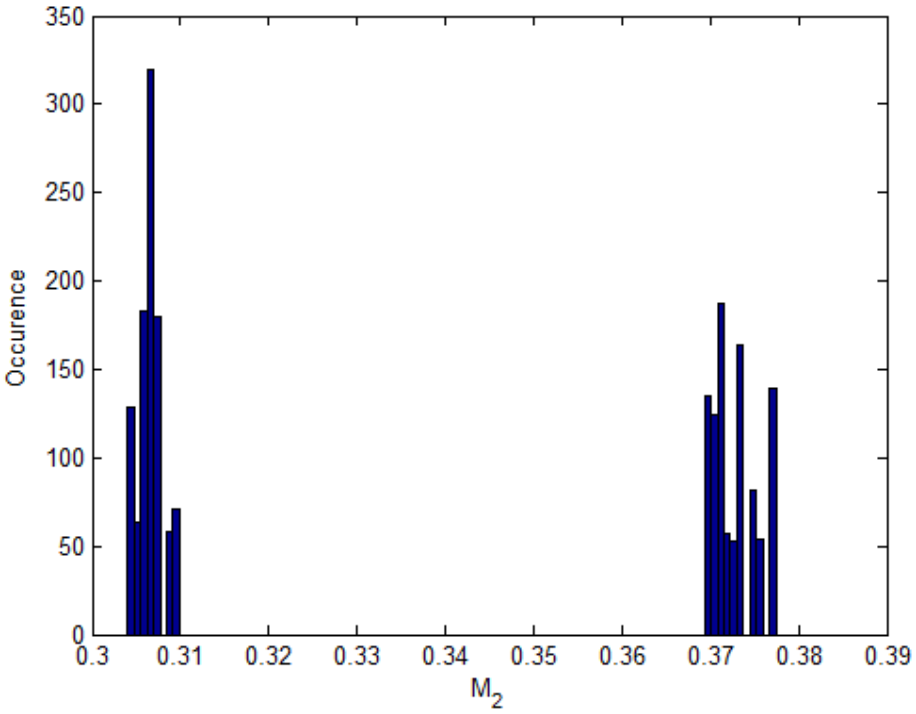

Figure III.16 Histogram for a M_2 with λ_0=785nm and D_0=40cm

On the other hand, Figure III.14 and Figure III.16 shows the effect of the distance, relevant in terms of values of M_2 encountered which were significantly modified. It is however of less importance in terms of shape of the probability distribution which is essentially modified by the values of C emphasizing the dominance of k_0 or $x_0(0)$ as stated earlier.

It is to be noted that this statistical aspect remains in moderate or weak feedback. In fact, Figure III.17 shows a simulation of the F function for the same values of $C=5$ and $a=3$ but k_0 and D_0 were simulated, as previously, by a Gaussian variable and a uniformly distributed variable respectively.

This figure shows that in this case the number of discontinuities is the same in both cases. The only difference is that right and left parts of these simulations were not the same. However, the addition of both these parts is approximately the same *((189.6-187.9)+(225.5-222.4)=1.7+3.1=4.8s)* for the first simulation and *((38.82-35.76)+(73-71.66)=3.06+1.34=4.4s)* for the second one.

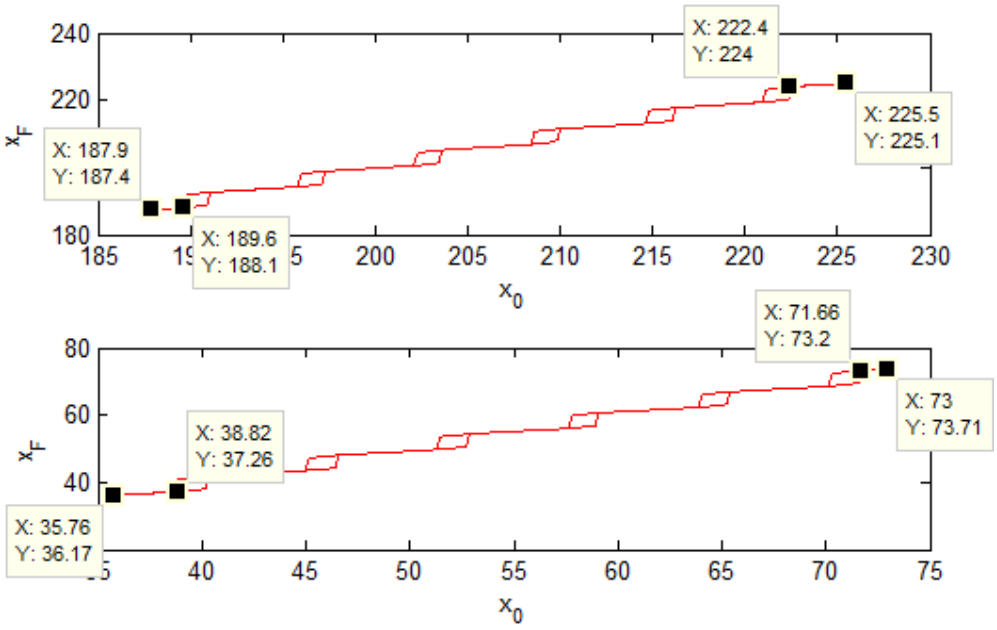

Figure III.17 F function for statistically varying k_0 and D_0. X in this figure represents the value of x_0 and Y the value of x_F.

Investigating this issue further, the OOP corresponding to these simulations was plotted in the Figure III.18 and the time occupied by the humps (pointed areas) was calculated (*(4.854-4.658)=0.196s* and *(5.362-5.156)=0.206s* for the humps of the first simulation, *(4.833-4.682)=0.151s* and *(5.343-5.18)=0.163s* for the second simulation. Looking at the respective differences (*0.196-0.151=0.045s* and *0.206-0.163=0.043s*) it can be seen that it is the same in both cases meaning that what diminishes in one hump is found in the other if D_0 and k_0 are varying statistically. Moreover the amplitude of this hump is approximately the same in both cases *(0.9085-0.4796)+(0.4796+0.9978)=0.4289+1.4774=1.9063* for the first simulation and *(0.907-0.03863)+(0.03863+0.9997)=1.9067* in the case of the second simulation.

Looking back on how the displacement is reconstructed by the phase unwrapping method (II.3) it can be seen that this statistical effect will not have an influence on the reconstructed displacement if no peaks were lost. The reconstructed displacement corresponding to the previous simulations is plotted in Figure III.19. This figure shows the displacements corresponding to the previous simulations reconstructed by the phase unwrapping method developed in [59]. It can be seen that both displacements are similar where both overlaps one over the other.

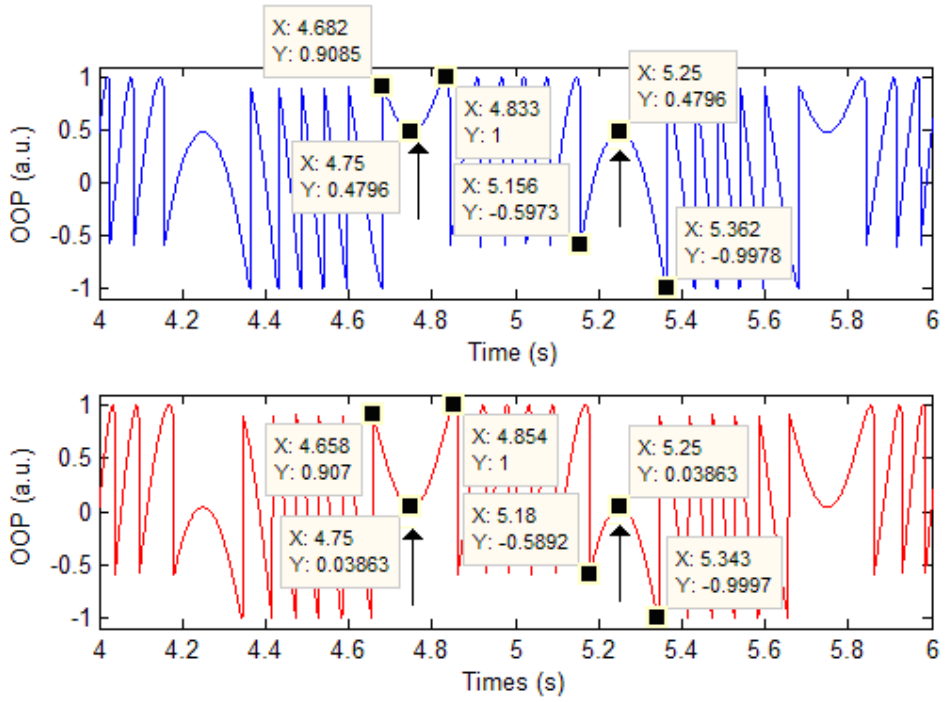

Figure III.18 OOP for statistically varying k_0 and D_0. X in this figure represents the time and Y the amplitude of the OOP.

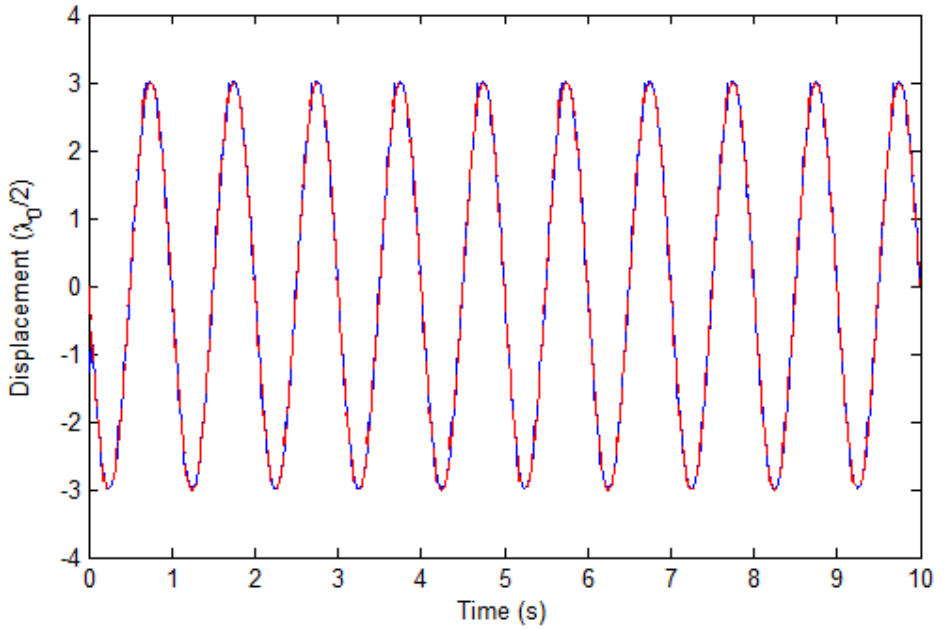

Figure III.19 Reconstructed displacements for statistically varying k_0 and D_0

It is to be noted that variations of D_0 (i.e. φ) may induce the disappearance of only one pair of peaks (II.6.3) but this will not affect seriously the resolution of the phase unwrapping method where it was shown previously (II.7) that the relative error will be around *3.27%* in this case (Figure II.32).

III.3. Experimental Statistical Study

Different experiments were made in order to understand better the variations of M_2. The first experiment, shown in Figure III.20, consisted of a rotating shutter placed between the laser diode and the PZT (separated by approximately *100cm*) cutting the beam completely because of its dark rough surface resetting thereby both statistical variables. 2000 measurements were achieved with the SM sensor and validated using a capacitive sensor installed inside the PZT. They were acquired using a 16 bit acquisition card during an eleven hours experiment. The real difficulty in this experiment was to find the convenient rotation speed of the shutter so the signal processing unit has the time to accomplish the acquisition.

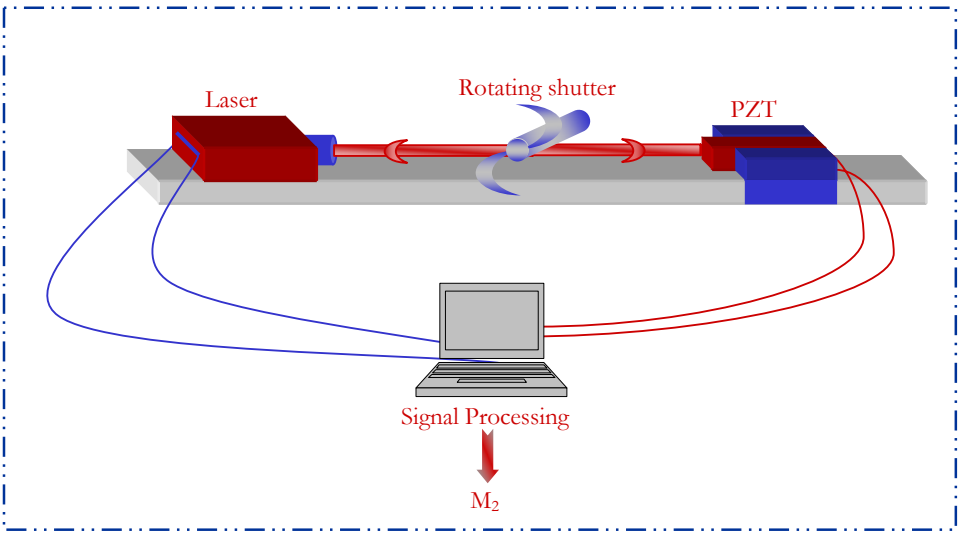

Figure III.20 Experimental setup

Figure III.21 shows the histogram of the experimentally measured values of M_2. This figure shows similarities with Figure III.10 in terms of statistical distribution (i.e. the mixed effect of both k_0 and D_0) and especially the occurrence frequencies. On the other hand, the values of M_2 encountered in this figure were modified because of the sensibility of the control photodiode and the gain of the electronic circuit.

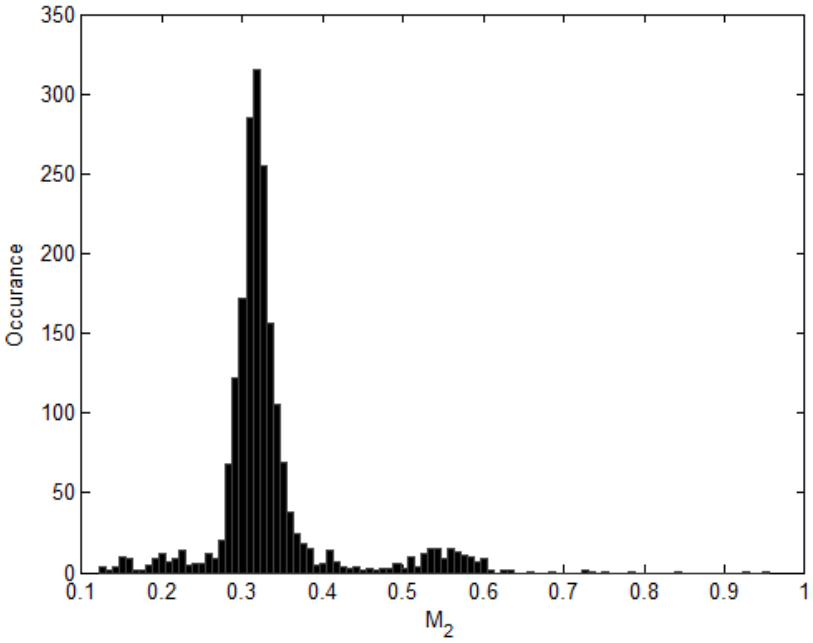

Figure III.21 Experimental histogram obtained throughout 2000 measurements of M2.

This experiment was repeated in Figure III.22, with this time 2500 acquisitions lasting for 15 hours approximately and the result was similar to the one obtained in Figure III.21 with the mixed effect of the Gaussian D_0 and the normally distributed k_0.

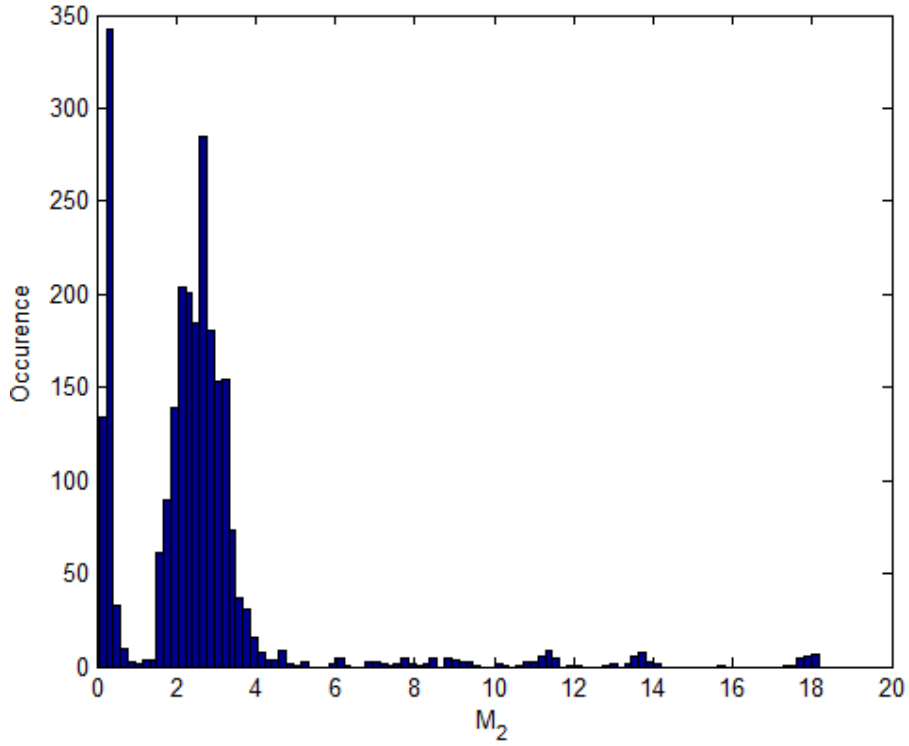

Figure III.22 Experimental histogram obtained throughout 2500 measurements of M2.

III.4. Feasibility of The Sensor under Strong Feedback

It was shown previously through simulations that the laser, under strong feedback, will accomplish a sort of injection detection following exactly the displacement in terms of amplitude and frequency. This will also be shown through different experiments using the experimental setup of Figure II.12. Figure III.23 shows the FFT of the different SM signals generated by displacements having different frequencies of *330*, *500*, *800* and *1000 Hz*. This figure proves experimentally that the SM signal follows the displacement at exactly the same frequency where the counter-measurement was made by a high resolution capacitive sensor mounted inside the PZT itself.

Moreover, Figure III.24 shows the response of the laser to different excitation signals like sinusoidal, triangular and square. Both time and frequency domains are verified, and both showed very high correspondence with the counter-measurement accomplished this time by a fibered sensor by Philtec.

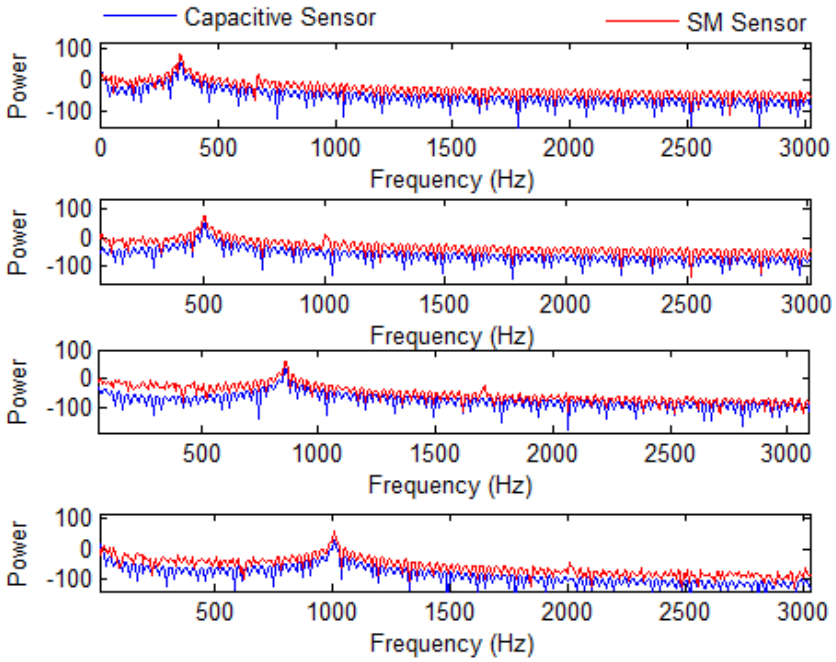

Figure III.23 FFT of the displacement given by both the SM sensor (grey) and the capacitive sensor (black) for different excitation frequencies.

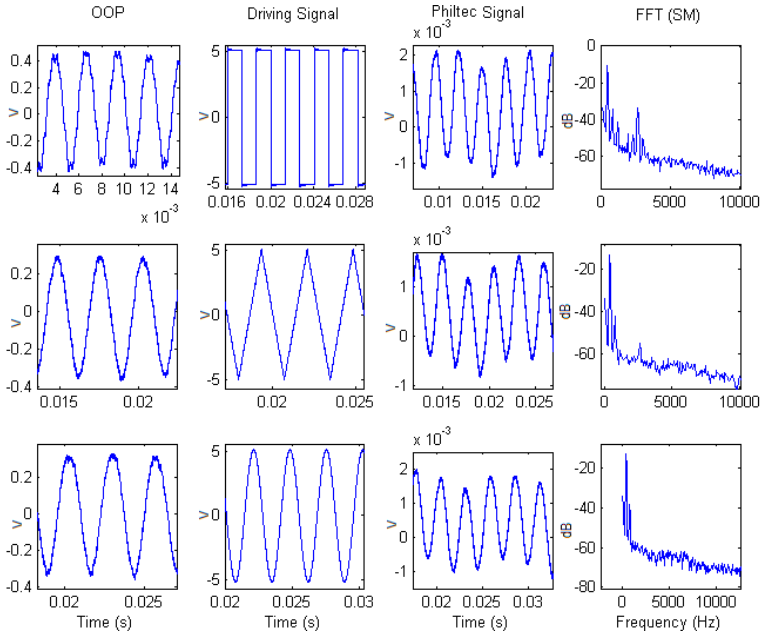

Figure III.24 Experimental results for different shapes of excitation

Next the linearity of the sensor was tested as the Figure III.25 shows the measured displacements for a sinusoidal excitation signal and amplitudes of *1*, *2*, *4*, and *5V* the resulting measured power is in the next table.

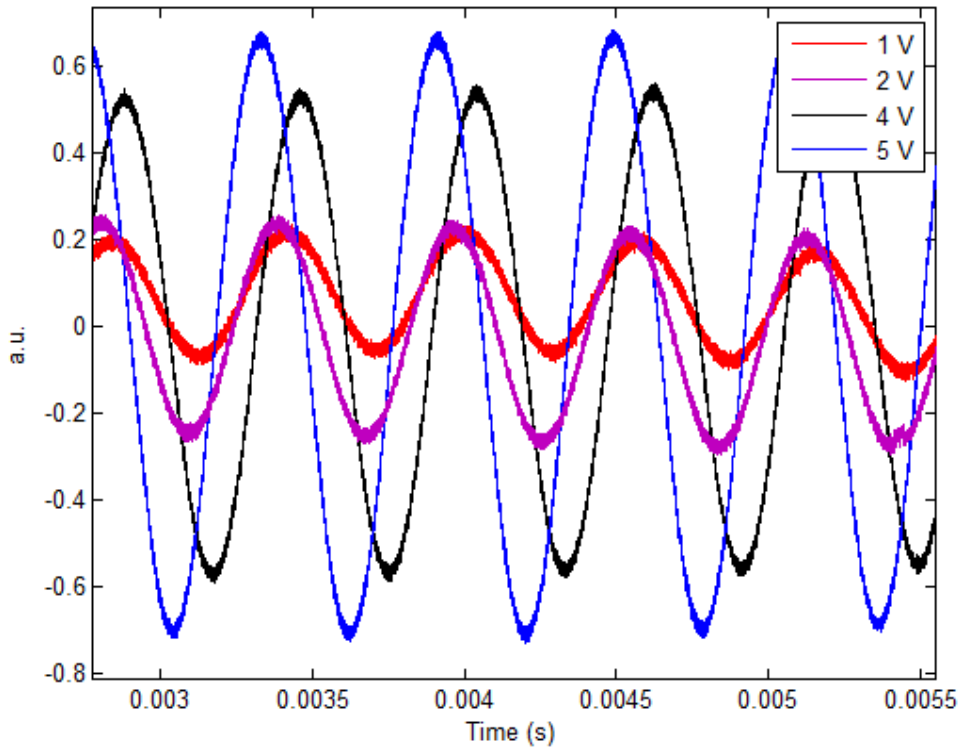

Figure III.25 Reconstruction of the displacements for excitations of 1, 2, 4 and 5V.

Table III.1 shows in bold the theoretical proportions of the amplitude of the driving signals while in italic are reported the proportions of the amplitudes of the OOP.

Amplitudes (a.u.)	***0.30767***	***0.5277***	***1.1323***	***1.4049***
0.30767		*0.5*	*0.25*	*0.2*
0.5277	**0.583**		*0.5*	*0.4*
1.1323	**0.272**	**0.466**		*0.8*
1.4049	**0.219**	**0.376**	**0.806**	

Table III.1. OOP's amplitudes obtained for sinusoidal displacements with a generating signal amplitudes of 1,2,4, and 5V.

The average error reflecting the linearity of the sensor as measured experimentally is of approximately *8%* which is very acceptable considering the fact that the PZT itself will not respond linearly to these different amplitudes.

On the other hand, the FFT of the SM signal was compared to the FFT of the transfer function approximated to be equal to the FFT of the impulse response multiplied by the FFT of the driving signal. Once again, both spectrums showed similarities. The main frequency was measured to be at *366.2Hz* by the SM sensor, whereas, it was found to be *360.1Hz* through the approximation of the mechanical displacement corresponding to an error of *1.7%* which is acceptable.

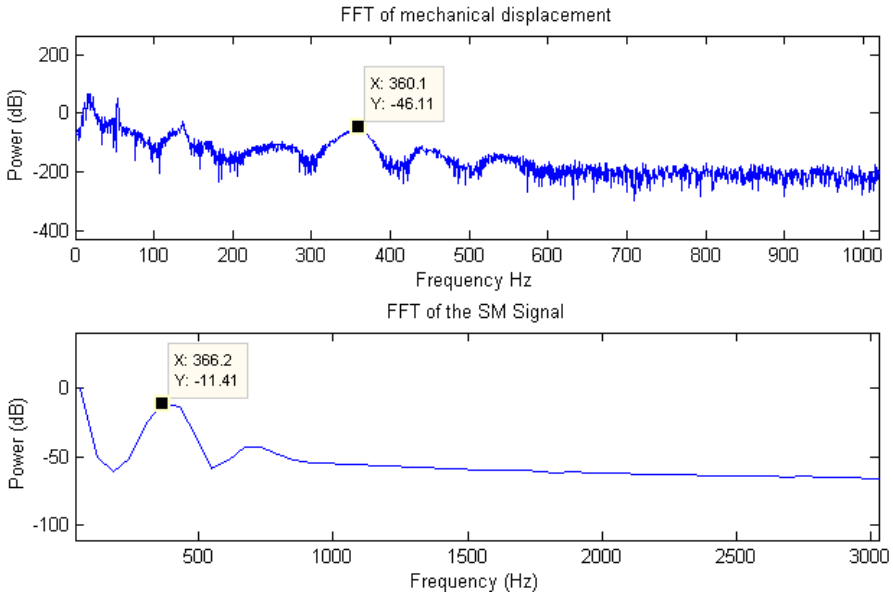

Figure III.26 FFT of the approximation of the mechanical displacement compared to the FFT of the OOP under strong feedback. X represents the frequency in Hz and Y the power in dB.

III.5. Simulation Results

III.5.1. Study of The Linearity of The System

The linearity of the self-mixing signal was furthermore investigated through different simulation using the behavioral model [57] in the case of strong feedback.

First, the transfer function of the laser diode under strong feedback was estimated for different values of *C* and for the same displacement amplitude.

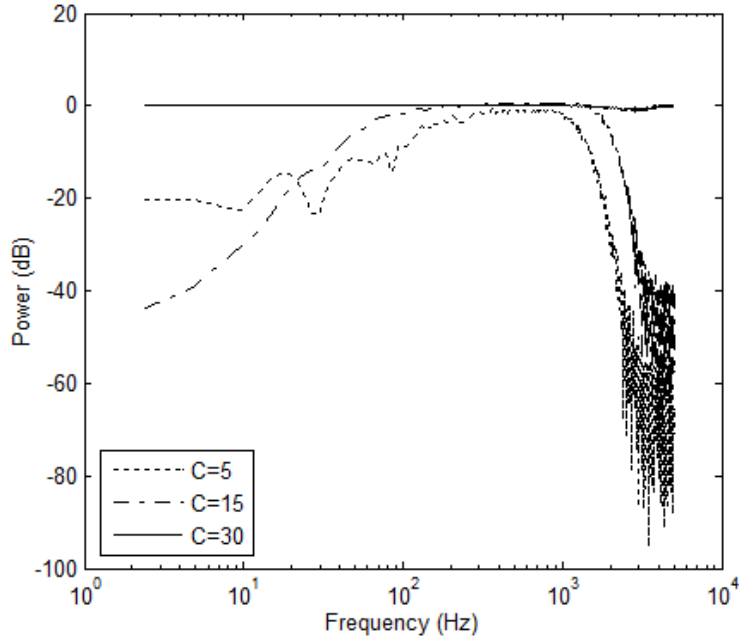

Figure III.27 Transfer function estimation for different levels of feedback of C=5, 15 and 30 and a constant amplitude of displacement.

Figure III.27 shows the estimation of this transfer function using the Welch method [75] for *C=5*, *15* and *30* respectively for the same amplitude of displacement. This transfer function shows a linearity that increases with the values of *C*. For *C=5* the low-pass frequency of the system is around *166 Hz* and its high-pass frequency is around *1160 Hz*. These values passes respectively to *76 Hz* and *1170* for *C=15* and finally for *C=30* the system will be perfectly linear all over the considered frequency spectrum.

The system's linearity was studied furthermore using the correlation function. This function can be defined between two signals (*x* and *y*) at a certain frequency

(ω) in terms of power spectral of both signals ($R_x(\omega)$ and $R_y(\omega)$) densities and cross-spectral density ($R_{xy}(\omega)$) as follows:

$$C_{xy}(\omega) = \frac{|R_{xy}(\omega)|^2}{R_x(\omega) R_y(\omega)} \tag{3.18}$$

In fact the coherence function will have values between *0* and *1* where *0* will correspond to uncorrelated signals and *1* to perfectly correlated signals.

Figure III.28 shows the coherence functions for different values of *C* and different amplitudes of displacement *a*. It exhibits a strong influence of the augmentation of the amplitude of vibration on the coherence function. This influence may be compensated by an increase of *C*, the coherence function keeping a value around 0.8 even for high amplitudes when the feedback is strong enough. This coherence function is ameliorated with respect to the hypothesis of small fluctuations of $x_F(t)$ and high-values of *C*.

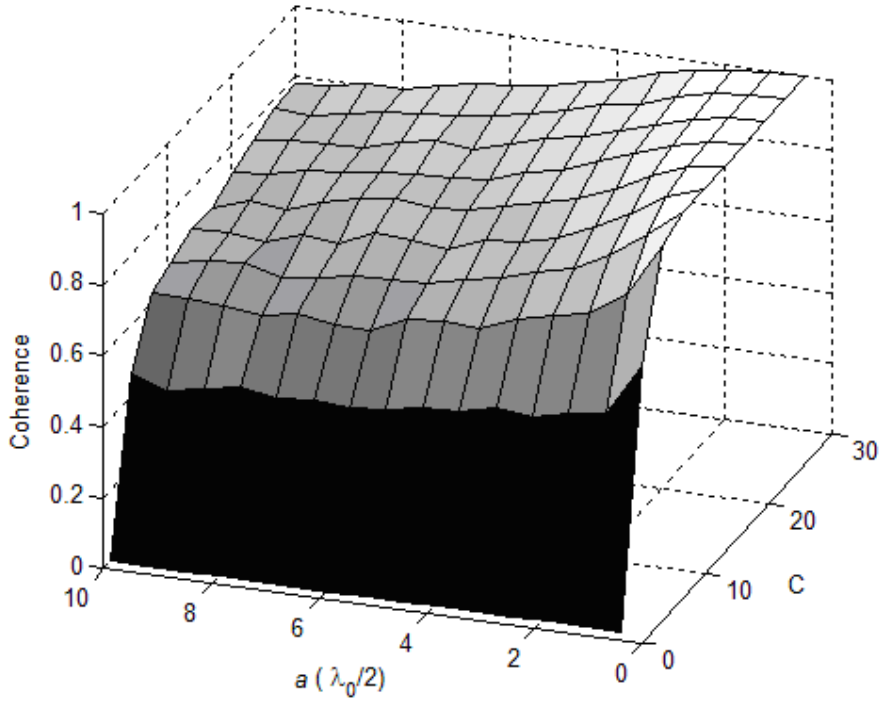

Figure III.28 Coherence function for different values of a and C.

Figure III.29 shows different transfer function estimations for a *C=25* and for different amplitudes of *10*, *20* and *30*$\lambda_0/2$. The augmentation of the amplitude induces a degradation of the transfer function similar to the one caused by the diminution of the coupling coefficient.

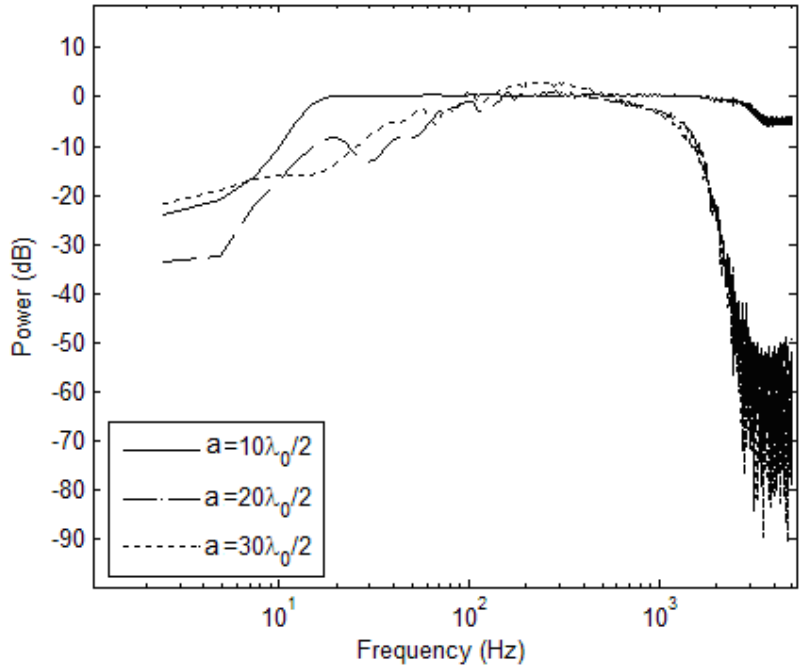

Figure III.29 Transfer function estimation for the same level of feedback of C=25 and different amplitudes of displacement.

These results are in good accordance with the previously-reported theoretical analysis showing the relationship between *C* and *a* to obtain the strong feedback regime [76]. It demonstrated that an OOP without fringes can be observed even for small values of *C* if *a* is small enough (Figure III.4).

III.5.2. Analysis of the total harmonic distortion

The previous study showed that some non-linearities may appear for high amplitudes of displacement or when the coupling coefficient is not high enough. Thereby, the effect of these non-linearities was investigated through a study of the total harmonic distortion (THD) that expresses the power added by the system at the harmonics of the input's fundamental frequency:

$$THD = \sqrt{\frac{\sum_{i=2}^{NH} U_i^2}{U_1^2}} \qquad (3.19)$$

Where NH is the number of the studied harmonics and U_i is the voltage found at each of these harmonics whereas, U_1 is the voltage measured at the fundamental frequency of the signal.

The THD was plotted as a function of *C* for different values of a (Figure III.30). It shows that for the same amplitude of displacement the TDH increases

generally when values of *C* decrease. This figure also shows that for increasing amplitudes of displacement the TDH will have values that are also increasing generally.

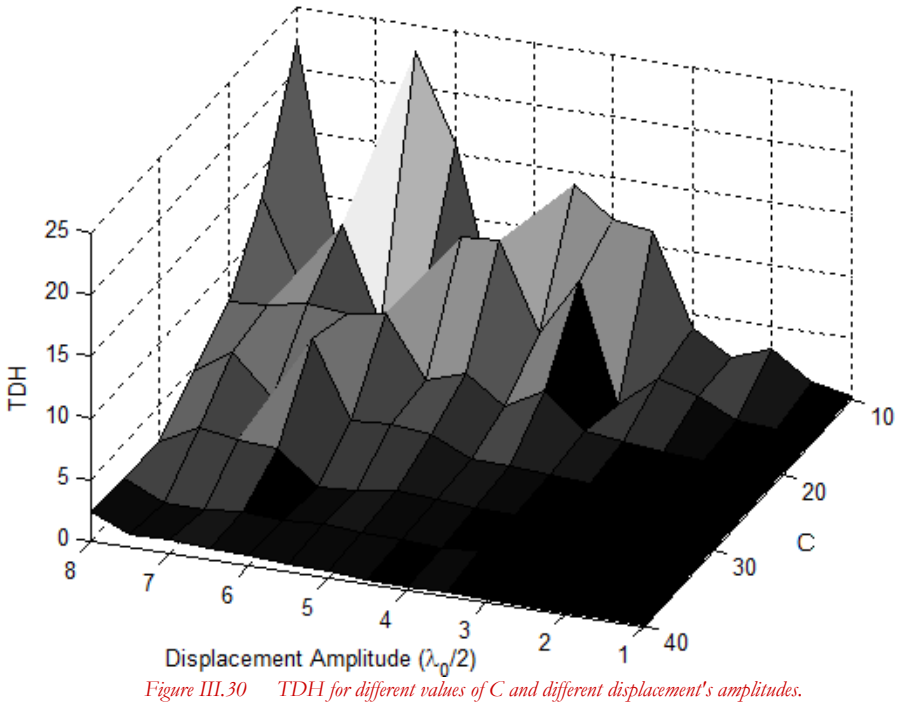

Figure III.30 TDH for different values of C and different displacement's amplitudes.

Similarly this study showed a decreasing TDH for increasing values of *C* and decreasing values of *a*. However the TDH is generally under *10%* which is relatively low.

III.6. Experimental Results

III.6.1. Experimental Analysis of The System's Linearity

The time consuming frequency sweeping method used previously with SM sensors [72]-[77] is not needed anymore as a noise covering the whole frequency spectrum can be applied directly to the structure. The sensor will then provide a complete spectrum response from only one measurement.

The experimental setup consisted of a piezoelectric transducer (PZT) used as a target at a distance of approximately *1m*. The PZT was driven by a quasi-white noise generated by the sound card of a computer. The reference measurement was provided by a capacitive sensor mounted inside the PZT having an announced resolution of *2nm* and a linearity of *1%*.

The sensor was firstly tested with the PZT surface covered with a blue micro-prisms retro-reflective adhesive paper that represented a very cooperative target for the strong feedback regime.

Figure III.31 shows the transfer function estimation (TFE) still using the Welch method [75] between the different considered signals. In plain line is the transfer function between the displacement as provided by the capacitive sensor (*d(t)*) and the self-mixing signal (*sm(t)*). The dashed line is the transfer function between the driving signal of the PZT *g(t)* and *sm(t)*. Finally, the dotted line is the transfer function between *g(t)* and *d(t)*.

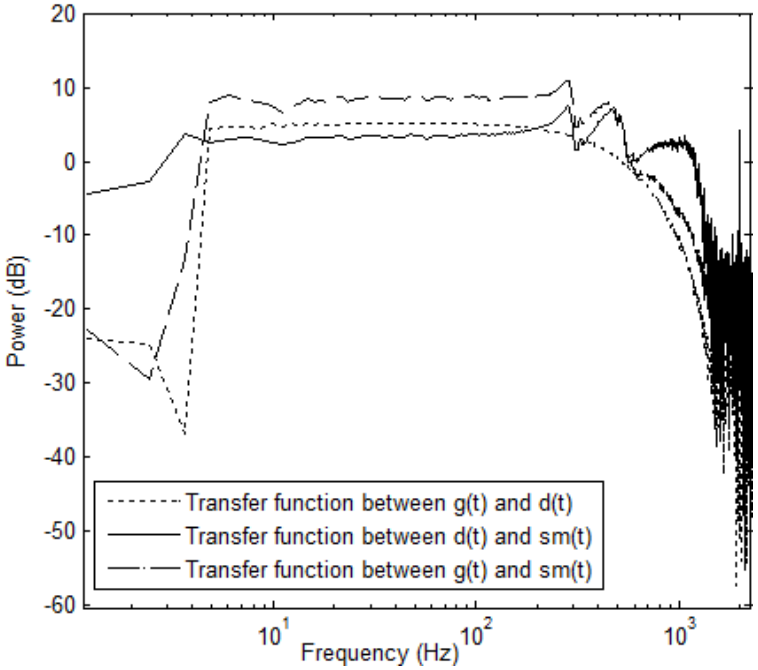

Figure III.31 Transfer function estimation between the different acting signals where g(t) is the driving signal, d(t) is the displacement as measured by the capacitive sensor and sm(t) the OOP fluctuations of the self-mixing sensor.

It can be seen from both TFE between *sm(t)* and *g(t)* and between *sm(t)* and *d(t)* that the sensor showed a very high linearity between *4 Hz* and *1 Khz* considering a *4 dB* margin. On the other hand, the degradation of the system's linearity beyond *1 Khz* was caused (partially or completely) by the PZT itself as verified through the TFE between *g(t)* and *d(t)*.

The coherence function between the self-mixing signal and the displacement showed a strong correlation in the considered bandwidth (Figure III.32). The coherence had a value higher than *0.9* for frequencies up to *800 Hz* and conserved a value higher than *0.7* for frequencies up to *1 Khz*.

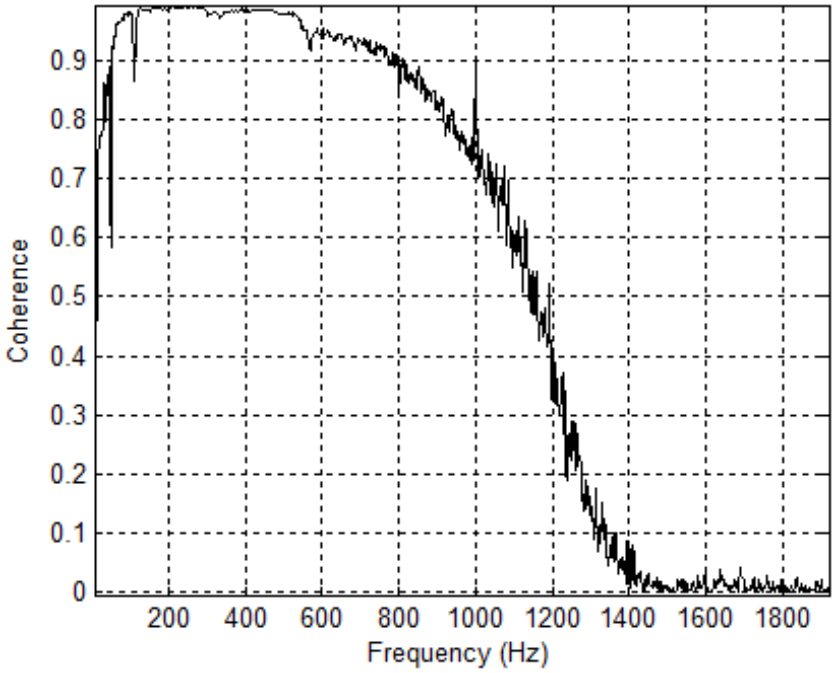

Figure III.32 Coherence function between the SM signal and the displacement as provided by the capacitive sensor

The results found experimentally proved the high linearity of the sensor and its compatibility for different modal analysis applications.

III.6.2. Effect of The Target's Surface Type

Equation (3.9) showed analytically that the response of the sensor did not depend on the reflectivity of the target nor the coupling efficiency. In order to verify this theory, the previous experiment was repeated for other types of surfaces such as a gray micro-sphere adhesive paper or the metallic surface of the PZT itself which is representative of surfaces used in mechanical structures (Figure III.33). Finally in order to point out the limitations of the system, a target consisting of a very rough sandpaper was used.

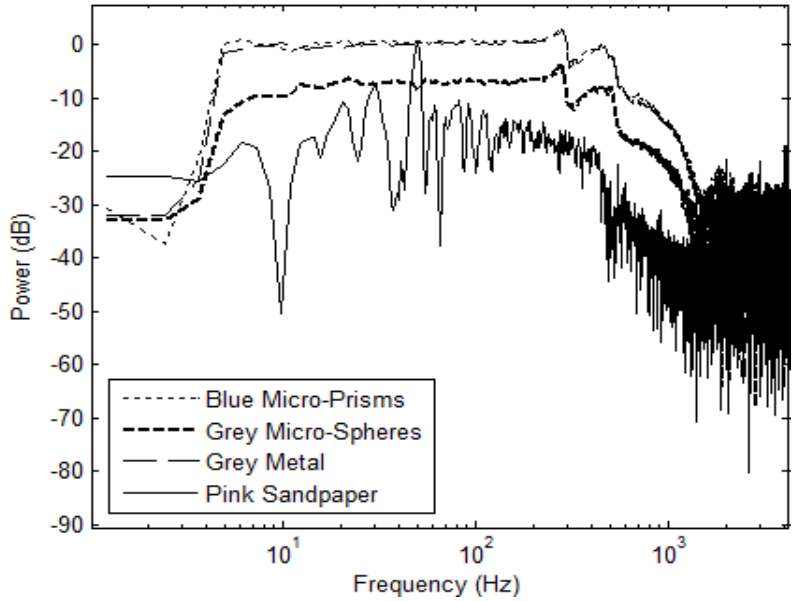

Figure III.33 TFE for different surface types of blue micro-prisms, grey micro-spheres, gray metallic surface of the PZT itself and pink sandpaper.

The system showed similar linearities for all of the surfaces and had very similar transfer functions in exception of the sandpaper.

The coherence function was also plotted for the three first surfaces (Figure III.34). These coherence functions confirmed the results obtained with the transfer function estimations. The linearity of the system is relatively independent from the reflectivity of the considered surface. The displacement and the SM signal are strongly correlated for different types of surfaces whenever the sensor is kept in the strong feedback regime.

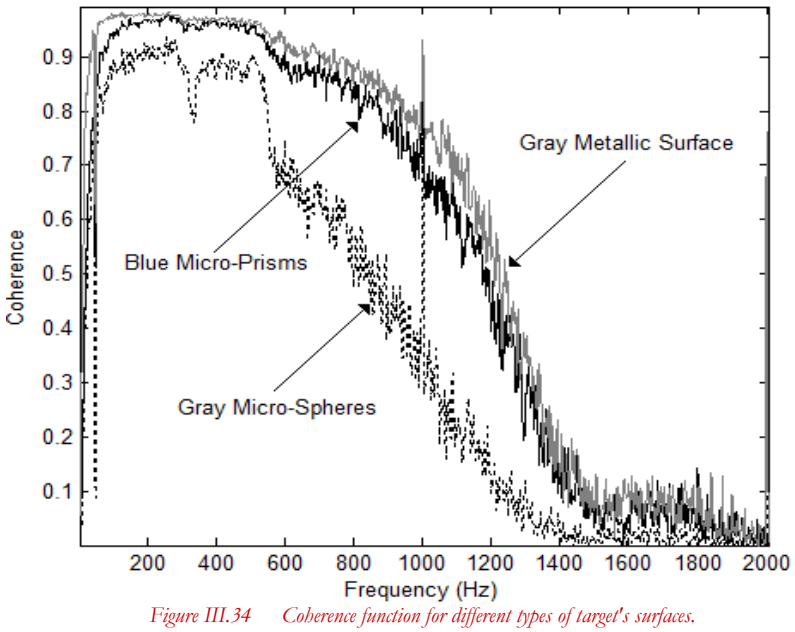

Figure III.34 Coherence function for different types of target's surfaces.

Although the sandpaper experience did not give the expected results it had a major interest as it showed that for low amplitude vibrations, the OOP variations without fringes are obtained, the SM signal being compared to the displacement after elimination of the noise from both of them (Figure III.35).

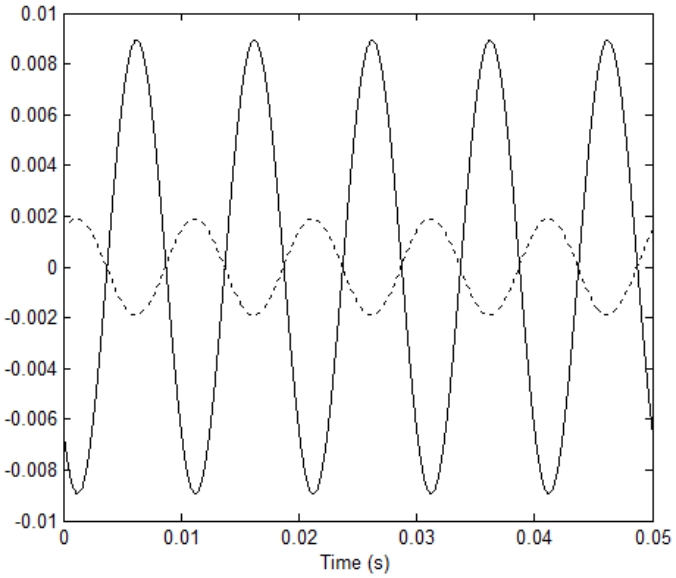

Figure III.35 OOP signal compared to the displacement (in dotted line) for a very rough sandpaper surface (after noise elimination).

By increasing the vibration amplitude, fringes appeared and the usual fading caused by the speckle effect was clearly observed (Figure I.13) [66].

As a consequence, a sensor subject to strong feedback is more robust to this disturbance even if the difficulty is to maintain the sensor under this regime with such rough targets. The differences obtained between the rough target and the cooperative targets can be explained by the approximations in the Lang-Kobayashi equations [74] traditionally used for describing the self-mixing effect.

As a matter of fact, contributions from non-linear gain suppression, spontaneous emission, and multiple reflections are neglected. Moreover, local variations of C due to fluctuations in the amplitude and the phase of the scattered light because of the random pattern of the target surface are not yet considered in the behavioral model.

III.6.3. Relative Displacement Measurements

This sensor has proven throughout simulations and experimentations to be linear in the case of high values of C and low displacement amplitudes. Moreover, considering usual targets for mechatronic applications, this sensor is fairly robust to the influence of the speckle effect and relatively independent of the reflectivity of the surface.

All these characteristics make this sensor very attractive for displacement measurements. However, the gain coefficient expressed in equation (3.13) has a statistical aspect as caused by D_0 and k_0 fixed arbitrary each time the sensor is powered.

This statistical aspect of M_2 restricts the displacement measurements possible using this sensor to the case of only relative displacement measurement and not absolute displacement.

In the following experiment displacements with different amplitudes were measured by both the capacitive sensor and the self-mixing and Table III.2 shows the different measured amplitudes. It is to note that all these measurements were made without turning off the laser thereby it is possible also to verify how much M_2 will be experimentally constant.

Capacitive Sensor (µm)	*SM Sensor (V)*	*M_2 (µm/V)*	*Displacement considering $\overline{M_2}$ (µm)*	*Error (nm)*	*Error (%)*
0.2204	0.0322	6.8447	0.2253	4.9	2.2%
0.3344	0.0486	6.8806	0.3401	5.7	1.7%
0.4473	0.0628	7.1226	0.4396	7.7	1.72%
0.7265	0.1016	7.1506	0.7112	15.3	2.1%

Table III.2. Different M_2 calculations without turning off the laser for different displacement amplitudes.

This table shows an average conversion factor of $\overline{M_2} = 6.9996\,\mu m/V$ for these different four measurements. This leads to an average error of *1.93%* in respect to the average value. This proves that M_2 is fairly constant while the laser is not turned off.

Furthermore, this shows that the laser is able to accomplish absolute displacement measurement if calibrated each time it is powered.

Table III.2 shows that this absolute displacement may be measured with an average precision of *8.4 nm* without the need of any signal processing.

In order to test the relative displacement measurement ability of this sensor the measured displacements in table I should be compared and reported to each others. In fact, Table III.3 shows, in italic, the different proportions of the displacement's amplitudes measured by the capacitive sensor (i.e. *0.2204/0.3344*) whereas in bold, are reported the proportions of the displacement's amplitudes measured by the SM sensor (i.e. *0.0322/0.0486*).

	0.0322	**0.0486**	**0.0628**	**0.1016**
	0.2204	*0.3344*	*0.4473*	*0.7265*
0.0322				
0.2204	**X**	**X**	**X**	**X**
0.0486	**1.51**			
0.3344	*1.51*	**X**	**X**	**X**
0.0628	**1.95**	**1.29**		
0.4473	*2.03*	*1.34*	**X**	**X**
0.1016	**3.15**	**2.09**	**1.62**	
0.7265	*3.3*	*2.17*	*1.62*	**X**

*Table III.3. Relative displacement measured by the capacitive sensor (in italic) and by the SM sensor (**in bold**). Values to be compared are symmetrically disposed from one side and the other of the diagonal (**X**).*

This table shows that this sensor has a good linearity and is able to accomplish relative displacement measurement with an average error of *2.64%* without the need of any signal processing.

III.7. Conclusion

In this chapter, a self-mixing sensor operated under strong feedback was conceived and characterized in terms of precision, linearity and harmonic distortion.

In the first part of this chapter, the strong feedback regime was presented by studying the peak free signals and simplifying the behavioral model in the particular case of this regime. Afterwards, this statistical aspect was studied in details depicting the effect of different key parameters such as a, C or φ on the performances of this type of sensors. φ proved to be more of a second order

parameter when compared to the effect *a* and *C* had where increases of *C* or decreases of *a* ameliorate significantly the performances of such sensors.

The second part, introduced the conception and characterization of relative displacement sensor in terms of linearity and total harmonic distortion through different simulations and different experiments where it showed a good linearity increasing when *C* increases or *a* decreases.

This sensor was able to accomplish relative displacement measurements with a relative error less than *2%* and a linearity of approximately *2.6%* both of these being defined experimentally.

Chapter IV. Strong Feedback Sensor for Modal Analysis

IV.1. Introduction

In the pervious chapter, a self-mixing sensor using a laser diode under strong feedback was conceived and characterized. This sensor showed a lot of advantages for modal analysis where it provided a signal directly related to the displacement in terms of amplitude and frequency which can be very useful for real time modal analysis [78].

Experimental modal analysis methods are investigation methods recently developed in order to ameliorate the conception of dynamical models of real structures. In fact, the parameters that allow to have a full representation of the dynamical behavior of a linear structure, whatever its complexity is, may be resumed into a certain number of key modal parameters such as the resonance frequencies, the damping coefficient and the modal vector etc…

Resonance frequencies are the excitation frequencies for which the studied object vibrates with an amplitude abnormally high which may cause its destruction such as the famous historical issue of the "Basse-Chaîne" bridge at Angers, France which was destructed in 1850 by soldiers marching causing the death of 226 of them. Modal vectors, represents the form of deformation of the studied object when excited at one of its resonance frequencies; in the case of the bridge, previously cited, the modal vector associated to the lowest resonant frequency has a U form.

Thereby, modal analysis can serve as a predictive study where mechanical fatigue will induce a progressive modification of the vibration spectrum i.e. a shifting of the resonance frequencies or changes in the modal vector.

This phenomenon was investigated in the aviation field where they were affronted to the problem of “undulation” of airplanes. In this phenomenon, the aeroelastic coupling between the air and the structure of the plane induced at

certain speeds generates a phenomenon of vibrations auto-excited able to destruct the structure. This can be predicted if the dynamical characteristics of the structure were known.

In this chapter, the sensor characterized in the previous chapter will be applied for modal analysis purposes where in the first part simulations will show the quality of frequency response of this type of sensors. In the second part, this sensor will be tested in order to test a thin clamped plate and then in the third part to test carbon fiber beams. In both cases, the response of the sensor will be compared to counter-measurements provided by different types of sensors.

IV.2. Modal Analysis and Self-Mixing

The first methods developed between 1950 and 1960 consisted of applying to the structure a group of stimulating forces having an amplitude and a phase chosen in a manner to have a response proportional to a characteristic mode of the associated conservative system (Figure IV.1) [79]. These methods are very reliable because the investigator can depict each parameter by itself, but they are very costly in terms of implementation and needs important investments.

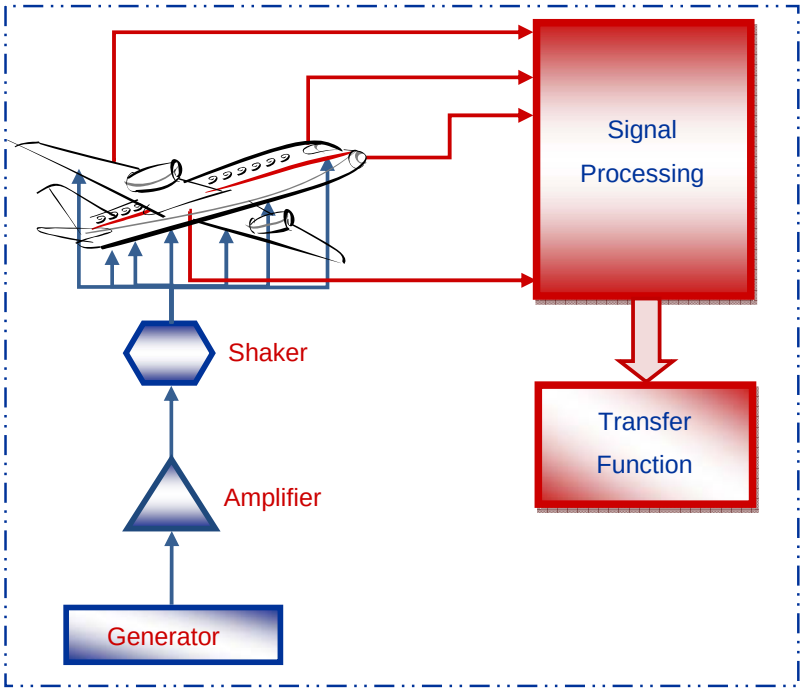

Figure IV.1. Schematic of the general methods of experimental modal analysis.

Another type of experimental modal analysis techniques is to apply a white noise excitation to the structure and to exploit its response having thereby the response of all the vibration modes all over the frequency spectrum without the need of any frequency sweeping. However, this type of methods requires, from the used sensor, a high fidelity to the vibration of the structure. [79]

Different studies of the use of self-mixing sensors in the field of modal analysis were accomplished such as the conception of a self-mixing sensor for vibration measurement or defect detection [77] or for structural analysis and damping evaluation [72].

The advantage of such non contact sensors in this type of applications is that they have a very competitive price compared to other optical sensors.

The main addition for the use of self-mixing sensors under strong feedback is the fact that they provide a real time image of the displacement in terms of frequency and amplitude of displacement. This enables the use of white noise excitations and to have a direct complete transfer function covering the whole vibration spectrum without the need of any signal processing other than a Fast Fourier Transform (FFT) which simplifies the time consuming measurement iterations used before such in [72].

IV.3. Simulation Results

The behavioral model developed earlier [57] permitted simulations of self-mixing signals in all the feedback regimes. In this paragraph it is used in order to simulate the response of a laser diode when submitted to feedback caused by a moving target at a distance of *40cm* which was excited by a white noise displacement.

Figure IV.2 shows how a laser diode subject to a strong feedback (*C=60*) will follow the displacement discarding its shape and here after an example of a white noise displacement.

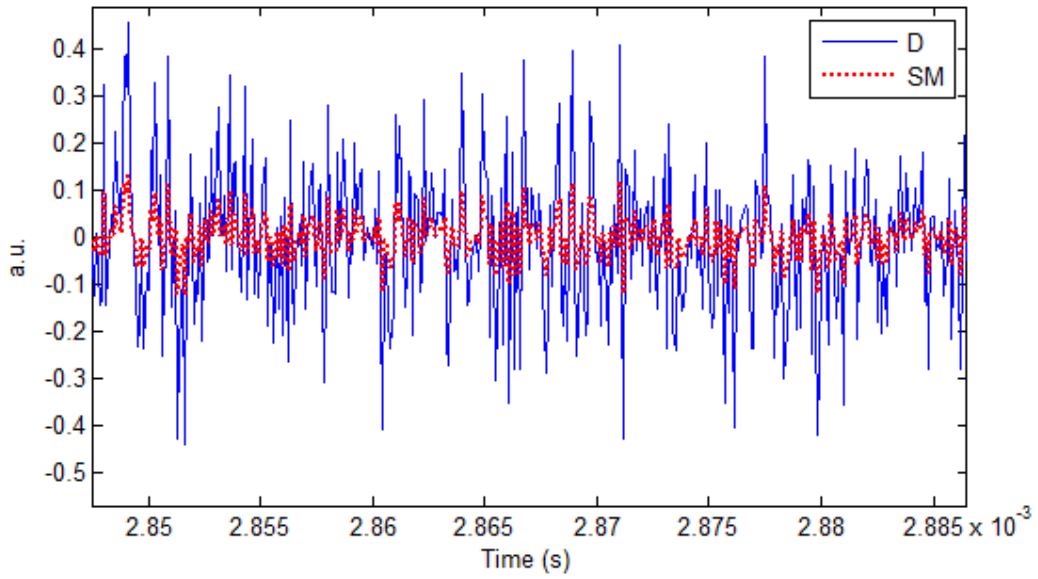

Figure IV.2. Simulation of the time response of a white noise displacement and the corresponding self-mixing signal.

However, it is not the time domain which is the most important for modal analysis where, as mentioned earlier, the main aim is to determine the resonance frequencies and the modal vector. Hence, the interest will be in a frequency domain analysis as in Figure IV.3.

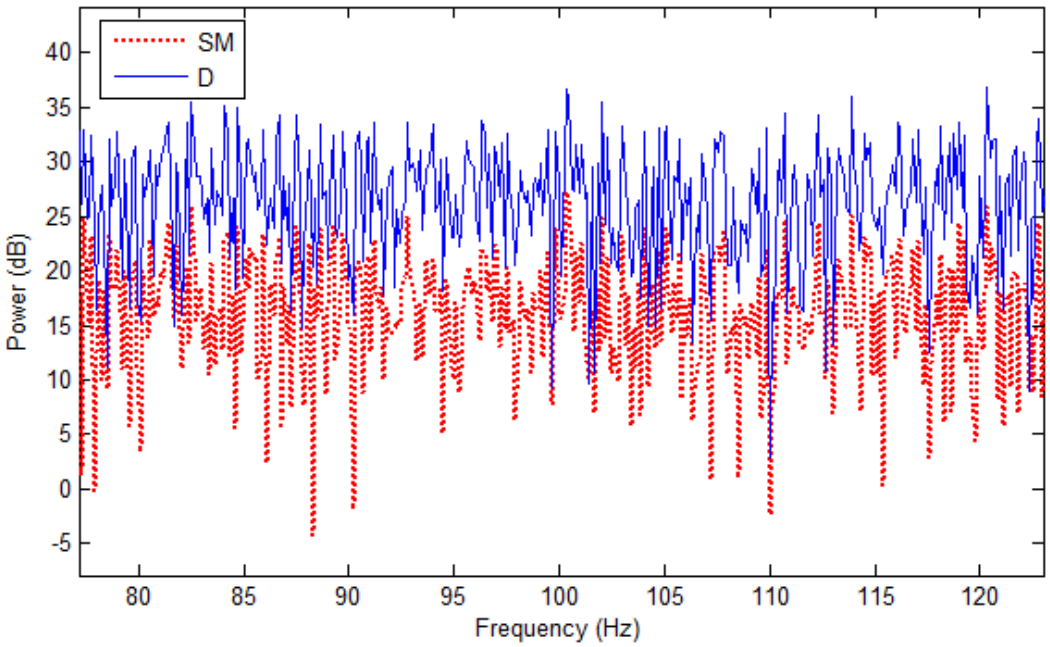

Figure IV.3. Simulation of the frequency response of a white noise displacement and the corresponding self-mixing signal.

This figure shows the frequency spectrums of both signals shown in Figure IV.2 where a similitude in both frequency and time domains can be seen which makes this sensor very suitable for modal analysis applications.

IV.4. Experimental results

IV.4.1. First experiment: PZT as a target

The ability of the sensor to determine the vibration frequencies of a structure was first studied with simple structures such as a PZT excited by a sinusoidal signal at different frequencies of *330*, *500*, *850* and *1000Hz* respectively. Figure IV.4 is a zoom of Figure III.23. It shows the comparison of the FFT of both the SM signal (*SM*) and the displacement provided by a capacitive sensor (*D*). It can be seen how the OOP follows exactly the signal of the capacitive sensor for frequencies up to *1500Hz*, this limit being chosen only for visual clarity reasons.

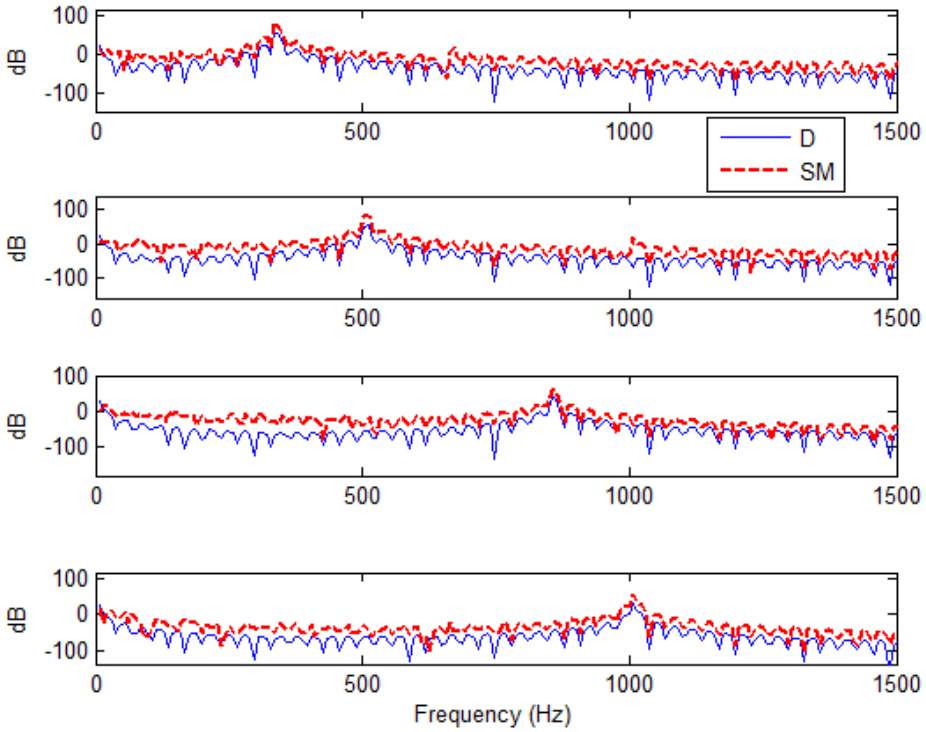

Figure IV.4. FFT of the displacement given by both the SM sensor and the capacitive sensor for different excitation frequencies.

Looking closer at these signals the FFTs of the self-mixing signals plotted above were gathered in one figure (Figure IV.5) showing how closely the OOP's frequency followed the displacement frequency.

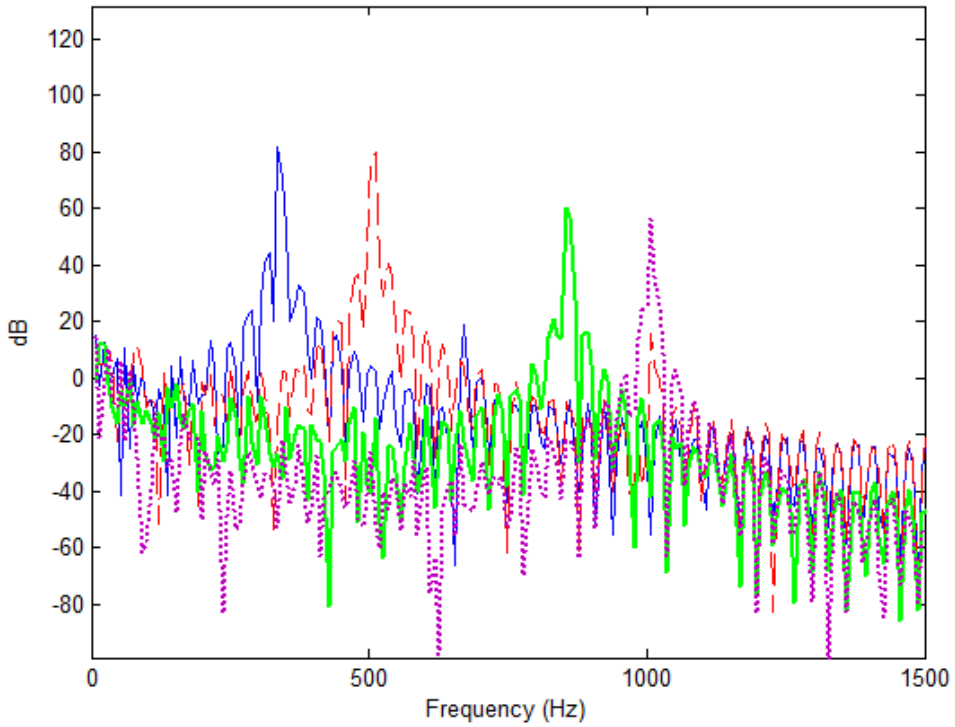

Figure IV.5. FFT of the SM for different excitation frequencies of 300, 500, 800 and 1000Hz.

Moreover, the frequency spectrum of the response of the PZT was measured by the SM sensor and compared to the one obtained by the capacitive sensor for different driving signals (sinusoidal, triangular and square) considered at the same frequency of *330Hz* (Figure IV.6).

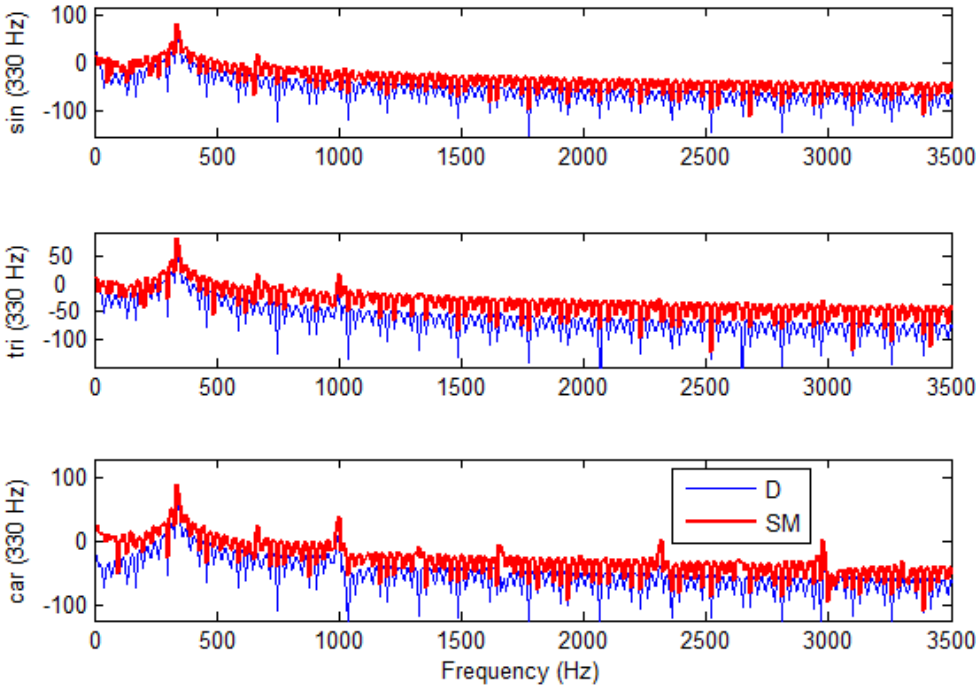

Figure IV.6. FFT of the displacement given by both the SM sensor and the capacitive sensor for different generating signals.

It can be seen that both signals showed good similarities for the whole studied spectrum. For example, in the case of a square driving signal, as expected, the odd harmonics are more accentuated than in the case of other signals.

This study was completed by a calculation of the TDH in the case of real experimental signals. Figure IV.7 shows the power spectral density of both the sinusoidal driving signal and the SM signal respectively.

Calculating the power injected by the SM sensor at the harmonic frequencies the TDH may be calculated. It is found to be *2.08%* using equation (3.19).

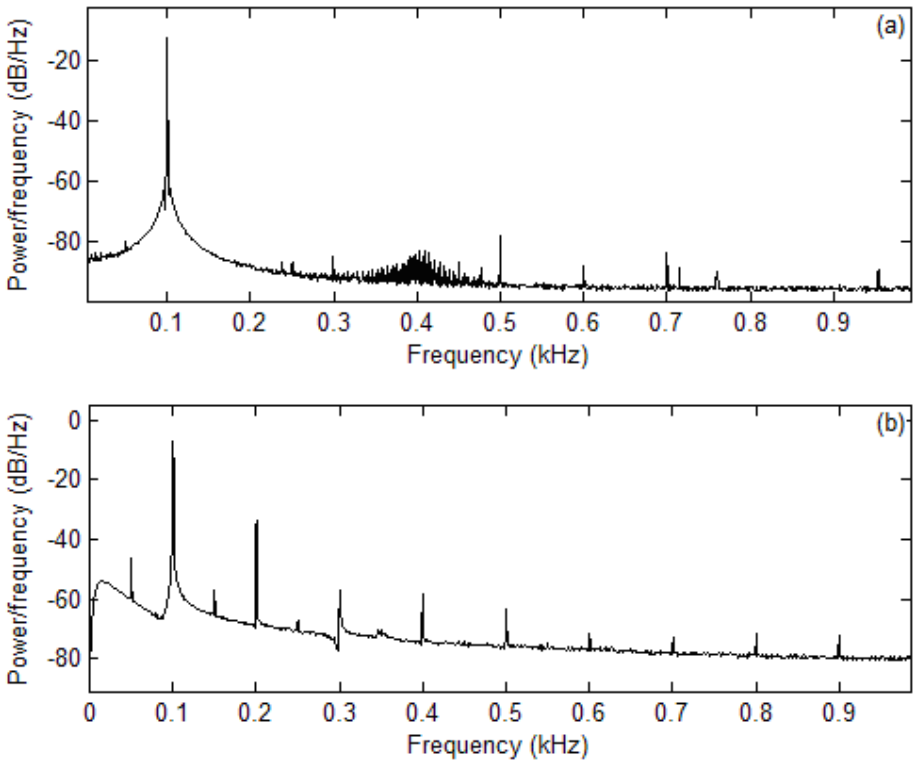

Figure IV.7. PSD of the driving signal (a) and the self-mixing signal (b) respectively.

Finally, in order to study a realistic application of such a type of sensors in modal analysis, a white noise was applied to the PZT and the FFTs of the displacements measured by both the capacitive sensor and the self-mixing sensor were plotted in Figure IV.8.

This figure shows a high similarity between the two observed spectrums. A frequency span of only *1500Hz* was considered for clarity issues. Looking at the whole frequency spectrum of the excitation frequencies shows even a higher similitude between both signals all over the studied frequency span.

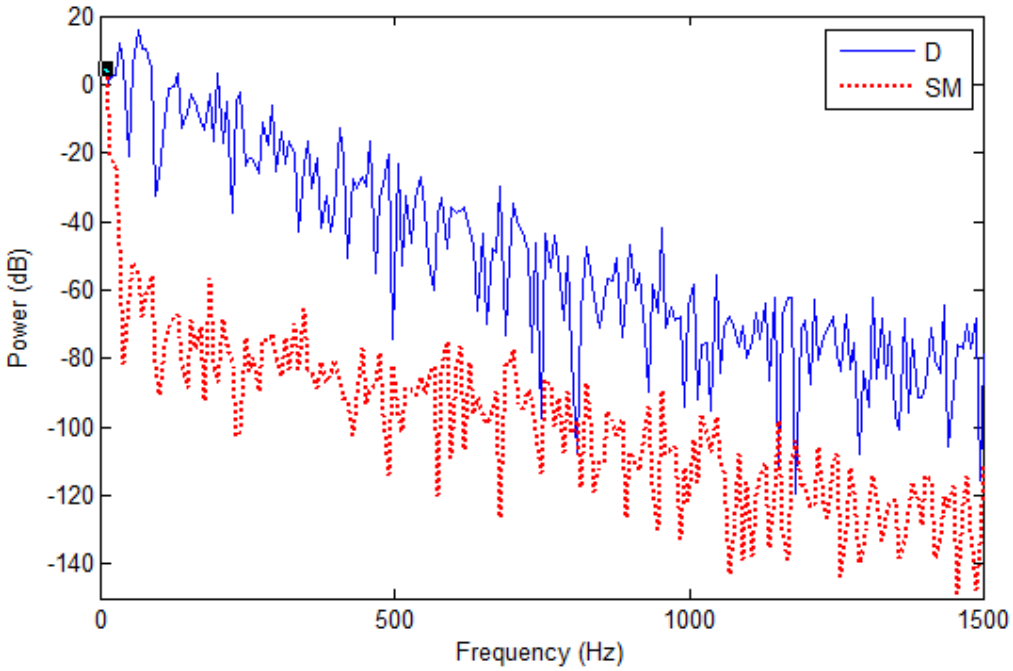

Figure IV.8. FFT of the displacement as measured by the capacitive sensor and by the SM sensor.

IV.5. Thin Clamped Plate

The second experiment was conducted using a thin plate that was clamped very tightly inside a metallic frame. During the first experiments only one laser was used pointing at a micro-prism adhesive paper posed on top of an accelerometer providing the counter-measurement. The excitation was created using a hammer with a force sensor installed on top of it. The shocks were done in a way not to have big amplitude of displacement in order to keep the laser in the strong feedback without inducing any peaks in the self-mixing signal. However, one or two peaks will not deteriorate the measurement since they will be induced at a high frequency relatively to the frequencies mechanically interesting. The next figure shows the schematic of the conducted experiment.

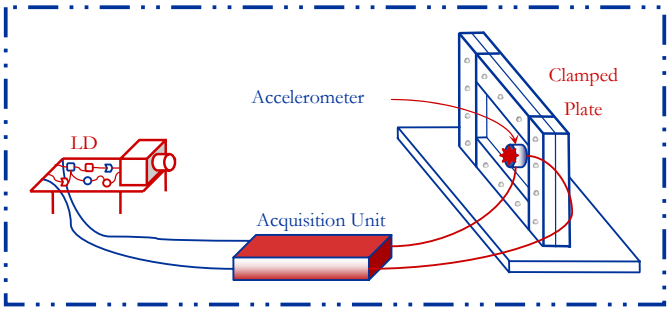

Figure IV.9. Schematic of the first modal analysis experiment.

IV.5.1. Mechanical Theory of Thin Plates

In order to better understand the measurements of vibration of such plates, first of all it is necessary to define a thin plate and to determine the equations of its resonance frequencies.

In fact, a thin plate can be defined as a plate with a thickness h very small when compared to its width a' and its length b. In this particular case, the Kirchoff's hypothesis of thin plates can be applied.

This hypothesis consists of two main points:

- The transverse component of the stress tensor is negligible.
- Any straight cross section normal to the middle plane remains straight during the deformation.

In a more general way, for a clamped plate, the resonance frequencies corresponding to the different vibration modes can be obtained from the following equation:

$$f_{ij} = \frac{\lambda_{ij}^2}{2\pi a'^2}\left[\frac{Eh^3}{12\gamma'\left(1-\nu^2\right)}\right]^{\frac{1}{2}}; \quad i=1,2,3,...; j=1,2,3,... \tag{4.1}$$

Where λij is a parameter depending on the studied mode defined in the next tables. E is the module of Young ($E=69000\ MPa$ in the case of aluminum), ν is the Poison's ratio ($\nu=0.345$ for aluminum) and γ' is the weight per unit of surface.

The next figure shows the dimensions of the plate used in this experiment which allows us to calculate $\gamma'=M/a'.b=8.018Kg/m^2$.

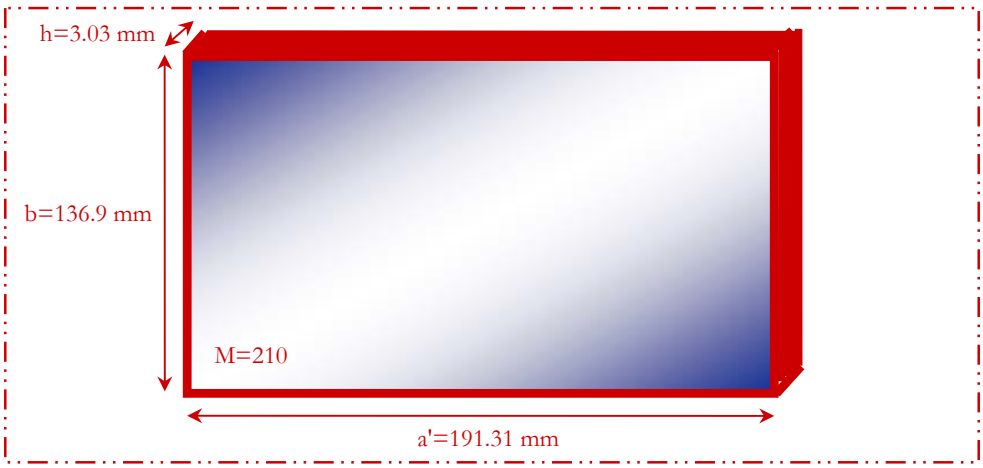

Figure IV.10. Dimensions and weight of the used plate

λ_{ij} (ij)	Mode Sequence					
a'/b	1	2	3	4	5	6
0.4	23.65 (11)	27.82 (12)	35.45 (13)	46.7 (14)	61.55 (15)	63.1 (21)
2/3	27.01 (11)	41.72 (12)	66.14 (21)	66.55 (13)	79.85 (22)	100.9 (14)
1	35.99 (11)	73.41 (21)	73.41 (12)	108.3 (22)	131.6 (31)	132.2 (13)
1.397	**45.82**	**81.53**	**103.33**	**124.75**	**150.7**	**169.8**
1.5	60.77 (11)	93.86 (21)	148.8 (12)	149.74 (31)	179.7 (22)	226.9 (41)
2.5	147.8 (11)	173.9 (21)	221.5 (31)	291.9 (41)	384.7 (41)	194.4 (12)

Table IV.1. λ_{ij} factor for the different possible modes [86][80].

In our case $a'/b = 1.397$ the corresponding values of λ_{ij} can be then calculated through an interpolation. They will be noted in bold in the previous table.

Then, it will be possible now to write the resonance frequencies as a function of λij as follows:

$$f_{ij} \approx 20.4 * \lambda_{ij} \tag{4.2}$$

f_{ij} (Hz)	Mode Sequence					
a'/b	1	2	3	4	5	6
1	734.2	1497.56	1497.56	2209.32	2684.64	2696.88
1.397	**934.73**	**1663.21**	**2107.93**	**2544.9**	**3074.28**	**3463.92**
1.5	1239.71	1914.74	3035.52	3054.7	3665.88	4628.76

Table IV.2. Resonance frequencies of the different possible modes of the considered plate.

Going back to Table IV.1 the resonance frequency is calculated in all the cases of $a/b=1$, 1.397 and 1.5 and represented in the Table IV.2.

This will give theoretical values of the resonance frequencies to compare with the different measurements accomplished later in this paragraph. However, it is to be kept in mind that many approximations were done in order to get these values where the plate was not homogenous nor perfectly rectangular nor perfectly clamped. Moreover, the exact alloy of aluminum was not known which adds more imprecision to the values of the module of Young and the Poisson ratio.

IV.5.2. Experimental Results:

IV.5.2.a. Clamped Plate

As mentioned earlier, the first experiment was conducted with only one laser pointing on top of the accelerometer and acquiring instantaneously the

acceleration measured by the accelerometer and the displacement achieved by the self-mixing sensor.

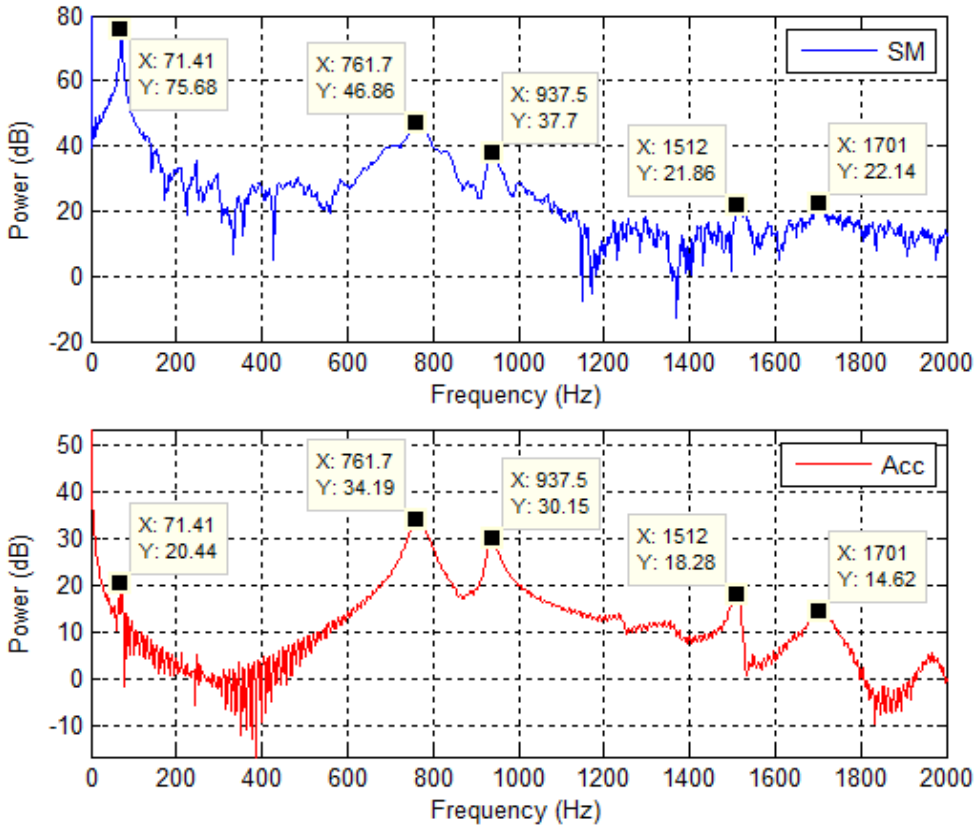

Figure IV.11. FFT of the vibration of the plate measured by the SM sensor and the accelerometer respectively. X represents the frequency in Hz and Y represents the power in dB

The Fast Fourier Transform (FFT) of these signals was plotted in Figure IV.11 that shows similarities between both FFTs where the resonance frequencies were determined by the SM sensor and by the accelerometer. However, the target may be not accessible in some cases in order to put the accelerometer where the advantage of non contact sensing. Moreover, the accelerometer has a weight of few grams that varies the measurement of the frequency by few Hertzs [77].

Another very important advantage of this type of sensors is their low cost and their simplicity which facilitates a lot their duplication allowing to have simultaneous measurements at different points which simplifies the reconstruction of the modal vector.

As mentioned earlier, a lot of differences resign between the theory of a rectangular clamped plate and the experiment conducted hereby. No relevant conclusions could be taken comparing both theoretical and experimental results.

However the experimental signals obtained by the SM sensor where validated by the counter-measurement conducted by the accelerometer.

An array of six sensors was created by duplicating the circuit used before the following figure shows the schematic of the experiment allowing the instantaneous multi-point modal analysis.

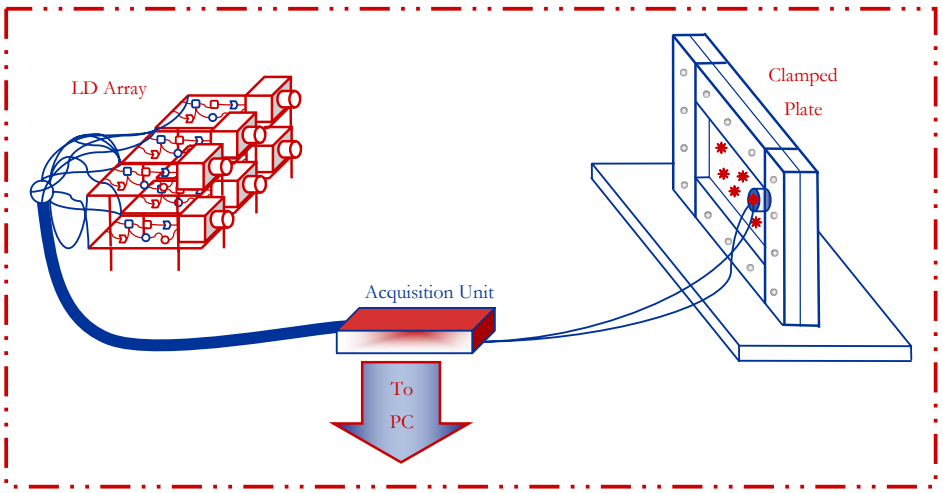

Figure IV.12. Schematic of the modal analysis of a clamped plate using an array of six lasers.

The laser array was used to accomplish simultaneous measurements at different points of the plate. Acquiring all the signals coming from those sensors and the accelerometer gives the FFT at 6 different points simultaneously (one of the lasers is always pointing on the accelerometer in order to provide the counter-measurement).

These FFTs were plotted in Figure IV.13 (first the six SM sensors and on a larger scale the accelerometer) which shows a similarity in all the resonance frequency knowing that differences comes essentially form the limitation of the numerical FFT algorithm. The difference in power levels comes from the fact that not all the points will vibrate with the same amplitude and from the statistical aspect of M_2 previously discussed. This last aspect can be omitted if a calibration measurement is accomplished.

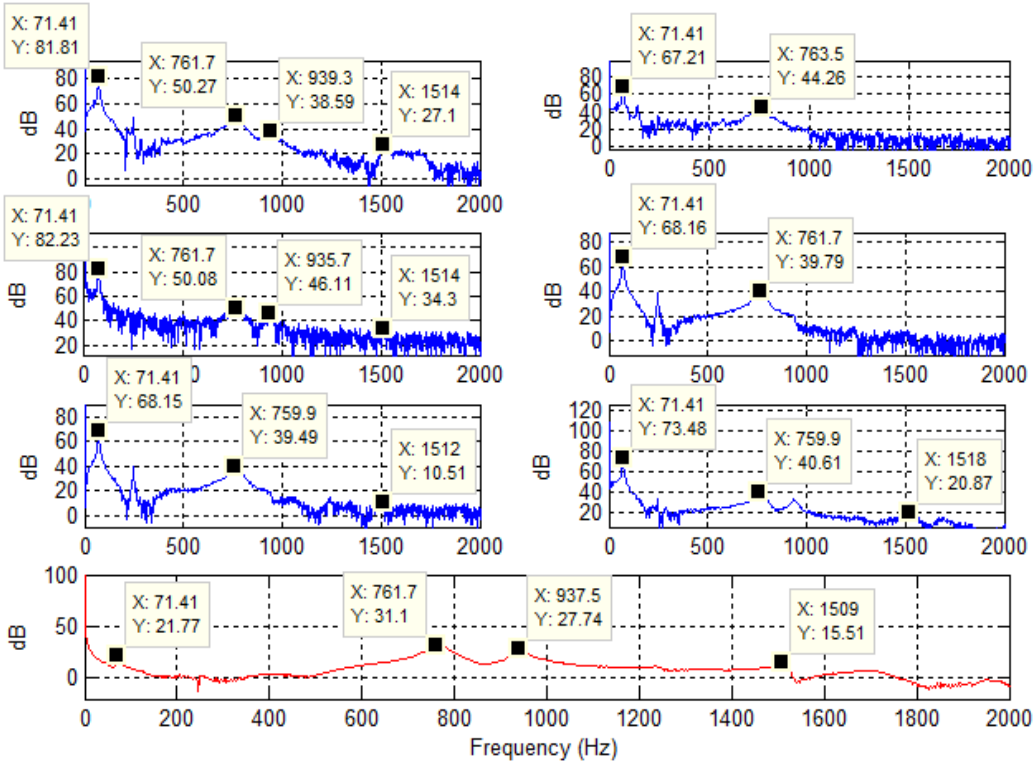

Figure IV.13. FFT of the six SM sensors and the accelerometer. X represents the frequency in Hz and Y the power in dB.

IV.6. Carbon Fiber Beam

The experiment conducted with the thin clamped plate was more of an academic modal analysis application accomplished just to validate the response of the tested sensor. Another type of applications having more industrial importance was the detection of impacts in Carbon Fiber Beams or CFBs. This experiment was conducted with the help of ISAE-SUPAERO who offered the tested CFBs.

The use of composite materials in structural components has increased during the recent years, by offering enormous potential and benefits to the aerospace industry and many other sectors. However composite materials are susceptible to delamination from a wide variety of sources which include fabrication stress, environmental cyclic loading, handling damage and foreign object impact damage [79][81]-[82]-[83]. Delamination may lead to the severe degradation of the mechanical behavior of structures due to loss of structural integrity. The detection of delamination and the study of their influences on the mechanical behavior of delaminated composite structures has become an important issue in the last years.

IV.6.1. One SM Sensor Tests

After studying the thin plate in the previous paragraph, the next structure to study is a carbon fiber beam (CFB). The CFB was mounted on a shaker that vibrates it vertically and the laser was installed on top of it with an accelerometer for counter-measurement. Another measurement of the force, applied at the middle of the CFB, was accomplished by the force sensor. The following figure shows the schematic of the first experiment conducted with only one laser. In all the experiments the shaker was excited by a white noise signal generated, by the acquisition unit, from a random sequence generated by the PC.

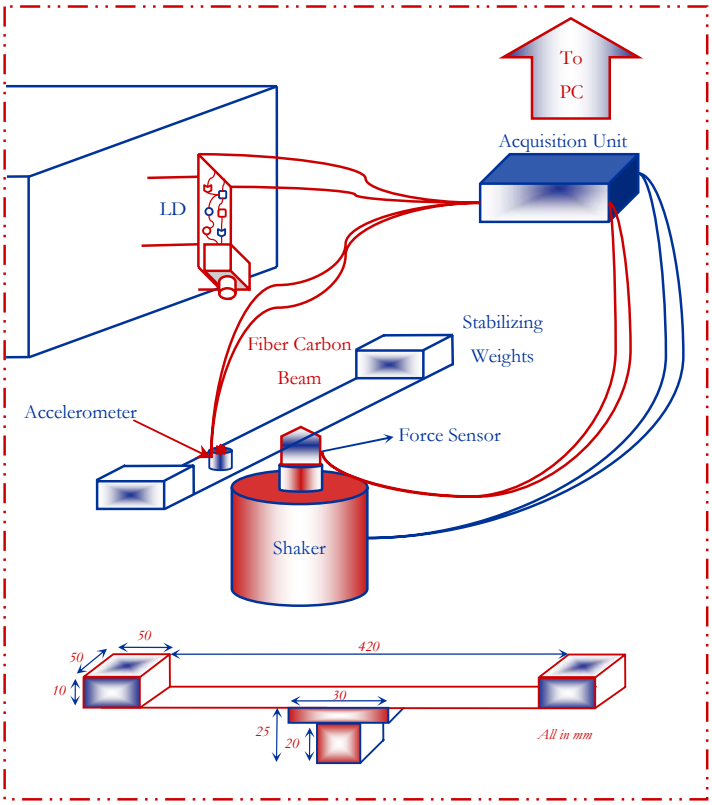

Figure IV.14. Schematic and dimensions of the CFB experiment.

This CFB was previously characterized using a Polytech vibrometer. Its resonance frequencies and principal modes of vibration are plotted in the following figure.

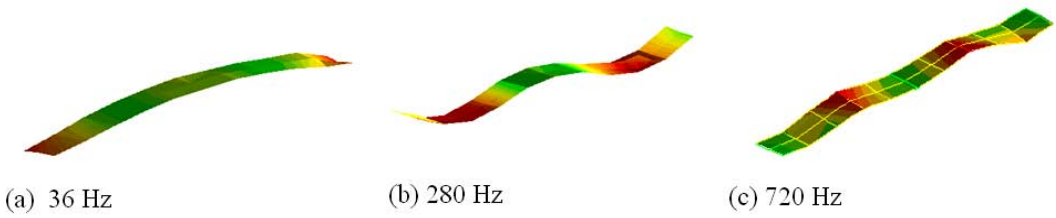

(a) 36 Hz (b) 280 Hz (c) 720 Hz

Figure IV.15. Vibration modes of the CFB.

On the other hand the FFTs of the three signals given by the force sensor (force), the accelerometer (acc) and the SM sensor (SM) were calculated and plotted in Figure IV.16 and Figure IV.17.

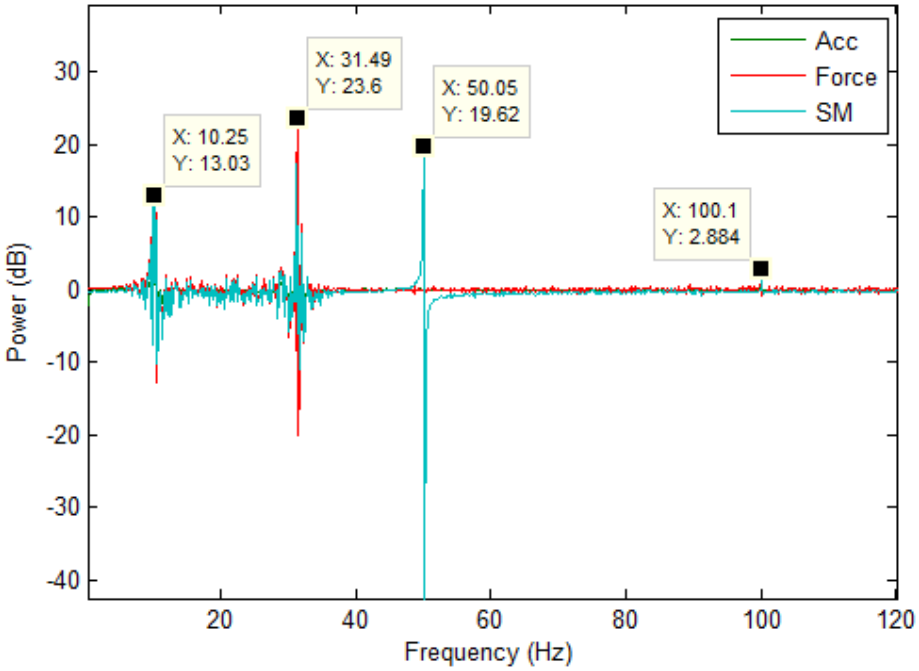

Figure IV.16. First zoom of the FFT of the three signals. X represents the frequency in Hz and Y the power in dB.

These FFTs showed a high similarity between all three sensors except for a noise peak in the SM signal caused by the alimentation noise at *50Hz*. Another parasite peak appeared in the signal of all the three sensors at *10 Hz* which may be caused by a vibration of the shaker itself caused by a bad fixation of this last. The other peak corresponds to the resonance frequencies of the first vibration modes at *31.49Hz*. The last peak at *100 Hz* is a harmonic frequency of the *50Hz* peak.

The second zoom, in Figure IV.17, shows another harmonic of the *50Hz* at *300Hz* approximately and another resonance frequency of the CFB at *282.2Hz*.

Furthermore the excitation signal sent to the shaker was also acquired and used in order to estimate the transfer function estimation (TFE) between each of

the different signals and this excitation signal. The result is plotted in Figure IV.18 showing the peaks of resonance detected earlier and the *50 Hz* peak and its harmonics.

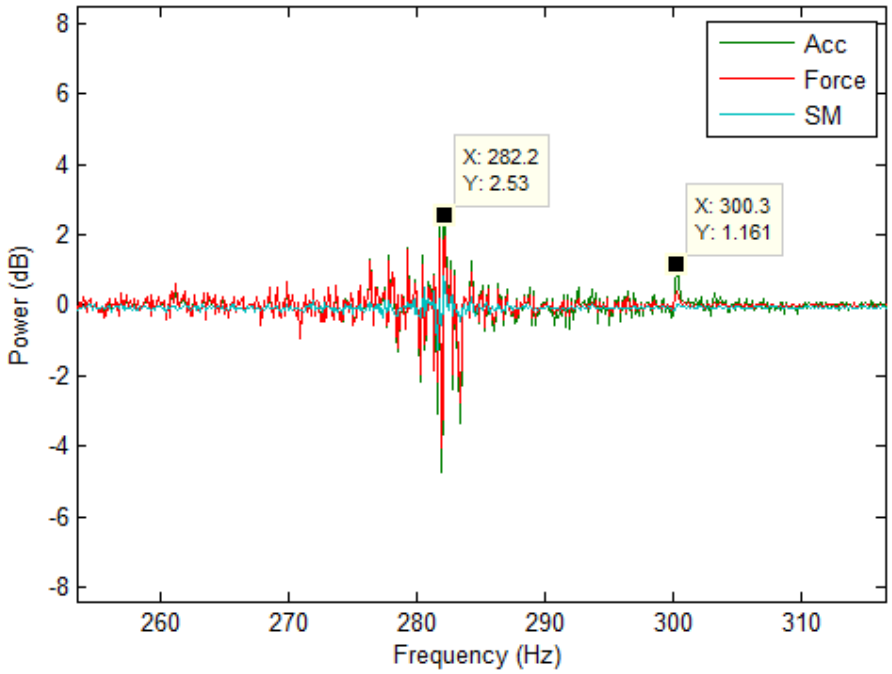

Figure IV.17. Second zoom of the FFT of the three signals. X represents the frequency in Hz and Y the power in dB.

Moreover, this TFE showed the third peak of resonance of the CFB corresponding to the third vibration mode (Figure IV.15). This peak was undetected in the case of the FFTs because of the noise level and because of the limitation of its numerical algorithm.

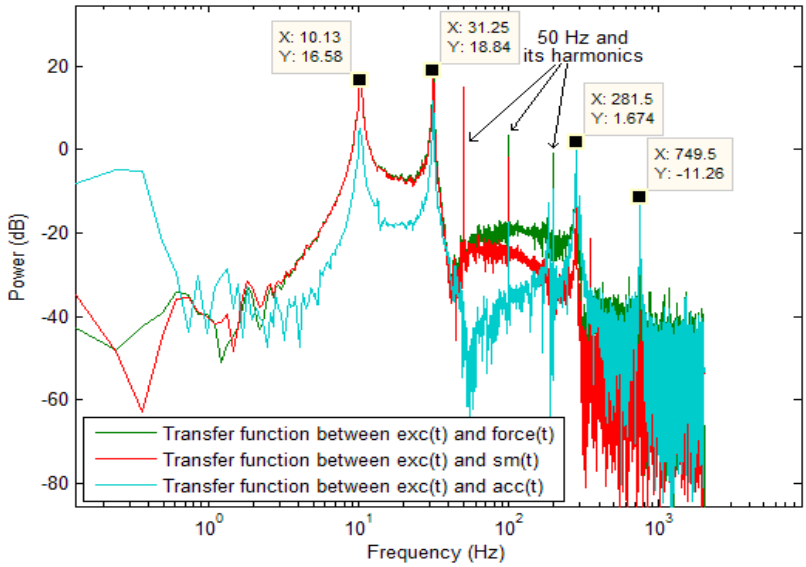

Figure IV.18. Transfer function between the white noise excitation signal and the different signals given by the accelerometer and both the force and SM sensors. X represents the frequency in Hz and Y the power in dB.

Furthermore a study of the power spectral densities of all the signals (Figure IV.19) shows the quality of the white noise generated and confirms all the results stated earlier from the FFT and the TFE methods.

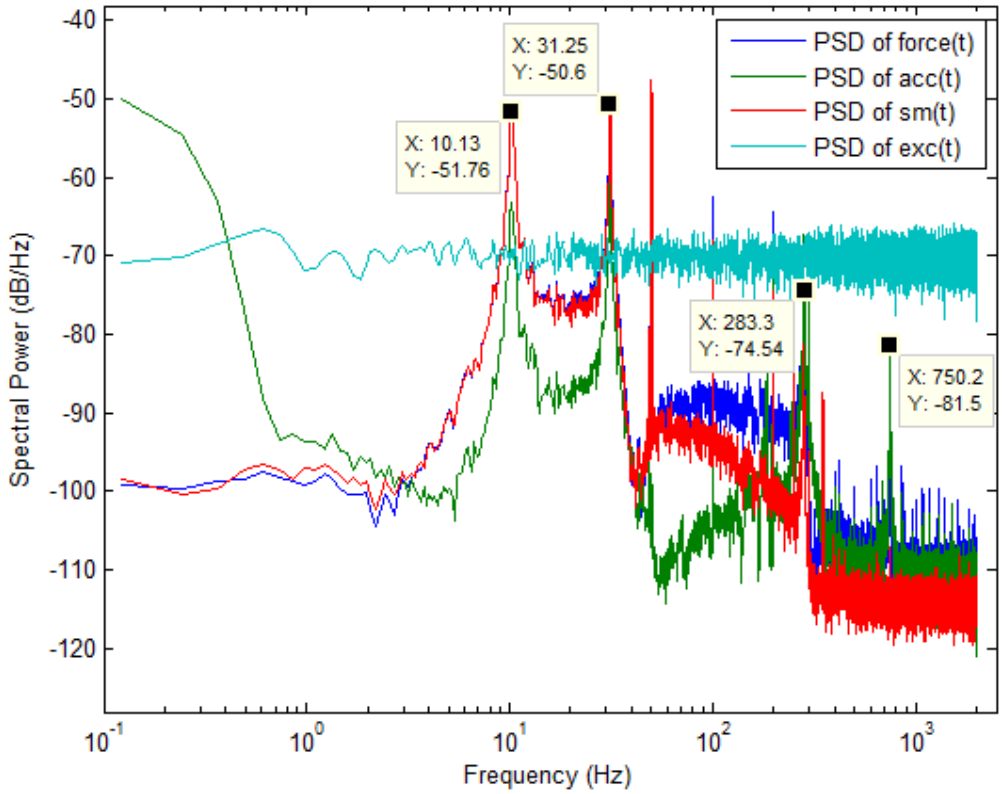

Figure IV.19. PSD of the white noise excitation signal and the different signals given by the accelerometer and both the force and SM sensors. X represents the frequency in Hz and Y the power in dB.

Before adding the other sensors to this experiment a test had to be done in order to confirm the repeatability of such a sensor despite the statistical aspect of M_2. Four different measurements were repeated while exciting always the shaker with a white noise signal without turning off the sensor. The FFTs of the SM signals were reported in Figure IV.20 and showed a correspondence in terms of both the resonance frequency peaks and the corresponding amplitude of vibration. These two parameters being vital in modal analysis in order to reconstruct the modal vector.

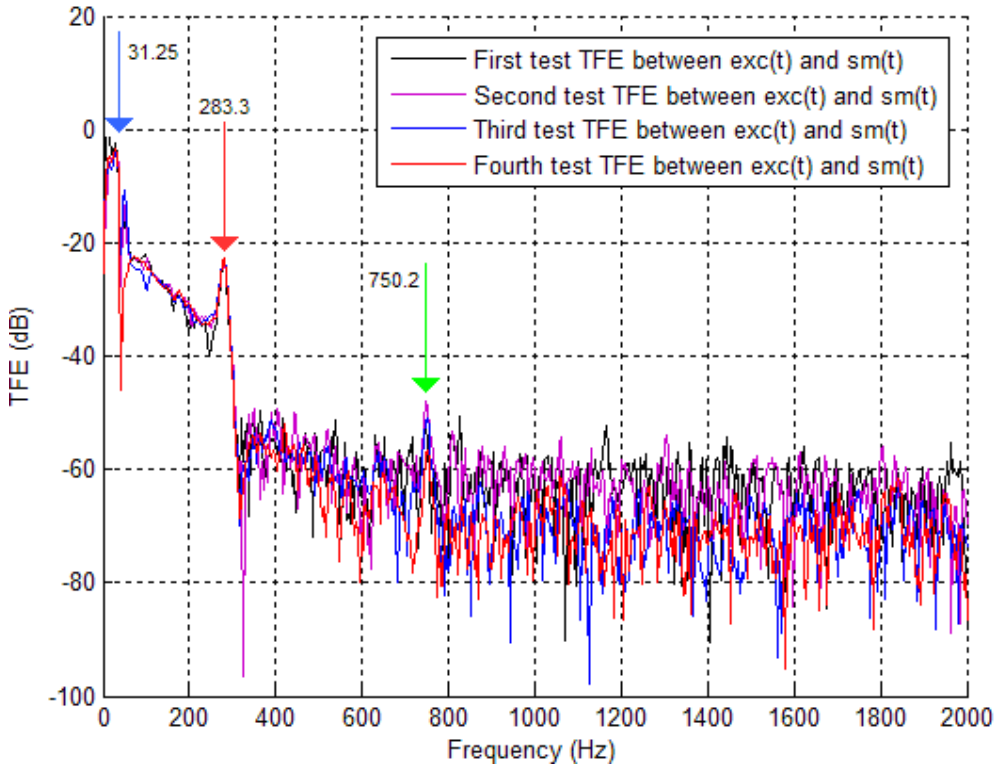

Figure IV.20. TFE between the SM signal and the excitation signal during four different repetitions.

IV.6.2. Two SM Sensors Tests

After making sure that one sensor is detecting the right peaks, another sensor was added to the experiment in order to show that two different lasers pointed at two different points will detect the same resonance frequencies but with different amplitude. However, this difference of amplitude may be induced by the statistical aspect of M_2 or also by the fact that those two points are not vibrating with the same amplitude but all this will not affect the detected frequency as shown in Figure IV.21.

It must be noted that this is not the same CFB tested in Figure IV.18 which explains the differences in the previously detected frequencies. Moreover, this CFB was damaged inducing a frequency shifting as reported earlier [77].

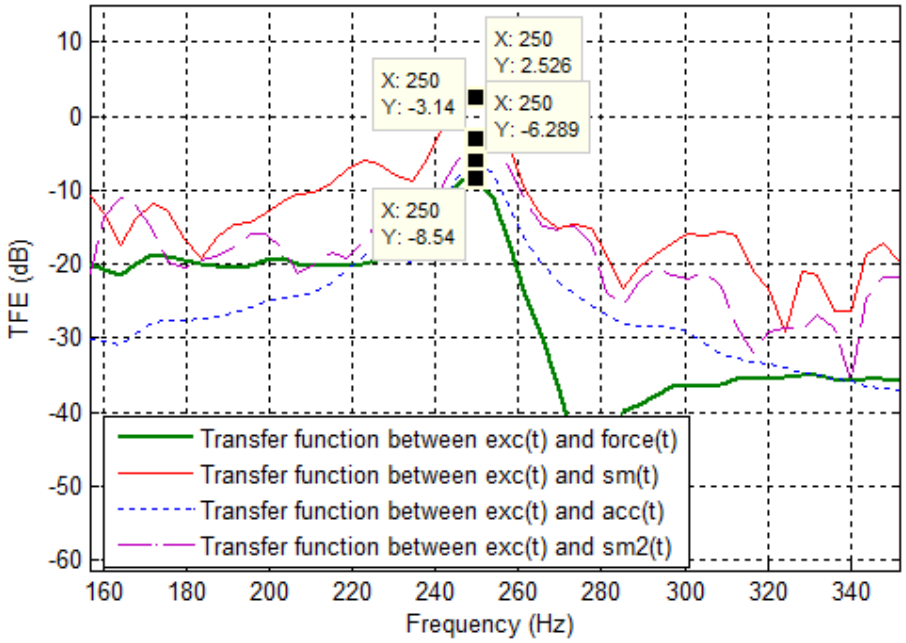

Figure IV.21. Zoom on one of the vibration modes detected by two SM sensors in addition to the accelerometer and the force sensor. X represents the frequency in Hz and Y the power in dB.

IV.6.3. Tests with an Array of Sensors

Figure IV.22 shows the schematic of the experiment involving an array consisting of six SM sensors pointing at different points of the CFB vibrated by the shaker still excited by a white noise signal. The counter-measurement is provided by both the accelerometer and the force sensor. Three different CFBs were tested in the case of this experiment: CFBs 16 and 17 were undamaged and CFB 11 was damaged. In the case of each CFB the experiment was repeated three times.

The effective aim of this study is to be able to identify if a CFB is damaged or not by using an array of SM sensors operated under strong feedback. For this purpose the two first undamaged CFBs will be studied first in order to evaluate the variances of the resonance frequency caused by fabrication differences and then to be compared to the differences with the damaged CFB.

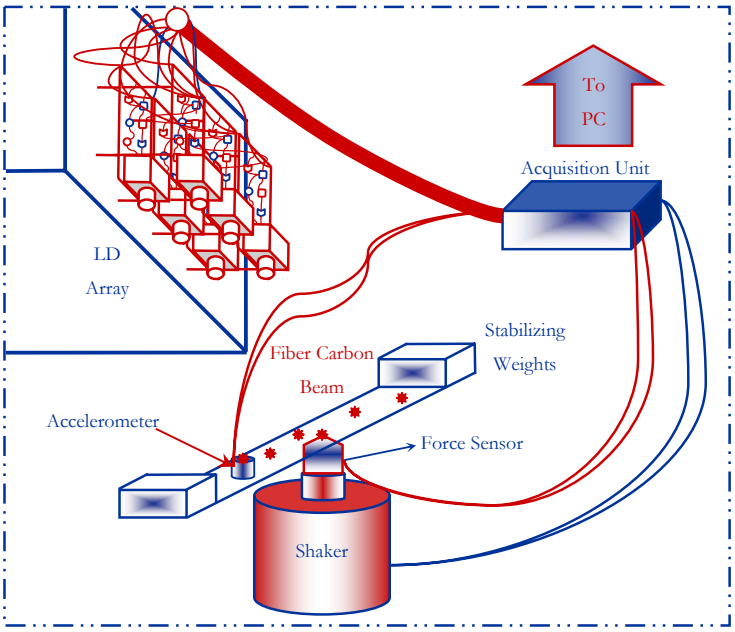

Figure IV.22. Schematic of the sensor's array experiments

IV.6.3.a. Modal Analysis of CFB 16

CFB number 16 was undamaged and was tested three consecutive times using all the six sensors; sensor 1 (*sm1(t)*) pointed on top of the accelerometer and sensor 6 (*sm6(t)*) pointed at the same point where the force was applied and measured by the force sensor.

Figure IV.23 shows the transfer function estimation between the excitation signal and each of the signals given by the force sensor, the accelerometer and the six SM sensors.

This figure represents one of the three tests accomplished whereas the Table IV.3 represents the detection of all the resonance frequencies corresponding to each of the three first modes for all three tests and their average values.

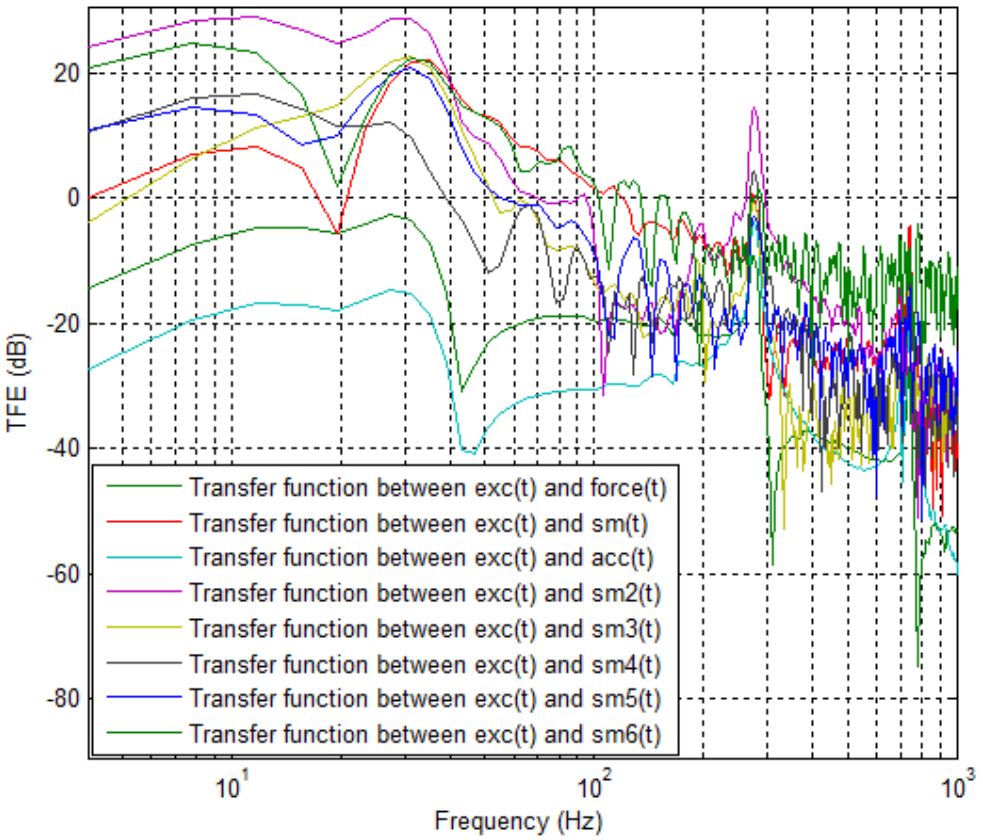

Figure IV.23. TFE for the force sensor, the accelerometer and the six SM sensors for the undamaged CFB 16.

CFB 16	*Mode 1 (Hz)*	*Mode 2 (Hz)*	*Mode 3 (Hz)*
Accelerometer	31.25	277.3	742.2
	31.25	277.3	742.2
	31.25	277.3	742.2
Force Sensor	31.25	277.3	742.2
	31.25	277.3	742.2
	31.25	277.3	742.2
SM1	31.25	277.3	742.2
	31.25	273.4	742.2
	31.25	277.3	742.2
SM2	31.25	277.3	742.2
	31.25	277.3	742.2
	31.25	277.3	742.2
SM3	31.25	277.3	742.2
	31.25	277.3	742.2
	31.25	277.3	742.2
SM4	31.25	277.3	742.2
	27.34	277.3	742.2

	31.25	273.4	742.2
SM5	31.25	277.3	750
	31.25	277.3	742.2
	35.16	277.3	742.2
SM6	31.25	277.3	742.2
	31.25	273.4	742.2
Average Frequency	***31.25***	***277.14***	***742.52***

Table IV.3. Frequency of each of the vibration modes detected by each of the sensors during three tests in the case of CFB 16.

It is to be noted that the variations encountered in some of the measurement may be due essentially to the numerical errors caused by the limitation of the TFE numerical algorithm.

IV.6.3.b. Modal Analysis of CFB 17

The experimental setup is the same as the one used for CFB 16, all the CFBs have the same dimensions and weights. This should theoretically mean that both CFBs should have the same modal vectors or same resonance frequencies. However CFB 17 has been studied in order to evaluate the variations of the resonance frequencies that may be caused by fabrication variances.

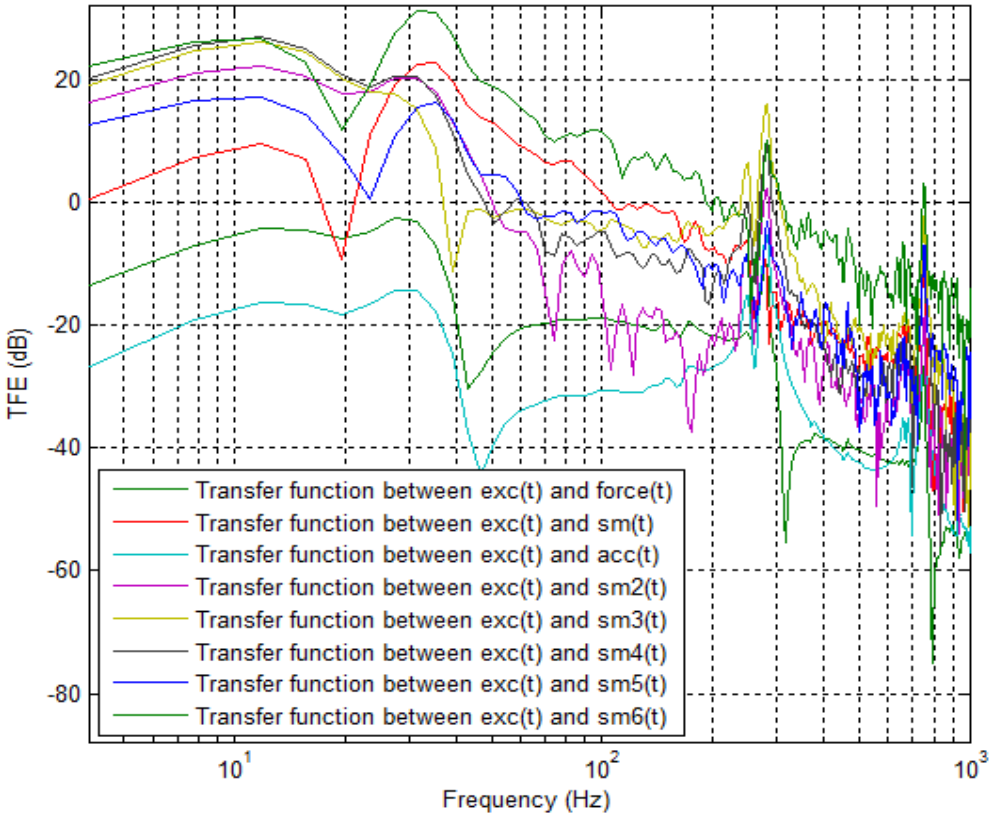

Figure IV.24. TFE for the force sensor, the accelerometer and the six SM sensors for the undamaged CFB 17.

Figure IV.24 shows also the TFE between the excitation signal and each of the signals coming from the different sensors and again Table IV.4 shows the frequencies corresponding to each of the first three vibration modes.

CFB 17	Mode 1 (Hz)	Mode 2 (Hz)	Mode 3 (Hz)
Accelerometer	31.25	281.3	750
	31.25	281.3	750
	31.25	281.3	750
Force Sensor	31.25	277.3	750
	31.25	277.3	750
	27.34	277.3	750
SM1	31.25	277.3	750
	31.25	277.3	750
	31.25	277.3	750
SM2	31.25	281.3	750
	31.25	281.3	753.9
	X	281.3	X
SM3	31.25	281.3	750
	31.25	281.3	750
	X	281.3	753.9
SM4	31.25	281.3	750
	27.34	281.3	750
	27.34	281.3	750
SM5	31.25	281.3	753.9
	31.25	281.3	753.9
	31.25	277.3	753.9
SM6	35.16	281.3	753.9
	31.25	281.3	750
	31.25	281.3	753.9
Average Frequency	30.89	279.97	751.19

Table IV.4. Frequency of each of the vibration modes detected by each of the sensors during three tests in the case of CFB 17.

Again the variations of the frequency of *3.9 Hz*, or a multiple of it, are caused purely by the limitation of the number of points used in the Matlab numerical algorithm. Although, if the frequency difference between the two different CFBs is calculated, it is of *0.36 Hz* for the first mode, *2.83 Hz* for the second mode and *8.67 Hz*.

IV.6.3.c. Modal Analysis of CFB 11

This CFB has been damaged in different points of its structure using the drop weight method illustrated in the following figure [84]-[85].

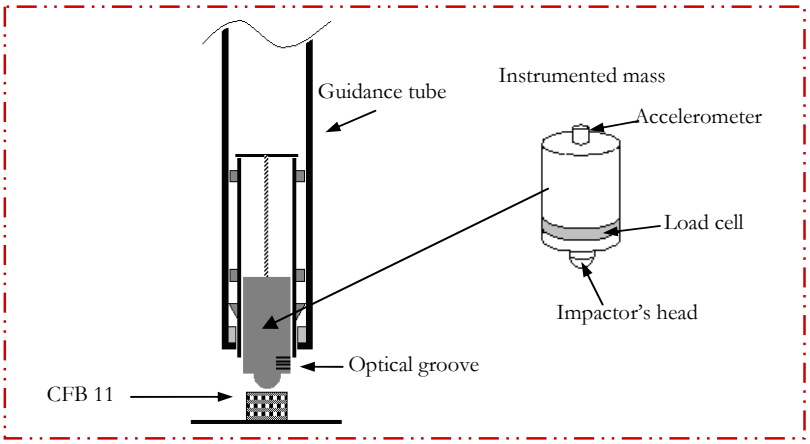

Figure IV.25. Drop weight method used to impact CFB 11.

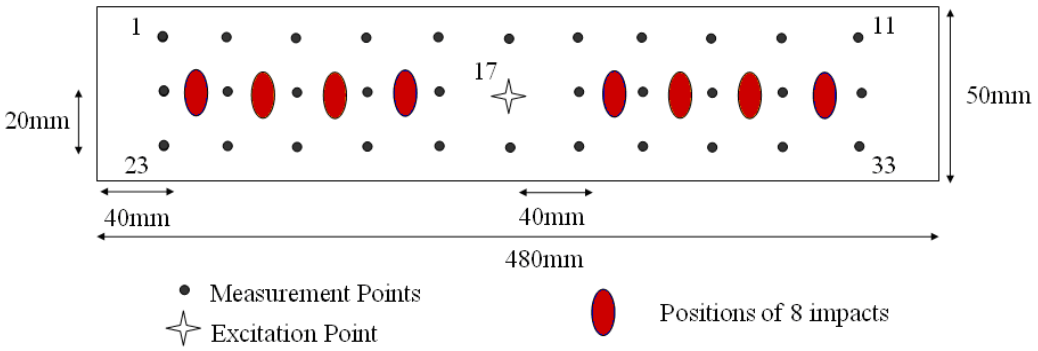

Figure IV.26. Positions of the impacts of CFB 11.

Figure IV.26 shows the positions of the impacted points of CFB 11. The objective of this study is to be able to distinguish impacted CFBs from non impacted ones.

Thereby, the FFT of the response of the different sensors will be studied in the case of CFB 11. Looking at these TFEs, shown in Figure IV.27, no differences can apparently be found with what was shown in Figure IV.23 and Figure IV.24.

However the frequencies of the vibrations modes are completely different from the case of CFBs 16 and 17 which can be seen in Figure IV.28.

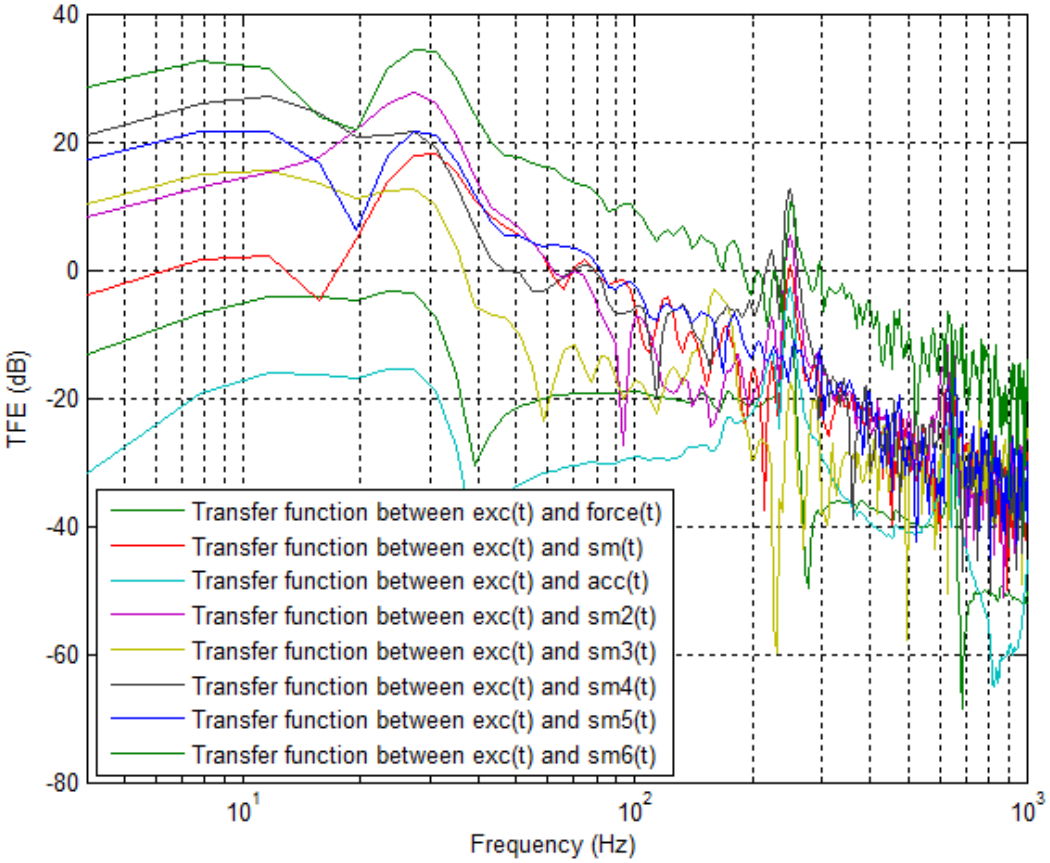

Figure IV.27. TFE for the force sensor, the accelerometer and the six SM sensors for the damaged CFB 11.

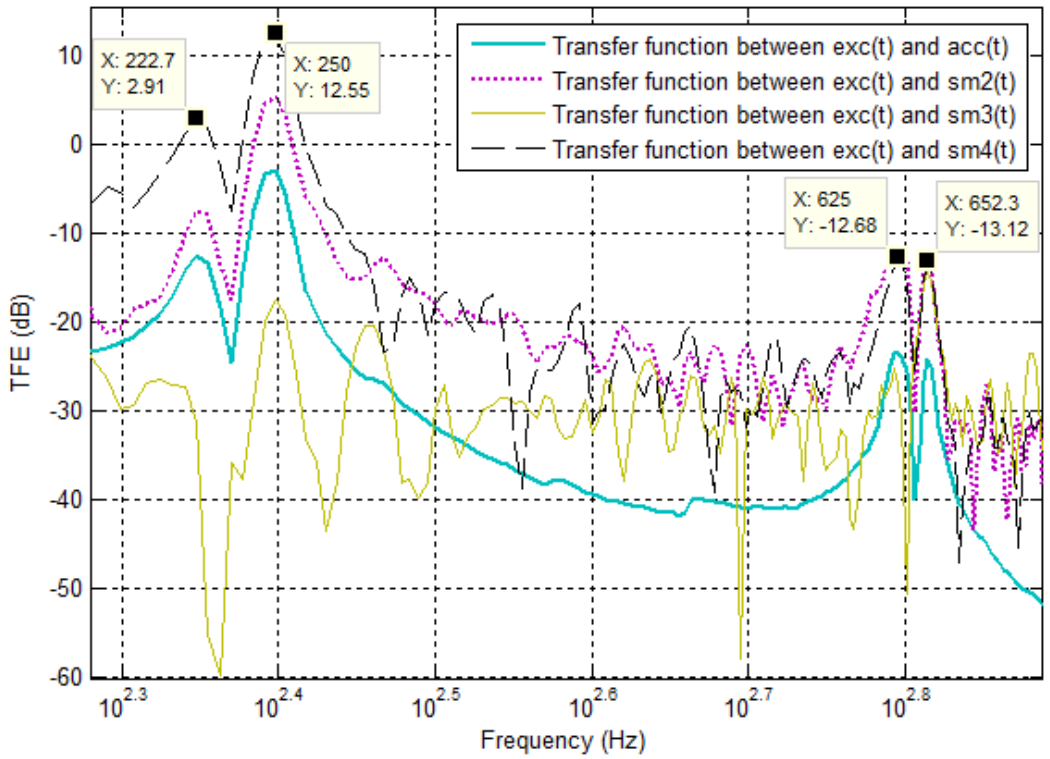

Figure IV.28. Zoom on the second and third vibrations modes in the TFE in the case of the accelerometer and two of the six SM sensors in the case of CFB 11. X represents the frequency in Hz and Y the power in dB.

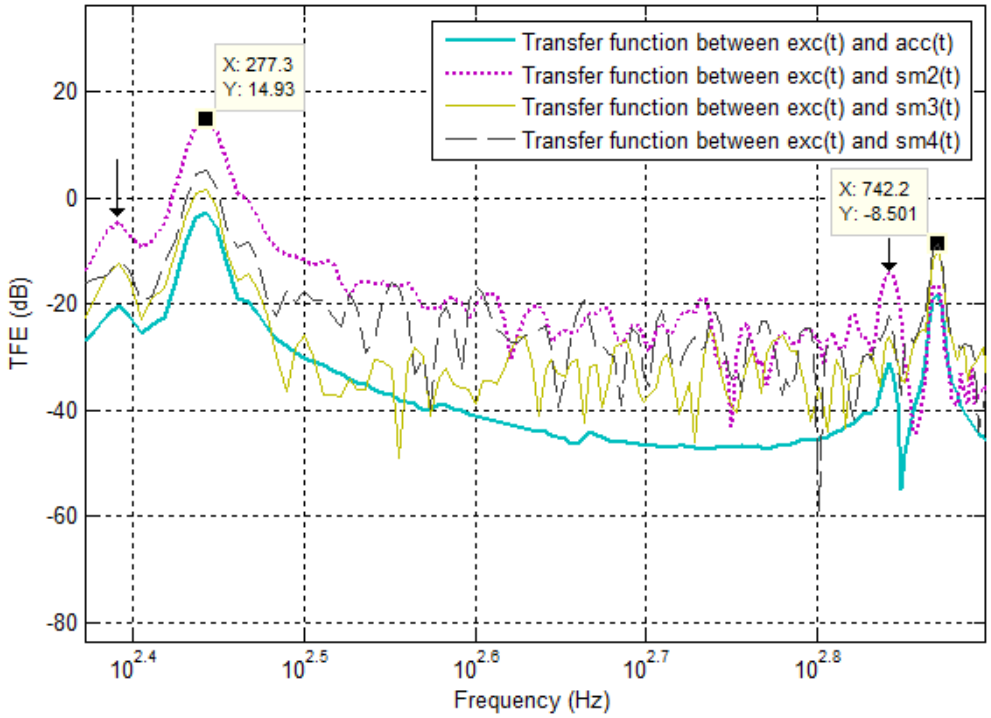

Figure IV.29. Zoom on the second and third vibrations modes in the TFE in the case of the accelerometer and two of the six SM sensors in the case of CFB 16.

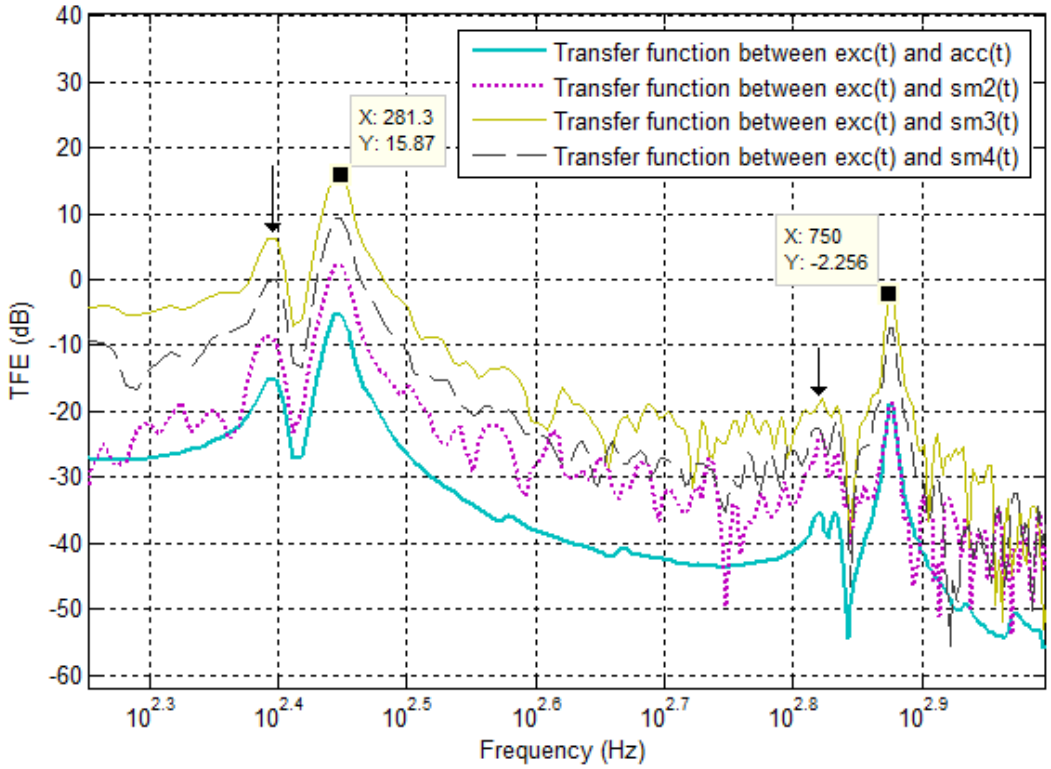

Figure IV.30. Zoom on the second and third vibrations modes in the TFE in the case of the accelerometer and two of the six SM sensors in the case of CFB 17. X represents the frequency in Hz and Y the power in dB.

CFB 11	Mode 1 (Hz)	Mode 2 (Hz)	Mode 2' (Hz)	Mode 3 (Hz)	Mode 3' (Hz)
Accelerometer	23.44	222.7	250	625	652.3
	23.44	222.7	250	625	652.3
	23.44	222.7	250	625	652.3
Force Sensor	23.44	X	246.1	X	652.3
	23.44	X	246.1	625	652.3
	23.44	X	246.1	X	652.3
SM1	31.25	222.7	250	621.1	652.3
	31.25	214.8	250	625	652.3
	31.25	222.7	246.1	625	656.3
SM2	27.34	222.7	250	628.9	652.3
	27.34	222.7	250	625	648.4
	27.34	222.7	250	X	X
SM3	27.34	X	250	621.1	652.3
	27.34	230.5	250	628.9	652.3
	X	X	X	625	652.3
SM4	27.34	222.7	250	625	652.3
	27.34	222.7	250	621.1	652.3
	X	222.7	250	625	652.3
SM5	27.34	X	X	632.8	656.3
	31.25	226.6	246.1	628.9	X
	31.25	222.7	246.1	X	644.5
SM6	27.34	226.6	250	632.8	656.3
	27.34	226.6	253.9	628.9	652.3
	31.25	222.7	253.9	X	648.4
Average Frequency	25.06	223.3	238.45	626.03	652.14

Table IV.5. Frequency of each of the vibration modes detected by each of the sensors during three tests in the case of CFB 11.

This table shows that the resonance frequencies have shifted a lot more significantly than in the case of comparison between CFBs 16 and 17. In fact, when considering mode 2 the difference is *53.84 Hz* if compared to CFB 16 and *56.67 Hz* if compared to CFB 17. The difference is even greater if the mode 3 is considered where comparing CFBs 11 and 16 leads to a difference of *125.16 Hz* and comparing CFBs 11 and 17 leads to *116.49 Hz*.

In conclusion, by comparing all the obtained results it can be seen that the resonance frequency corresponding to the first vibration mode is approximately unchanged for all the three CFBs. On the other hand, looking at the second and third vibration modes the frequency shifts between the different beams are noted in the following table (relatively to frequencies from Figure IV.15).

CFBs	Mode 2	Mode 3
16-17	1%	1.2%
11-16	19.2%	16.2%
11-17	20.2%	17.4%

Table IV.6. Frequency shift between the different CFBs for modes 2 and 3.

This table showed that the damage in a CFB can be detected when comparing the second and the third resonance frequencies where the difference revealed to be a lot more important than the one obtained when comparing two undamaged CFBs.

Finally it could be noticed that other vibration modes were detected by the SM sensors and by the accelerometer closely to the second and third vibration modes (pointed in Figure IV.28, Figure IV.29 and Figure IV.30). These modes were more accentuated in the case of a damaged beam. However no definitive mechanical cause was found and they may be caused by a vibration of the shaker or a mechanical coupling between the shaker and the CFB.

IV.7. Conclusion

In this chapter, an array of sensors using the self-mixing effect under strong feedback for modal analysis applications has been designed and tested.

This setup was used for modal analysis of a thin camped plate and showed that it provided a faithful image of the displacement. This proved to be very useful where it is possible to apply a white noise excitation and to have a whole frequency response from only one measurement.

This same setup was also used in order to characterize CFBs and proved to give good results when compared to a force sensor and an accelerometer.

Impact detection of CFBs was also achieved, first results showing that the resonance frequencies of a damaged CFB were significantly smaller than those of undamaged CFBs.

Further work has to be done in order to quantify the frequency shifts through simulations or theoretical studies and to find an explanation for the appearance of modes 2' and 3'. Moreover, an optimization of the number of the sensors has also to be done in order to be able to reconstruct modal vectors efficiently and to deduce the average vibration level (AVL [72]) .

General Conclusion and Future Works

During this PhD, we were able to show the phenomenon of loss of peaks in the self-mixing signals when operating in the moderate feedback regime and to study the effect of such a phenomenon on displacement measuring techniques.

The peak free signal was then introduced, named strong feedback regime, and studied in details in terms of relationships between the different parameters of the laser and this regime.

A relative displacement sensor was conceived for the first time in the strong feedback regime. This sensor was characterized in terms of precision, linearity and harmonic distortion.

This same sensor showed a lot of advantages for modal analysis applications providing a real time loyal image of the displacement without any complicated signal processing. This sensor was used for the modal analysis of a thin clamped plate and for impact detection in carbon fiber beams.

Even if this work comes as the prolongation of previous studies; extra work has still to be done in different domains concerning the self-mixing effect.

As a direct sequel of the present work, regarding the modal analysis application of the sensor under strong feedback, the number of sensors has to be optimized in order to be able to reconstruct the modal vector efficiently. Other improvements can be done concerning the bandwidth of response of this sensor or regarding the methods used to detect impact in CFBs.

Moreover, the behavioral model [57] we have used for all simulations is still based on the steady state equations. Current studies will enable us to ameliorate this model, taking the speckle effect into account, notably its influence on the value of C [86].

However using these steady-state equations may not be applicable anymore when studying high frequency displacements such as in the case of RF switches. In this case, a new approach of the self-mixing effect would then be investigated, based on the non linear dynamic behavior of the laser subject to feedback [56].

Finally, other studies were conducted in order to conceive displacement sensors working in given regimes. For example, extended Kalman filters were used for weak feedback where an unwrapping phase method was exploited for a laser subject to moderate feedback. The "ideal sensor" will be the one operating without the need of changing the signal processing algorithm. The particule filtering approach would be able to deduce the displacement in both operating regimes. However, as this not yet a real-time solution, another way to explore would be keeping the laser in a single operating regime by using adaptive optics.

References

[1]. H. W. Jentink, F. F. M. de Mul, H. E. Suihies, J. G. Aarnoudse and J. Greve, "Small laser Doppler velocimeter based on the self-mixing effect in a diode laser," *Applied Optics*, Vol. 27, pp. 379-385, 1988.

[2]. T. Bosch, C. Bes, L. Scalise, G. Plantier, "Optical Feedback Interferometry", *Encyclopedia of Sensors*, vol. 7, pp 107-126, 2006, American Scientific Publishers, USA.

[3]. P. G. R. King and G. J. Steward, "Metrology with an optical maser," *New Scientist*, 1963.

[4]. M. J. Rudd, "A laser Doppler velocimeter employing the laser as a mixer-oscillator", *J. Hys. E: Sci. Instrum. 1*, 723-736, 1968.

[5]. S. K. Ozdemir, S. Ito, S. Shinohara, H. Yoshida, and M. Sumi, "Correlation-based speckle velocimeter with self-mixing interference in a semiconductor laser diode," *Applied Optics*, Vol. 38, pp. 6859-6865, 1999.

[6]. S. Donati, G. Giuliani and S. Merlo, "Laser diode feedback interferometer for measurement of displacements without ambiguity", *IEEE J. Quantum Electron.*, Vol. 31, pp. 113-119, 1995.

[7]. F. Gouaux, N. Servagent, and T. Bosch, "Absolute distance measurement with an optical feedback interferometer," *Applied Optics*, Vol. 37, pp. 6684-6689, 1998.

[8]. G Mourat, N Servagent and T Bosch, "Distance measurement using the self-mixing effect in a three-electrode distributed Bragg reflector laser diode," *Optical Engineering*, Vol. 39, pp. 738-743, 2000.

[9]. P J de Groot, G M Gallatin and S H Macomber, "Ranging and velocimetry signal generation in a backscatter-modulated laser diode," *Applied Optics*, Vol. 27, pp. 4475-4480, 1988.

[10]. E Gagnon and J-F Rivest, "Laser range imaging using the self-mixing effect in a laser diode," *IEEE Transactions on Instrumentation and Measurement*, Vol. 48, pp. 693-699, 1999.

[11]. http://www.business-sites.philips.com/lasersensors/about/article-15372.html

[12]. L. Y. Leng, J. R. Tucker, A. D. Rakic, "Distance Measurement using the Change in Junction Voltage Across a Laser Diode due to the Self-Mixing Effect", *Northern Optics*, pp. 73-77, 2006.

[13]. W. Mao, and S. Zhang, "Analysis of the effects of feedback asymmetry in external cavity He-Ne lasers," *Applied Optics*, Vol. 45, Issue 29, pp. 7723-7728, 2006.

[14]. L. Kervevan, H. Gilles, S. Girard and M. Laroche, "Two-dimensional velocity measurements With self-mixing technique in diode-pumped Yb:Er glass laser," *IEEE Photonics Technology Letters,* Vol. 16, Issue: 7, pp. 1709-1711, 2004.

[15]. L. Rovati, F. Docchio, "Low-coherence interferometry using a self-mixing super-luminescent diode," *IEEE Photonics Technology Letters*, Vol. 10, pp.123-125, 1998.

[16]. L. Rovati, F. Docchio, "Self-mixing super-luminescent diode optical tomography," *Proceedings of SPIE 18th Congress on the International Commission for Optics*, Vol. 3749, pp.790, 1999.

[17]. K. Petermann, "External optical feedback phenomena in semiconductor lasers," *IEEE J. Sel. Topics Quantum Electron.*, Vol. 1, N°. 2, pp. 480-489, 1995.

[18]. G. Acket, D. Lenstra, A. D. Boef, and B. Verbeek, "The influence of feedback intensity on longitudinal mode properties and optical noise in index-guided semiconductor lasers," *IEEE Journal of Quantum Electronics*, Vol. 20, pp. 1163-1169, 1984.

[19]. G. Giuliani, S. Bozzi-Pietra and S. Donati, "Self-mixing laser diode vibrometer", *Meas. Sci. Technol. 14*, pp. 24-32, 2003.

[20]. L. Golderg, H. F. Taylor, A. Dandridge, J. F. Weller, and R. O. Miles, "Spectral Characteristics of Semiconductor Lasers with Optical Feedback", *IEEE J. Quantum Electron*, Vol. QE-18, pp. 555-564, 1982.

[21]. G. Mourat, "Etude de diodes laser pour des applications métrologique de la rétro-injection optique ", *PHD INPT*; N°: 1561, 2006.

[22]. W. M. Wang, K. T. V. Grattan, A. W. Palmer, and W. J. O. Boyle, "Self-mixing interference inside a single-mode diode laser for optical sensing applications," *IEEE, Journal of Lightwave Technology*, Vol. 12, N°. 9, pp. 1577-1587, 1994.

[23]. C.Bes, " Conception d'un système laser de mesures de déplacements par interférométrie à rétro-injection optique dans le cas de feedbacks faible et modéré ", *PHD INPT*, N°. 2382, 2006.

[24]. T. Bosch, "An overview of self-mixing applications", *IEEE COMMAD04 invited paper*, 2004.

[25]. G. Giuliani, M. Norgia, S. Donati and T. Bosch, "Laser diode self-mixing technique for sensing applications", *Journal of Optics A: Pure and Applied Optics*, pp. 283-294, 2002.

[26]. S. Donati, "Laser interferometry by induced modulation of the cavity field", *Journal of Applied Physics*, Vol. 49, pp. 495-497, 1978.

[27]. S. Shinoara, A. Mochizuki, H. Yoshida and M. Sumi, "Laser Doppler velocimeter using the self-mixing effect of a semiconductor laser diode", *Applied Optics*, Vol. 25, pp. 1417-1419, 1986.

[28]. Beheim G. and Fritsch K., "Range finding using frequency modulated laser diode, *Applied Opt*ics, Vol. 25, pp. 1439-1442, 1986.

[29]. J. G. Webster, "The Measurement, Instrumentation and Sensors Handbook," *CRC Press*, p. 29, 1998.

[30]. C. BES, G. PLANTIER and T. BOSCH, "Displacement Measurements Using a Self-mixing Laser Diode Under Moderate Feedback", *IEEE Trans. on Instrumentation and Measurement*, Vol. 55, N°. 4, pp. 1101-1105, 2006.

[31]. C. Bes, V. Belloeil, G. Plantier, Y. Gourinat and T. Bosch, "A self-mixing laser sensor design with an extended Kalman filter for optimal online structure analysis and damping evaluation", *IEEE/ASME Trans. on Mechatronics*, Vol. 12, N°. 3, pp. 387-394, 2007.

[32]. A. DONCESCU, C. BES and T. BOSCH, "Displacement Estimation with an Optical Feedback Interferometer Using an Evolutionary Algorithm", *Proceedings of IEEE Sensors 2007*, Atlanta, 2007.

[33]. J. C. Dainty, "Laser Speckle and Related Phenomena," *Springer Berlin*, 1975.

[34]. S. Donati and G. Martin, "Speckle-pattern intensity and phase second-order conditional statistics," *J. Opt. Soc. Amer.*, Vol. 69, pp. 1690-1694, 1979.

[35]. M. Norgia, S. Donati, and D. D'Alessandro, "Interferometric measurements of displacement on a diffusing target by a speckle tracking technique," *IEEE J. Quant. Electron.*, Vol. 37, pp. 800-806, 2001.

[36]. V. Annovazzi-Lodi, S. Merlo, and M. Norgia, "Measurement on a micromachined silicon gyroscope by feedback interferometry," *IEEE/ASME Trans. on Mechatronics*, Vol. 6, pp. 1-6, 2001.

[37]. V. Annovazzi-Lodi, S. Merlo, and M. Norgia, "Characterization of silicon microstructures by feedback interferometry", *Journal of Optics A: Pure and Applied Optics*, Vol. 4, pp. 311-317, 2002.

[38]. S. Donati, M. Norgia: "A Hybrid Opto-Mechanical Gyroscope with an Injection-Interferometer Readout", *Electronics Letters* , Vol. 37, No. 12, pp. 756-758, 2001.

[39]. W. M. Wang, W. J. O. Boyle, K. T. V. Grattan, and A. W. Palmer, "Self-mixing interference in a diode laser: Experimental observations and theoretical analysis," *Applied Optics*, Vol. 32, No. 9, pp. 1551-1558, 1993.

[40]. P. A. Roos, M. Stephens, and C. E. Wieman, "Laser vibrometer based on optical-feedback induced frequency modulation of a single-mode laser diode", *Applied Optics*, Vol. 35, pp. 6754-6761, 1996.

[41]. G. Giuliani, S. Bozzi-Pietra, and S. Donati, "Self-mixing laser diode vibrometer," *Measurement Science and Technology*, Vol. 14, pp. 24-32, 2003.

[42]. L. Scalise, Y. Yu, G. Giuliani, G. Plantier, and T. Bosch, "Self-mixing laser diode velocimetry: application to vibration and velocity measurement," *IEEE Transactions on Instrumentation and Measurement*, Vol. 53, pp. 223-232, 2004.

[43]. R. J. Adrian, "Selected Papers on Laser Doppler Velocimetry," *SPIE*, Bellingham, 1993.

[44]. X. Raoul, T. Bosch, G. Plantier and N. Servagent, "A double-laser diode onboard sensor for velocity measurement," *IEEE Transactions on Instrumentation and Measurement*, Vol. 53, pp. 95-101, 2004.

[45]. J. H. Churnside, "Laser doppler velocimetry by modulating a CO_2 laser with backscattered light," *Applied Optics*, Vol. 23, pp. 61-66, 1984.

[46]. S. Shinohara, A. Mochizuki, H. Yoshida, and M. Sumi, "Laser doppler velocimeter using the self-mixing effect of a semiconductor laser diode," *Applied Optics*, Vol. 25, pp. 1417-1419, 1986.

[47]. J. Albert, M. C. Soriano, I. Veretennico, K. Panajotov, J. Danckaert, P. A. Porta, D. P. Curtin, and J. G. McInerney, "Laser doppler velocimetry with polarization-bistable VCSELs," *IEEE Journal Of Selected Topics In Quantum Electronics*, Vol. 10, pp. 1006-1012, 2004.

[48]. G. Plantier, N. Servagent, A. Sourice, and T. Bosch, "Real-time parametric estimation of velocity using optical feedback interferometry," *IEEE Transactions on Instrumentation and Measurement*, Vol. 50, pp. 915-919, 2001.

[49]. F. F. M. de Mul, L. Scalise, A. L. Petoukhova, M. Van Herwijnen, P. Moes, and W. Steenbergen, "Glass-fiber self-mixing intra-arterial laser doppler velocimetry: Signal stability and feedback analysis," *Applied Optics*, Vol. 41, pp. 658-667, 2002.

[50]. M. H. Koelink, M. Slot, F. F. M. de Mul, J. Greve, R. Graa_, A. C. M. Dassel, and J. G. Aarnoudse, "Laser doppler velocimeter based on the self-mixing effect in a fiber-coupled semiconductor laser : theory," *Applied Optics*, Vol. 31, pp. 3401-3408, 1992.

[51]. S. K. Ozdemir, S. Takamiya, S. Ito, S. Shinohara, and H. Yoshida, "Self-mixing laser speckle velocimeter for blood flow measurement," *IEEE Transactions on Instrumentation and Measurement*, Vol. 49, pp. 1029-1035, 2000.

[52]. A. Courteville, T. Gharbi, and J. Y. Cornu, "Noncontact mmg sensor based on the optical feedback effect in a laser diode," *Journal of Biomedical Optics*, Vol. 3, pp. 281-285, 1998.

[53]. G. Beheim and K. Fritsch, "Range finding using frequency-modulated laser diode," *Applied Optics*, Vol. 25, pp. 1439-1035, 1986.

[54]. http://newtonperipherals.com/MoGo_press_philips.html

[55]. http://optics.org/cws/article/research/9217

[56]. D.M. Kane and K.A. Shore editors, "Unlocking dynamical diversity: optical feedback effects on semiconductor lasers", Chapter 7, pp 217-256, Wiley, 2005.

[57]. G. Plantier, C. Bes, and T. Bosch, "Behavioral model of a self-mixing laser diode sensor," *IEEE Journal of Quantum Electronics*, Vol. 41, pp. 1157-1167, 2005.

[58]. Y. Yanguang, G. Giuliani, and S. Donati, "Measurement of the linewidth enhancement factor of semiconductor lasers based on the optical feedback self-mixing effect," *IEEE Photonics Technology Letters*, Vol. 16, N°. 4, pp. 990-992, 2004.

[59]. C. Bes, G. Plantier, and T. Bosch, "Displacement measurements using a self-mixing laser diode under moderate feedback", *IEEE Transaction Instrumentation and Measurement*, Vol. 55, Issue 4, pp. 1101-1105, August 2006.

[60]. L. Goldberg, H. Taylor, A. Dandridge, J. Weller, and R. Miles, "Spectral Characteristics of Semiconductor lasers with optical feedback," *Journal of Quantum Electronics*, Vol. 18, p. 555, 1982.

[61]. C. Henry and R. Kazarinov, "Instability of semiconductor lasers due to optical feedback from distant reflectors," *Journal of Quantum Electronics*, Vol. 22, N° 2, p. 294, 1986.

[62]. J. O. Binder and G. D. Cormack, "Mode Selection and Stability of Laser with Weak Optical a Semiconductor Feedback," *Journal of Quantum Electronics*, Vol. 25, pp. 2255-2259, 1989.

[63]. Mork J. and Tromborg B., "Stability analysis and the route to chaos for laser diodes withoptical feedback," Photonics Technology Letters, Vol. 2, N°. 8, pp. 549-552, 1990.

[64]. Lenstra D., "Statistical theory of the multistable external-feedback laser," *Optics Communications*, Vol. 81, N°. 3-4, pp. 209-214.

[65]. Addy R.C., Palmer A.W., Thomas K. and Grattan V. "Effects of external reflector alignment in sensing applications of optical feedback in laser diodes," *Journal of Lightwave Technology*, Vol. 14, N°. 12, pp. 2672-2676.

[66]. X. Raoul, T. Bosch, G. Plantier and N. Servagent, "A double-laser diode onboard sensor for velocity measurements", *IEEE Transactions on Instrumentation and Measurement*, Vol. 55, N°. 1, pp. 95-101, 2004

[67]. G. Giuliani, S. Bozzi-Pietra and S. Donati, "Self-mixing laser diode vibrometer", *Meas. Sci. Technol.* 14, pp 24-32, 2003.

[68]. G.A. Acket, "The influence of feedback intensity on longitudinal mode properties and optical noise in index-guided semiconductor lasers", *IEEE Journal of Quantum Electronics*, Vol. 20, pp 1163-1169, 1984.

[69]. Norgia M., Donati S., "A displacement-measuring instrument utilizing self-mixing interferometry," *IEEE Transactions on Instrumentation and Measurements*, Vol. 52, N°. 6, pp. 1765-1770, 2003.

[70]. C. Bes, T. Bosch, G. Plantier and F. Bony, "Characterisation of a self-mixing displacement sensor under moderate feedback", *Optical Engineering*, Vol. 45, N°. 8, pp 084402-1-084402-6, 2006.

[71]. J. El Assad, G. Plantier, and T. Bosch, "Laser diode under strong feedback for mechatronic applications", *IEEE Sensors 2007 conference*, Atlanta, USA, 2007.

[72]. C. BES, V. BELLOEIL, G. PLANTIER, Y. GOURINAT, T. BOSCH, "A self-mixing laser sensor design with an extended Kalman filter for optimal online structure analysis and damping evaluation," *IEEE/ASME Transaction on Mechatronics*, Vol. 12, N°. 3, pp. 387-394, 2007.

[73]. G. GIULIANI, S. DONATI, M. PASSERINI and T. BOSCH, "Angle measurement by injection detection in a laser diode", *Optical Engineering*, Vol. 40, N°. 1, pp. 95-99, 2001.

[74]. R. LANG and K. KOBAYASHI, "External optical feedback effects on semiconductor injection laser properties", *IEEE Journal of Quantum Electronics*, Vol. QE-16, N°. 3, pp. 347-355, 1980.

[75]. P.D. WELCH, "The use of Fast Fourier Transform for the estimation of power spectra: a method based on time averaging over short, modified periodograms," *IEEE Transactions on Audio Electroacoustics*, Vol. AU-125, pp.70-73, 1967.

[76]. J. EL-ASSAD, T. BOSCH and G. PLANTIER, "Analysis of a Self-Mixing Signal for Displacement Measurements using a Laser Diode under Moderate Feedback", *in revision at Applied Optics*.

[77]. N. SERVAGENT, T. BOSCH and M. LESCURE, "A laser displacement sensor using the self-mixing effect for modal analysis and defect detection". *IEEE Instrumentation and Measurement*, Vol. 46, N°.4, pp. 847-850, 1997.

[78]. J EL. Assad, T. Bosch, G. Plantier, "Real Time Modal Analysis Using a Strong Feedback Self-mixing Sensor," *Proceedings of Advanced Laser Technologies (ALT'07)*, 2007.

[79]. D.J. Ewins, "Modal Testing: Theory and Practice," Brüel and Kjær, 1986.

[80]. R.D. Blevins, "Formulas for natural frequency and mode shapes," Van Nostrand Reinhold Co., 1979.

[81]. S.W. Tsai and H.T. Hann, "Introduction to composite materials", *Technic Publishing Company*, Westposrt, Connecticut, 1980.

[82]. V.C. Li, T. Kanda and Z. Lin, "Influence of Fiber/Array interface properties on complementary energy and composite damage tolerance," *Key Engineering Materials*, pp. 145-465, 1998.

[83]. R.M. Gadelrab, "The effect of delamination on the natural frequencies of a laminated composite CFB," *Journal of Sound and Vibration*, pp. 283-292, 1996.

[84]. S. Abrate, "Impact on composite structures," *Cambridge University Press*, 1998.

[85]. E. Abi Abdallah, S. Rivallant, C. Bouvet, J.J. Barrau, J.M. Buchin, "The influence of composite tubes damage tolerance on compressive residual strength: experimental observations," *AI4IA first international conference*, pp. 19-25, 2007.

[86]. R.H. Hage, G. Plantier, T. Bosch and A. Sourice, "Modeling and Analysis of Speckle Effects for Velocity Measurements with Self-Mixing Laser Diode Sensors," *accepted for 7th IEEE Conference on Sensors 2008*.

Abstract

Lasers have been widely used in different types of applications such as telecommunications, CD/DVD readers or for sensing purposes. A major drawback in their use is the optical feedback caused by an obstacle in their direction of propagation. This light reinjected in the active area modifies the emission properties of laser diodes and obliges the developers to consider adding isolators increasing thereby the complexity and the price of such systems.

However this optical feedback induces a variation in the emission power and frequency in function with the distance to the reflector. This phenomenon, more commonly known as self-mixing, is used in different types of displacement, velocity and vibration sensors.

In this work, the physical theory of the self-mixing effect is introduced and then a state of the art of its main applications in the different fields of instrumentation is accomplished.

A detailed study of the self-mixing signal in the moderate feedback regime is achieved introducing the effect of "loss of peaks", its physical interpretation, mechanisms and effect on different types of displacement measurement.

Afterwards, the discrepancy concerning the strong feedback regime was cleared out showing that it may be used for relative displacement measurement. A detailed study of this regime covers its statistical aspect and the influence of different parameters on this aspect.

Finally, the self-mixing sensor under strong feedback was introduced in modal analysis applications after being characterized. It was applied to study a clamped plate or to detect damage in carbon fiber CFBs. This type of sensors proved its major advantage of simplicity providing a direct image of the displacement without the need of any advanced signal processing. This facilitates its duplication where an array of sensors was used in different experiments.

Key Words: Self-mixing - Optical Feedback Interferometry- Long External Cavity- Relative Displacement Measurement - Modal Analysis.

Résumé

L'utilisation des lasers est répandue dans le domaine de l'instrumentation. Cependant, le fonctionnement de tels dispositifs peut être perturbé par le phénomène de rétro-injection optique (ou self-mixing) auquel est soumis la diode laser. Cette sensibilité du laser à la rétro-injection optique offre de nombreux avantages, notamment pour la mesure de déplacements, de vitesse ou de distance.

Dans ce travail, nous introduisons le phénomène de self-mixing avant d'effectuer un état de l'art des différentes applications de ce type de capteurs.

Le régime de fonctionnement de rétro-injection optique modérée est d'abord étudié en détails en introduisant la notion de perte de pics; en l'interprétant et en étudiant son effet sur différentes méthodes de mesure de déplacement.

Nous étudions ensuite le régime de forte rétro-injection optique en analysant son aspect statistique et l'effet des différents paramètres sur cet aspect. Un capteur de déplacement relatif opérant dans ce régime est alors conçu et réalisé.

Après l'avoir caractérisé, l'application de ce capteur était étendue à l'analyse modale où il avait l'avantage majeur de donner une image très fidèle du déplacement en temps réel sans traitement de signal complexe. Ce capteur est alors utilisé pour caractériser une plaque encastrée et pour détecter les impacts dans des poutres en fibre de carbone.

Table of Figures

le mercredi 22 octobre 2008

Au Laboratoire LOSE, INPT-ENSEEIHT

Sous la direction de : Mr Thierry Bosch

Spécialité : Microonde, ElectroMagnétisme et Optoélectronique

---

Analysis of Self-Mixing Moderate and Strong Feedback Regimes for Mechatronics Applications

---

Lasers have been widely used in different types of applications such as telecommunications, CD/DVD readers or for sensing purposes. A major drawback in their use is the optical feedback caused by an obstacle in their direction of propagation. This light reinjected in the active area modifies the emission properties of laser diodes and obliges the developers to consider adding isolators increasing thereby the complexity and the price of such systems.
However this optical feedback induces a variation in the emission power and frequency in function with the distance to the reflector. This phenomenon, more commonly known as self-mixing, is used in different types of displacement, velocity and vibration sensors.
In this work, the physical theory of the self-mixing effect is introduced and then a state of the art of its main applications in the different fields of instrumentation is accomplished.
A detailed study of the self-mixing signal in the moderate feedback regime is achieved introducing the effect of "loss of peaks", its physical interpretation, mechanisms and effect on different types of displacement measurement.
Afterwards, the discrepancy concerning the strong feedback regime was cleared out showing that it may be used for relative displacement measurement. A detailed study of this regime covers its statistical aspect and the influence of different parameters on this aspect.
Finally, the self-mixing sensor under strong feedback was introduced in modal analysis applications after being characterized. It was applied to study a clamped plate or to detect damage in carbon fiber CFBs. This type of sensors proved its major advantage of simplicity providing a direct image of the displacement without the need of any advanced signal processing. This facilitates its duplication where an array of sensors was used in different experiments.

Mots clés Self-mixing - Optical Feedback Interferometry- Long External Cavity- Relative Displacement Measurement - Modal Analysis**.**

INPT-ENSEEIHT

Laboratoire LOSE

2 rue Charles Camichel

31071 Toulouse cedex 7